UNIVERSITY OF MALTA

Institute for Sustainable Energy

M.Sc. Dissertation

ANALYSIS OF SEA WAVES DATA FOR THE MALTESE
ISLANDS

by

Martina Vassallo

A dissertation submitted in partial fulfilment of the requirements of
the award of Masters of Science in Sustainable Energy

COPYRIGHT NOTICE:

Dedication

To my family

Abstract

This dissertation analyses different sources of sea waves data for the Maltese Islands. The first aim was to establish the comparability of different datasets, be it modelled or measured, hindcast or forecast, for the purpose of operational use. The second aim was to asses the power potential, using the same datasets as before, and investigating the applicability of different Wave Energy Converters (WECs). The dataset sources considered are the following: Directional Wave Spectral Drifter (buoy), HF Radar, Satellite, Copernicus model, and ROSARIOSWAN model. The ROSARIOSWAN model used in this work is one which has yet to be extensively validated and fine tuned, and so, this work serves to contribute to its further development.

The inter-comparison of data from the considered datasets (excluding HF radar) generally yielded the the best correlation for the significant wave height (SWH) comparison, and the worst for the peak period comparison. ROSARIOSWAN models tend to overestimate the buoy values, while the Copernicus model compares better, despite lower resolution. Filtering out data with lower SWH yielded better correlation for all but the SWH parameter, when comparing buoy and model data. Two prominent wave directions, East and North-West, resulted from this analysis.

The wave power potential analysis indicated that the Maltese Islands have a low potential for wave energy extraction (Class I) due to, mainly, low SWH; this is typical of enclosed seas. In addition, high variability in the Maltese Waters further worsen the situation. The WEC found to be most suitable in this study is the point absorber Wavestar C6 which, at the buoy position, has an annual average output power of 192.7 kW and capacity factor of 32.1%.

Acknowledgements

I would like to thank my supervisor Dr Adam Gauci for his guidance, input and affirmation throughout this dissertation. I would also like to acknowledge the help I've received from Prof Aldo Drago and other members of the University of Malta.

CONTENTS

List of Figures

xiii

LIST OF TABLES

Glossary of Terms

Symbols

C_g	Group velocity
d	Still water depth
d_O	Orthodromic distance
E	Mechanical energy of a propagating wave
g	Acceleration due to gravity
H	Wave height
H_s	Significant wave height
k	Wave number
m_r	r^{th} moment of the variance density spectrum
P_{WEC}	Wave Energy Converter output power
$\mathcal{P}$	Wave Energy Converter power matrix
R	Correlation coefficient
R^2	Coefficient of determination
ρ	Density of water
$S(\sigma)$	Variance density spectrum

σ	Wave dispersion
T	Wave period
T_E	Wave energy period
T_p	Wave peak period

Abbreviations

ADCP	Acoustic Doppler Current Profiler
al	Saral/AltiKa
AWCP	Acoustic Wave and Current Profiler
BLUE	Best Linear Unbiased Estimate
c2	Cryosat-2
cfo	CFOSAT
CMEMS	Copernicus Marine Environment Monitoring Service
COV	Coefficient of Variation
DV	Daily Variability Index
DWSD	Directional Wave Spectral Drifter
ECMWF	European Centre for Medium-Range Weather Forecasts
EMEC	European Marine Energy Center
FNT	Float-Neck-Tank
h2b	Hai Yang-2B measurements
HF	High Frequency
j3	Jason-3
LMM	Lateral Mobile Module

MAE	Mean Absolute Error
MCA	Multi-Criteria Approach
MV	Monthly Variability Index
OI	Optimal Interpolation
O&M	Operational and Maintenance
PD	Probability of Detection
PFA	Probability of False Alarm
PTO	Power Take-Off
RMSE	Root Mean Square Error
RSS	Residual Sum of Squares
s3a	Sentinel-3A
s3b	Sentinel-3B
SAR	Synthetic Aperture Radar
SI	Scatter Index
SV	Seasonal Variability Index
SWAN	Simulating WAves Nearshore
SWH	Significant Wave Height
TSS	Total Sum of Squares
WAM	Wave Amplitude Model
WEC	Wave Energy Converter

CHAPTER 1

INTRODUCTION

The diversification of the energy mix through the increased contribution from renewable energy is one of the fundamental aspects of sustainable development. Several existing technologies are reaching their mature stage in the extraction of renewable energy and so, have been widely commercialised and applied. However, focusing on the development of newer and more efficient technologies, is still important in the aim of diversification. Wave energy is one such field where a lot of research is being carried out in order to understand the resource and how to adequately extract it. One of the main challenges of wave energy, like wind energy, is that it is stochastic. This implies that the long-term generation of wave energy, and energy which can be extracted, has to be estimated using statistical trends. [1].

In such applications, the validation and use of wave forecasts is very important. Numerical models provide a way to estimate the energy that can be generated over the reliable timescale of the wave model [1]. However, apart from wave forecasts and hindcasts, sea wave measurements obtained through *in-situ* and remote sensing, are equally important. These kinds of measurements are essential for the verification of model data; model data indeed exists to overcome one of the main limitations of measured data,

the spatial coverage limitation. It is then important for modelled data to be compared and assimilated to actual measurements to provide more and more reliable results. The process of assimilation is a means of integrating measured data, from *in-situ* or remote sensing instruments, into the modelled data calculation procedure in order to increase the accuracy of the model [2, 3].

Wave buoys are frequently used to measure *in-situ* wave parameters. These use an accelerometer, an electronic compass, and a gyroscope to measure sea waves based on the principle of gravity acceleration. In recent years, GPS wave buoys have also become popular since these are a low cost new wave measurement method that uses satellite GPS signals to measure ocean waves. *In-situ* Acoustic Doppler Current Profilers that are mounted on the seabed, can also measure waves by using the doppler effect. Remote sensing measurements usually are capable of covering larger areas of sea waves through their non-direct method of measurement. Examples of these are X-band radar, High Frequency radar, radar altimeters (equipped aboard satellites) and synthetic aperture radar.

The Physical Oceanography Research Group of the University of Malta have been using various systems to measure waves in the local context. The CALYPSO HF radar system [4] consists of a network of seven HF radars, four of which are located in Malta and Gozo. These observations are added to numerical modelling endeavours that have been now enhanced to cover the whole Malta shelf area.

The first goal of this research was to review the existing systems and compare the performance of different datasets with the intention of integrating measurements across observations and models for cross-validation and exploitation in operational services. In particular, the inter-comparison of datasets allowed for a quantitative assessment on the quality and readabil-

ity of model data to be made. These comparisons are done mainly through a linear regression and probability density function analysis, along with calculation of several statistical parameters that further inform the relationship between two datasets. In order to further test the modelled data, a significant wave height analysis is performed. This analysis provides information on the capability of the model to correctly detect a wave height above a threshold limit. The information from these comparisons yield useful insights to the performance of modelled data as well as the comparability of measured values. In particular, the ROSARIOSWAN model used in this work has yet to be extensively validated, and so, the comparisons made will contribute to its further development and fine tuning.

The second major goal of this research was to use wave data to provide assessments on the wave resource potential in hindcast and forecast mode relevant to the Maltese Islands. This entails the calculation of wave power available using both point datasets of measured and modelled data, along with regional calculations using mapped model data. The point data allows for cross comparison between most of the datasets, while the mapped model data allows for spatial analysis. The use of mapped model data in the forecast mode is then useful in providing a tool for the forecasting of the wave energy resource around the Maltese Islands. In addition, looking into the WECs and their resulting power output at a point and over a spatial domain is useful in giving an indication of their suitability.

This report is organised as follows:

In Chapter 2, a literature review that covers the different background information required in order to give context to following Chapters and the work carried out in this dissertation, is presented. The sections touch on the different wave data acquisition systems, wave models, validation and assimilation of wave data, wave energy converters, and previous studies that have

been carried out.

Chapter 3 presents the methods through which the required data was obtained for analysis. Mainly, the correlations and comparative methods that were carried out are described. The power potential calculation methods for the wave power and WEC output, are also put forward. Finally, a Multi-Criteria Approach (MCA) for WEC technology and installation location selection, is described. Chapter 4 describes the datasets utilised in this work; this consists of model data from the Copernicus Model and ROSAR-IOSWAN model, and *in-situ* and remote sensing data from buoy, HF radar, and satellite. Finally, the bathymetry, that represents the depth at different locations, is described in relation to the different locations of data acquisition.

Chapter 5 presents the results obtained from the work carried out based on the methods described in Chapter 3. An interpretation and brief discussion follows each of the presented results.

General conclusions about the main findings of this study as well as possible future work, are finally presented in Chapter 6.

CHAPTER 2

LITERATURE REVIEW

In this Chapter, different background information is presented reflecting the requirements of this work in order to give context to following Chapters and the work carried out in this dissertation. This section touches on the different wave data acquisition systems, wave models, validation and assimilation of wave data, wave energy converters and previous studies that have been carried out. In this regard, the Chapter provides a mix of both a theoretical and qualitative description of the discussed topics.

2.1 Wave data acquisition systems

As has been mentioned, several different methods of wave data acquisition exist. Each of these have associated with them their own key characteristics which makes them preferred in some situations over other technologies; the key characteristics of some of these are summarised in Figure 2.1.

The first three systems listed in Figure 2.1 are *in-situ* measurement devices, whereas the last two are remote measuring devices; these two types of measurement devices will be discussed in the following Sections [5].

System	Key characteristics
Surface-following buoy	Relatively expensive, accuracy well established, affected by currents, limited accuracy in steep waves, suitable for long-term deployment
Seabed pressure sensor	Relatively cheap, only suitable for shallow water, deployed in an array, can give directional characteristics, also measures variation in water depth
Acoustic current profiler	Relatively expensive, suitable for water depths up to 50 m, also measures marine currents, recovery required to extract data
Radar (land-based)	Deployed on land away for aggressive environment, typically requires calibration for each site, often limited to wave height measurement
Radar (satellite)	Large geographical coverage with low spatial and temporal resolution, typically limited to wave height measurement

FIGURE 2.1: *Wave measurement systems [5]*

2.1.1 *In-situ*

Wave Buoys

Wave buoys are the primary method of *in-situ* measurements when it comes to wave parameters [6]. The networks of dispatched buoys are most of the time not intended for wave resource estimation and so, oftentimes, wave buoys are dispatched according to the requirements of the project [6]. One such network is WaveNet [7] deployed around the UK and buoy networks belonging to several different programs are agglomerated by the National Data Buoy Center [8]. Wave buoys operate with on-board accelerometers that measure vertical acceleration and convert it to vertical displacement η by the integration

$$\eta = \iint \frac{dw}{dt}, \tag{2.1}$$

where w is the vertical acceleration [6]. From this, the time series of elevation is obtained [6]. Directional information can be obtained with additional sensors which can detect the tilt of the buoy and monitor the north direc-

6

tion, or with buoys that can track their horizontal motion by utilising the Earth's magnetic field [6]. Direction can also be deduced from modern non-directional buoys since these are equipped satellite communication facilities; by considering the buoy anchor location and the buoy location given by GPS, the bearing angle can be found as done by Drago et al. [9]. The wave characteristics that are sought after from the wave buoys are temporal, directional and spectral [6].

GPS wave buoys function through the utilisation of satallite communications, without the need for on-board accelerometers due to the high accuracy of GPS [6]. GPS buoys require higher energy consumption and consistent connections with satellites in order to function; this can be problematic during rough sea conditions [6]. The tilt of the buoy can be measured using inclinometers (2 perpendicular directions). When acquiring wave data, very long periods of collection may be impractical depending on the time-scale of the project at hand; in this case, 1 year of buoy data usually suffices for the verification of wave models since this captures the seasonal and short-term variability [6]. The following are the types of characteristics obtained [6]:

- Temporal : Significant Wave Height (SWH), wave period

- Directional : 'Waverose' or statistical properties of the direction properties are usually presented (ex. mean direction).

- Spectral : (spect. vs freq) This kind of information is useful when considering WECs because of the different optimal operational frequencies.

Because wave buoys have been in use for such a long time, the technology is well-established and so is their accuracy, which is beneficial for wave measurements [5]. Limitations are also well understood; steep waves, harsh

conditions, expense and risk of loss of equipment [5]. The modern GPS buoy has been shown to be more robust than the traditional accelerometer version due to the lack of moving parts, easier deployment and transport [10]. Data from the GPS buoy can be extracted through the Doppler shift in the frequencies of the GPS signal due to the motion of the buoy [10]. Some limitations of the GPS buoy data extraction method comes from the requirement of a fixed reference point, restricting the distance from the buoy to station [10].

Acoustic Waves and Current Profiler

The Acoustic Wave and Current Profiler (AWCP) is another method of measuring wave height which is installed at the sea bed [6]. The AWCP is a type of Acoustic Doppler Current Profiler (ADCP) with an additional transducer in the vertical sense which allows for wave measuring [6]. The beams, three or more, are used to characterise the current by utilising a diverging beam pattern [6]. It functions by emitting an acoustic signal followed by the receiver sampling at different times in order to establish the distance at which the signal was reflected, from which the current can then be profiled (see Figure 2.2) [6]. The AWCP allows for the measurement of both waves and currents concurrently, providing room for their interaction to also be investigated [6].

Data reflected off of hard surfaces is neglected since this signal will be stronger than the other reflected waves, overpowering them in the process [6]. The ADCP then doesn't sample certain areas in order to avoid this kind of echo along with the 'blanking distance'; the latter is an area in which a pulse lingers after it is transmitted, leading to a type of *ringing* [6]. These omitted sampling areas are then extrapolated in the post processing of the velocity data [6]. Errors in this type of system are reduced through the con-
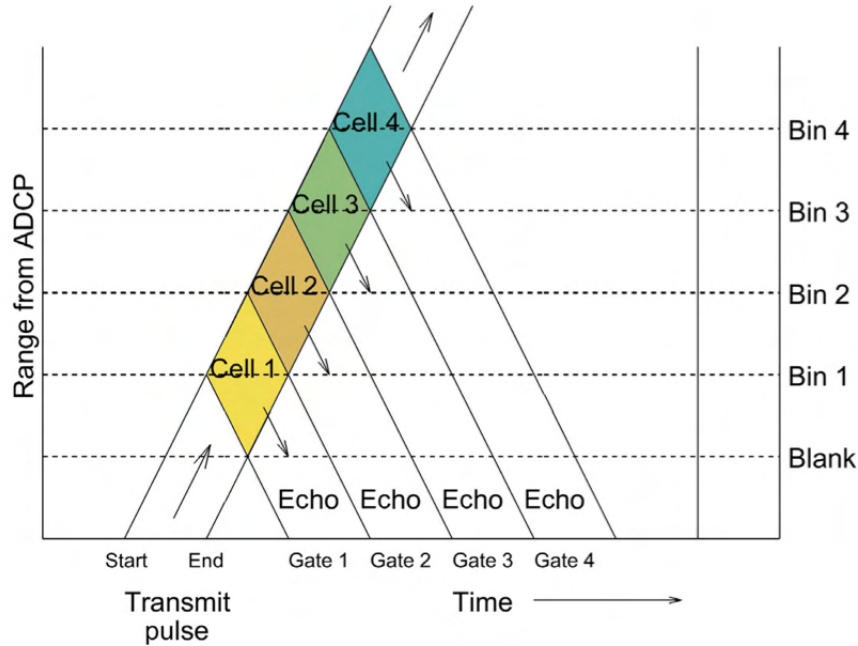
FIGURE 2.2: *Range-time plot showing how and ADCP transmits pulses and echos travel through space [6]*

sideration of an *ensemble average*, whose averaging interval must be chosen carefully to balance out the instruments noise (large interval) and for how long can the flow be statistically taken to be stationary [6].

ADCPs are often moored such that they are upward facing; the structure on which they are to be deployed have to take into account the strength of the currents at the location in order to prevent movement post-installation [6]. The European Marine Energy Center (EMEC) gives a 30-day minimum deployment standard for tidal resource evaluation, justified through the consideration of the Rayleigh criteria [6]. In reality, the length of deployment depends on factors such as cost, logistics, battery life, internal memory and weather adequacy [6]. The moored depoloyment has the benefit that it is not that affected by severe weather or marine traffic [6]. ADCPs can also be attached to the hulls of ships, looking down into the water, for measurement by accounting for the motion of the ship itself in the processing of the data; this sort of deployment is not adequate for measuring the vertical velocity

component or estimating the turbulance properties [6].

AWCP are required to be deployed in relatively shallow areas (less than 50m) as the signal would be less capable of resolving the vertical velocities of waves, the further away from the surface the device is [5]. The AWCP oftentimes stores its data on-board, meaning that the data will only be accessible once the device is retrieved, and the quality of said data only realised then [5].

2.1.2 Remote sensing

X-band radar

X-band radar utilises the frequency range 8-12 GHz and systems are found on several large research vessels; they are able to measure both waves and currents [6]. This is possible through the reflection of the signals by the sea surface, primarily through the process of Bragg Scattering [6]. This 'sea clutter' is then processed in order to obtain the relevant wave parameters [6]; different approaches to obtain the SWH (H_s) have been developed, some of which are empirical [11, 12], semi-physical [13] and purely physical [14]. X-band is limited by its short range and the requirement of significant 'sea clutter' that can be picked up by the system [6].

HF radar

High Frequency (HF) radar has an edge over the range of X-band radar due to the lower frequencies used, 3-30 Mhz, which can reach up to 200 km, however, the resolution is less than that achievable by X-band radar [6]. The range benefits give these systems the possibility for them to be

installed and maintained onshore, leading to them being utilised for long-term monitoring and keeping them away from exposed hostile conditions [6, 5]. Using the Doppler shift Bragg scattered at the surface, the radars are capable of measuring the surface currents through the utilisation of at least two HF stations [6]. The mechanism behind HF measurements of wave heights, associated with first-order Bragg scattering, was discovered in 1955 [15] and later theorised in 1971 [16]. The directional information of the sea state was shown to be obtainable from the second-order echo by Lipa [17]. Through an HF radar system survey in Europe [18], an inventory was compiled by EuroGOOS and the locations of the ongoing systems (amongst others) are displayed geographically on their online portal; there are four such stations installed in Malta [19]. The depth up to which the radar can pick up currents is that of $\lambda_R/8\pi$, where λ_R is the radio wavelength [6].

Such HF systems need calibration in order to produce meaningful data; this is often done by considering another local wave measuring instrument (such as a buoy) for data comparison [5].

Satellite and synthetic aperture radar

Satellite sensing is very good at providing global coverage and can return altimetry information from which wave height can be deduced; this information is extracted from the time it takes for the radar pulse to travel from the satellite to the sea surface and back again [6]. The data in this case, however, tends to be more coarse, and repeated measurements over the same region are more widely spaced temporarily, making them less useful for direct characterisation of the temporal properties of oceans [6]. This kind of data is then more useful in the validation of the spatial capabilities of wave models as it has the benefit of covering large geographical area [6, 5]. Altimetry-derived data can be used to obtain information about ocean tides, but is

usually assimilated with hydrodynamic models for a more accurate result [6]. In coastal areas, the presence of land deforms the waveforms, making it difficult to extract useful data from it; this is usually discarded [6].

Synthetic Aperture Radar (SAR) is essentially the same technology as X-band radar, but instead is installed on satellites or air-craft; the combined information on the movement of the aircraft and the signal that is transmitted and received allows for smaller antennas to be used, resulting in an effective large antenna [6].

2.2 Models

2.2.1 Wave Models

The use of models for the simulation of the oceans and seas is beneficial in that they provide a less costly alternative to *in-situ* measurement campaigns; this makes models highly suitable for the scoping stages of a project [20]. It is important to keep in mind, however, that model data is reliant on its inputs, which can only be parametrised and validated by *in-situ* measurements [20]. The models that are used mostly nowadays are third generation phase-averaged wave models where, as opposed to the second generation models, the wave spectrum evolution is based on the physics governing the wave generation; the three drivers of wave generation are wind, dissipation and nonlinear wave-wave interaction [20, 21]. These third generation models are based on the solving of the action density, N, balance equation

$$\frac{\partial N}{\partial t} + \frac{\partial c_\lambda N}{\partial \lambda} + \frac{\partial c_\phi N}{\partial \phi} + \frac{\partial c_\sigma N}{\partial \sigma} + \frac{\partial c_\theta N}{\partial \theta} = \frac{S_{\text{tot}}}{\sigma}, \qquad (2.2)$$

where σ is the angular frequency, θ is the wave direction, λ and ϕ are the zonal and meridonal directions and c_λ, c_ϕ, c_σ and c_θ are the propagation velocities in their respective spaces, and S_{tot} is the source term [20]. The most commonplace wave models using this formulation for resource assessment are WAM [21], SWAN [22] and GFS-Wave (previously WAVEWATCH III) [23]. The models function by calculating for the source terms, S_{tot}, that are contributed by wind, dissipation and nonlinear wave-wave interaction [20].

The wind input contributes both a linear (A) and exponential growth (BE), the former being significant during the early growth by the turbulence above the sea surface and the latter in later stages when the movement of the wave depends on its own size [20]. This contribution can be thus described by

$$S_{\text{in}}(\sigma, \theta) = A + BE(\sigma, \theta). \tag{2.3}$$

Wave breaking (white capping), interaction with the sea bed and depth-induced wave breaking contribute to the dissipation of the wave energy; in deep water, the waves are dissipated only through the process of white capping [24]. The wave energy due to the sea bed friction can be expressed by the equation

$$S_{\text{ds, b}} = -C_{\text{b}} \frac{\sigma^2}{g^2 \sinh^2 kd} E(\sigma, \theta), \tag{2.4}$$

whereas the physics behind the dissipation due to wave breaking is the least understood in wave evolution and cannot be formulated as easily [20, 25]. This form of dissipation is then expected to have a smaller impact on the wave evolution due to its relative rareness (at most about 5%), however, focus to formulate better models for this term should not be underestimated [25]. The dissipation due to wave breaking is then, generally, taken to be

based on Hasselmann's statistical formulation

$$S_{ds, w} = -\eta \sigma^2 E(k), \qquad (2.5)$$

where η is a constant that represents the statistical properties of the dissipation process and k is the wavenumber [26], and is often considered in the form

$$S_{ds, w} = -\Gamma \tilde{\sigma} \frac{k}{\tilde{k}} E(\sigma, \theta), \qquad (2.6)$$

where Γ is related to the steepness of the waves, $\tilde{\sigma}$ and $\tilde{k}$ are the mean frequency and mean wave number, respectively [22]. In the case of the SWAN, the depth-induced wave breaking is integrated into the model through the inclusion of the source term

$$S_{ds, br} = -\frac{S_{ds, br, tot}}{E_{tot}} E(\sigma, \theta), \qquad (2.7)$$

where E_{tot} is the total wave energy and $S_{ds, br, tot}$ the rate of dissipation of E_{tot} [22].

For the case of nonlinear interactions, two main processes dominate. These are three-wave interactions and four-wave interactions; the former are important in shallow waters and the latter in deep and intermediate water [20]. Three-wave interactions cannot occur in deep waters because the resonance conditions, by which these nonlinear interactions are governed, cannot be satisfied by three freely propagating waves [24]. The interaction in deep water occurs due to the forming of two diamond patterns by two pairs of two interfering waves and, given that these four components satisfy the following

$$f_1 + f_2 = f_3 + f_4 \tag{2.8}$$

$$\vec{k}_1 + \vec{k}_2 = \vec{k}_3 + \vec{k}_4, \tag{2.9}$$

where f is the frequency and $\vec{k}$ is the wave-number vector, these two diamond patterns will interact between them; these are called quadruplet wave-wave interactions [24]. These interactions do not change the energy in the spectrum overall, as they only redistribute it [24]. The interaction between three-waves, triad wave-wave interactions, occur when the following resonance conditions are met

$$f_1 + f_2 = f_3 \tag{2.10}$$

$$\vec{k}_1 + \vec{k}_2 = \vec{k}_3 \quad [24]. \tag{2.11}$$

The WAM model [21] was the first realisation of such a third generation model as described here, and the development of WAVEWATCH III [23] based on this model. Because of the varying properties of wave evolution at different sea depths, the SWAN model was developed from WAM such that this model includes the effects of the additional dispersion mechanisms experienced in coastal areas (shallower areas) [22]. This model then takes into consideration also the geometries of coastal areas and how the waves interact with these obstacles (by processes of transmission and reflection) [24].

2.2.2 Wind forecasting models

Apart from the utilisation of wave models, it is worth noting that the input to the source term in equation 2.2 that comes from wind, equation 2.3, is

often driven by wind forecast models when simulations are done in forecast mode. Indeed, the performance of the model varies according to which wind model is utilised in the simulation; one such study to compare the different outcomes from combinations of three different wave models driven by four different wind fields was carried out by Ardhuin et al. [27].

There exists several approaches to the problem of wind forecasting. Different methods are applicable in different cases according to the required prediction horizon; broadly classified, these can be ultra-short-term (few minutes - 1hr), short-term (1 hr - several hrs), medium-term (several hrs - 1 week), long-term (1 week - 1 yr and beyond) [28].

One type of wind forecasting is based on persistence modelling, wherein the future wind speed is assumed to be the same as that when the prediction was made [28]. This kind of modelling is applicable only on the ulta-short-term time scale since accuracy rapidly decreases with increase in time [28].

Another approach is to consider numeric weather prediction (NWP). Terrain and more localised topological features are considered in this type of modelling, where factors such as temperature, pressure, surface roughness and obstacles are also integrated into the model [28, 29]. Increasing the spatial resolution of such models, to include more and more obstacle and terrain detail, increases the computational power required to use this type of modelling [28]. High resolution models of this kind are then not very feasible to use in short-term predictions due to the computational load they incur [29].

Primarily based on historic values, statistical approaches of wind predictions are cheaper and easier to model since they do not need the same amount of computational power to resolve [28]. These types of models include techniques such as auto regressive (AR), auto regressive moving average (ARMA), auto regressive integrated moving average (ARIMA), Bayesian

approach, and gray predictions [28]. These types of models are mostly appropriate for the short-term time-scale [28].

As in other data driven fields, artificial intelligence (AI) is also used in the field of wind prediction. One of the benefits of using AI is that the model does not require a predefined mathematical model, and is based on the training period of the model [29]. Some of the type's of AIs that have been adopted for wind forecasting efforts include artificial neural network (ANN), adaptive neuro-fuzzy inference system (ANFIS), fuzzy logic methods, support vector machine (SVM), neuro-fuzzy network, and evolutionary optimization algorithms [28].

In addition to the methods defined above, hybridised approaches have also been considered in order to create better optimised models [28]. This approach allows for information to be lent from one model to another, creating an overall more robust model [28].

2.3 Validation and assimilation

2.3.1 Validation

The validation of models is an important exercise in order to add confidence to its utilisation. Once a model is validated, it can be applied in other regions, insofar that the parameters have not been overly fit to meet the testing location [20]. The commonly used metrics that are used in validation exercises of models are the correlation coefficient, Root Mean Square Error (RMSE), Scatter Index (SI), Mean Absolute Error (MAE) and bias [20]. These methods will be further expanded on in Chapter 3.

2.3.2 Assimilation

It is more commonplace to find assimilation of observations within the numerical weather prediction and ocean modelling communities rather than in the field of operational wave modelling [30]. The process of assimilation can greatly, and positively, impact the quality of numerical wave forecasts as it aims to minimise the difference between measurements and model estimates by integrating the former into modelling procedures [2, 3]. Techniques of assimilation are generally divided into sequential and variational techniques; in the former, previous model states are not taken into consideration, but the model is corrected at each individual time step [2]. In the case of variational techniques, these consider the dynamics of the wave model as a whole by the recalculation of the waves, and not just considers the error between measurement and prediction at each step [2].

In light of the positive effects that assimilation has on the models, several studies that deal with modelling of waves carry out exercises of assimilation with measured data. Examples of which are the assimilation of the: WAM model with data from SAR and buoy data [31], WAVEWATCH III model with data from satellite altimeter and buoy data using the NEMOVAR variational scheme [30], WAM model with altimeter data using a sequential method [32] and even the use of a neural network for the assimilation of buoy data with a SWAN model nested in a WAVEWATCH III model [33].

Sequential Methods

The sequential methods are generally less computationally intensive than variational methods, which has lead to their extensive use in operational applications especially in the past [3]. This results because these methods consider the model only forward in time, and are so time independent; two

such sequential methods are Optimal Interpolation (OI) and the Kalman filter [3].

The first documented use of the OI method for SWH analysed-field construction was done by Lionello et al. [32], and provided the first consolidated technique capable of spreading altimeter data over the model grid [34, 32].

The analysed SWH in the case of the OI described by Lionello et al. [32] is expressed as the linear combination,

$$H_A^i = H_P^i + \sigma_P^i \sum_{j=1}^{N_{\text{obs}}} W_{ij} \frac{H_O^j - H_P^j}{\sigma_P^j}, \tag{2.12}$$

where H_P^i are model-produced, first-guess results, H_O^j are the observations, N_{obs} is the number of observations, W_{ij} are the weights chosen such that the RMSE of the analysis (σ_A^j) is minimsed, and σ_P^j is the RMSE in the model prediction

$$\sigma_P^j = \sqrt{\langle (H_P^j - H_T^j)^2 \rangle}, \tag{2.13}$$

where H_T^j is the true SWH value. The weights, assuming that the model and measurement errors are uncorrelated, are expressed as follows:

$$W_{ij} = \sum_{k=1}^{N_{\text{obs}}} P_{ik} M_{kj}^{-1}, \tag{2.14}$$

where,

$$M_{kj} = P_{kj} + O_{kj}, \tag{2.15}$$

where P and O are the prediction and observation error correlation matrices, respectively, which are in turn expressed as

$$P_{kj} = \left\langle \frac{(H_P^k - H_T^k)(H_P^j - H_T^j)}{\sigma_P^k \sigma_P^j} \right\rangle, \qquad (2.16)$$

and,

$$O_{kj} = \left\langle \frac{(H_O^k - H_T^k)(H_O^j - H_T^j)}{\sigma_P^k \sigma_P^j} \right\rangle. \qquad (2.17)$$

The matrices P and O therefore need to be predefined; if known exactly, which is not the case in practice, the resulting weights would be at their optimal values [34]. Observational errors are usually assumed to be uncorrelated and random, reducing O to its diagonal values:

$$O_{kk} = \frac{\sigma_{obs}^2}{\sigma_P^2}, \qquad (2.18)$$

where σ_{obs} is the RMSE of the observations [34]. P is a harder to specify quantiy, but is known to be horizontally correlated [34]. Lionello et al. set the expression of P, tentatively, as

$$P_{kj} = \exp\left[-\frac{|x_k - x_j|}{L}\right], \qquad (2.19)$$

in their description, where L is the decorrelation length scale and $|x_k - x_j|$ is the difference between points k and j [32]. Greenslade and Young [34] provide a number of expressions for P_{kj} which have been used in literature to describe this parameter, which will be listed here with their respective source citation:

$$P_{kj} = \left(1 + \frac{|x_k - x_j|}{L}\right) \exp\left[-\frac{|x_k - x_j|}{L}\right] \quad [35], \tag{2.20}$$

$$P_{kj} = \exp\left[-\frac{1}{2}\frac{|x_k - x_j|^2}{L^2}\right] \quad [36], \tag{2.21}$$

$$P_{kj} = \exp\left[-\left(\frac{|x_k - x_j|}{L}\right)^{\frac{3}{2}}\right] \quad [37], \tag{2.22}$$

$$P_{kj}(f) = \exp\left[-\frac{1}{2}\frac{|x_k - x_j|^2}{L(f)^2}\right] \quad [38], \tag{2.23}$$

where, for the case of the last equation 2.23, the background error correlation function was defined as a function of wave frequency, since, full wave spectra was assimilated [34].

In the case of the sequential process of Kalman Filtering, all the available data is used to calculate a more accurate description of the wave state as well as the uncertainties of the different information sources [39]. This method will be explained as described by Talgrand in [39]. Consider the following expression,

$$\mathbf{z} = \Gamma \mathbf{x}^t + \zeta, \tag{2.24}$$

where $\mathbf{z}$ is a vector of known available observations, $\mathbf{x}^t$ is the unknown true state vector, Γ is the *observation matrix* which is the statistically known link between the estimated parameters and the observations, and ζ is the associated error. An important assumption here is to consider that the error vector is unbiased:

$$E(\zeta) = 0 \tag{2.25}$$

and that its variances-covariances given by

$$E(\zeta\zeta^\top) = \Sigma, \qquad (2.26)$$

are known, where $E()$ denotes the statistical mean. When $\mathbf{z}$ can be decomposed into two vectors:

$$\mathbf{z} = (\mathbf{x}^{b\top}, \mathbf{y}^{o\top})^\top, \qquad (2.27)$$

where $\mathbf{x}^{bT}$ (dim m) is the background estimate of $\mathbf{x}^t$ and $\mathbf{y}^{bT}$ (dim p) is an additional set of measured observations. The background estimate is an a priori estimate of the true state, which can be derived from climatological average data. These two variables can then be represented by

$$\mathbf{x}^b = \mathbf{x}^t + \zeta^b \qquad (2.28)$$

$$\mathbf{y}^o = \mathbf{H}\mathbf{x}^t + \epsilon, \qquad (2.29)$$

where $\mathbf{H}$ ($p\times n$) is the observation matrix and ϵ are the associated observation errors. The parameters in equation 2.24 can be then expressed as

$$\Gamma = (\mathbf{I}_n, \mathbf{H}^\top)^\top, \qquad (2.30)$$

$$\zeta = (\zeta^{b\top}, \epsilon^\top)^\top, \qquad (2.31)$$

and

$$\Sigma = \begin{bmatrix} E(\zeta^b \zeta^{b\top}) & E(\zeta^b \epsilon^\top) \\ E(\epsilon \zeta^{b\top}) & E(\epsilon \epsilon^\top), \end{bmatrix} \tag{2.32}$$

which, assuming that the errors ζ^b and ϵ are uncorrelated, reduces to

$$\Sigma = \begin{bmatrix} \mathbf{P}^b & 0 \\ 0 & \mathbf{R} \end{bmatrix}. \tag{2.33}$$

The Best Linear Unbiased Estimate (BLUE) is then sought after in the form

$$\mathbf{x}^a = \mathbf{A}\mathbf{z}, \tag{2.34}$$

while imposing the condition that $\mathbf{x}^a$ is unbiased:

$$E(\mathbf{x}^a - \mathbf{x}^t) = 0, \tag{2.35}$$

which is satisfied if

$$\mathbf{A}\Gamma = \mathbf{I}_n, \tag{2.36}$$

while also imposing the condition that the trace of the covariance matrix of the estimation error,

$$\mathbf{P}^a = E((\mathbf{x}^a - \mathbf{x}^t)(\mathbf{x}^a - \mathbf{x}^t)^\top) \tag{2.37}$$

is minimised.

The solution to this problem is given by

23

$$\mathbf{A} = \left[\Gamma^\top \Sigma^{-1} \Gamma\right]^{-1} \Gamma^\top \Sigma^{-1} \tag{2.38}$$

and

$$\mathbf{P}^a = \left[\Gamma^\top \Sigma^{-1} \Gamma\right]^{-1}. \tag{2.39}$$

Finally, combining equations 2.30, 2.33, 2.34, 2.38 and 2.39 results in the following expressions for $\mathbf{x}^a$ and $\mathbf{P}^a$:

$$\mathbf{x}^a = \mathbf{x}^b + \mathbf{P}^b \mathbf{H}^\top [\mathbf{H} \mathbf{P}^b \mathbf{H}^\top + \mathbf{R}]^{-1}(y^o - \mathbf{H}\mathbf{x}^b) \tag{2.40}$$

$$\mathbf{P}^a = \mathbf{P}^b - \mathbf{P}^b \mathbf{H}^\top [\mathbf{H} \mathbf{P}^b \mathbf{H}^\top + \mathbf{R}]^{-1} \mathbf{H} \mathbf{P}^b \tag{2.41}$$

In order to arrive to the Kalman Filtering sequential process, the temporal dimension must be included. The resulting expressions for the temporal versions at time $k + 1$ of the parameters $\mathbf{x}^b_{k+1}$, $\mathbf{x}^t_{k+1}$ and $\mathbf{P}^b_{k+1}$ are given by the following expressions:

$$\mathbf{x}^t_{k+1} = \mathbf{M}\mathbf{x}^t_k + \eta_k, \tag{2.42}$$

$$\mathbf{x}^b_{k+1} = \mathbf{M}\mathbf{x}^a_k, \tag{2.43}$$

$$\mathbf{P}^b_{k+1} = \mathbf{M}\mathbf{P}^a_k \mathbf{M}^\top + \mathbf{Q}, \tag{2.44}$$

where $\mathbf{M}$ is the transition matrix, describing the state vector change from time k to $k+1$, η_k is the model error, where the model refers to the transition matrix, which can be considered to be the assimilation model, it is assumed unbiased, random, uncorrelated in time and is subject to the condition that

$$E(\eta_k \eta_l^\top) = \mathbf{Q}\delta_{kl}, \tag{2.45}$$

where $\mathbf{Q}$ is a known covariance matrix for η_k. These considerations lead to the BLUE being expressed as

$$\mathbf{x}_{k+1}^a = \mathbf{x}_{k+1}^b + \mathbf{P}_{k+1}^b \mathbf{H}^\top [\mathbf{H}\mathbf{P}_{k+1}^b \mathbf{H}^\top + \mathbf{R}]^{-1}(y_{k+1}^o - \mathbf{H}\mathbf{x}_{k+1}^b) \tag{2.46}$$

$$\mathbf{P}_{k+1}^a = \mathbf{P}_{k+1}^b - \mathbf{P}_{k+1}^b \mathbf{H}^\top [\mathbf{H}\mathbf{P}_{k+1}^b \mathbf{H}^\top + \mathbf{R}]^{-1}\mathbf{H}\mathbf{P}_{k+1}^b \tag{2.47}$$

In combination, equations 2.43, 2.44, 2.46 and 2.47 represent the sequential process of Kalman Filtering, which gives the BLUE at time $k + 1$ using all observations up to time $k + 1$.

Variational Methods

One of the more commonly used variational methods is that which utilises the adjoint model. It is the numerical complexity of wave models which makes the use of the adjoint model more computationally intensive, in general, than sequential methods [40].

The bases of the adjoint method, as describe by Talgrand in [39], is based on the minimisation problem described by the equations

$$\mathbf{x}_{k+1}^t = \mathbf{M}\mathbf{x}_k^t, \tag{2.48}$$

$$J(\mathbf{x}) \equiv \sum_{0 \le k \le N} [\mathbf{H}\mathbf{x}_k - \mathbf{y}_k^o]^\top \mathbf{R}^{-1}[\mathbf{H}\mathbf{x}_k - \mathbf{y}_k^o]. \tag{2.49}$$

One can note from comparing equations 2.42 and 2.48 that this approach assumes a perfect model with $\eta_k = 0$. Equation 2.49 is the objective function,

which is the variational formulation of the estimation of $\mathbf{x}^t$; $J(\mathbf{x})$ is to be minimised subject to the constraint given by equation 2.48.

The adjoint method is an approach aimed to solve the minimisation problem numerically, and can be derived from the use of the Lagrange multipliers technique or through the reduction of equation 2.48 to only use the initial state $\mathbf{x}_0$.

2.4 Wave Energy Converters

Several different types of WECs exist due to the different approaches conceived of to extract the energy from the wave energy resource; the variety in this type of renewable extraction is much larger than for other renewable sources, resulting in WECs whose efficiency depends on the wave characteristics [5, 41]. These devices are generally categorised into three categories:

1. *Terminators*, having a larger horizontal structure perpendicular to the wave propagation,

2. *Attenuators*, having a larger horizontal structure parallel to the wave propagation,

3. and *Point absorbers*, whose structures are made to not be directional.

Another form of classification involves description by installation location; *onshore*, *near-shore* and *offshore* [5]. This classification is helpful due to the different necessities related to water depth and land proximity.

The IEA Ocean Energy Systems adopt a different type of classification, see Figure 2.3, which is based more on the working principle of the WEC [42].
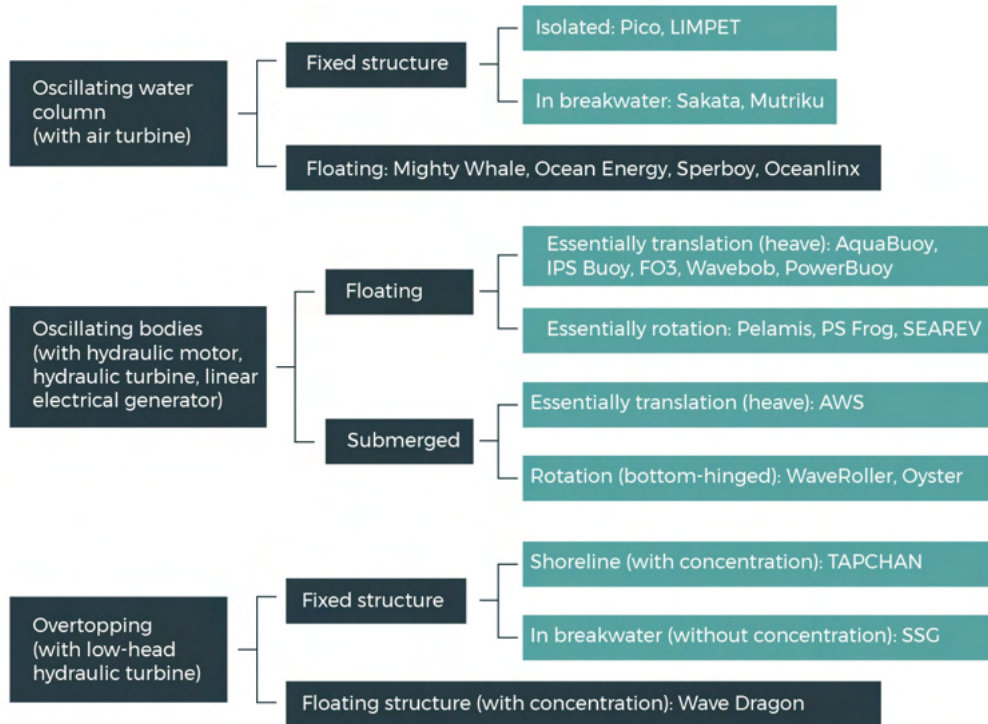
FIGURE 2.3: *Ocean Energy Systems WEC classification [42]*

The WECs considered in this work have been obtained from a study by Kamrazand and Hadadpour [41], having themselves extracted the most common devices used in similar studies, in order to apply a MCA to WEC selection and WEC location selection. Additionally, the Pelamis WEC is also considered in this study due to it being mentioned in the study by Guillou and Chapalain [43], in which the annual and seasonal variabilities in the performances of wave energy converters was investigated.

The power matrices of WECs characterise the operation of the device under different sea states and are hence useful in studying the performance of the WEC in different areas. The power matrix of a WEC constitutes of a two dimensional histogram which gives the power output for given ranges of SWH, H_s, and energy period, T_E, which will be described in more detail in Section 3.3, and the method of obtaining the output power of WEC

27

from these power matrices in combination with sea parameter data will be described in Section 3. Information regarding the WECs is summarised in Table 2.1.

TABLE 2.1: *Different WEC technologies*

Technology	Rated power / kW	Classification	Matrix resolution $(H_s \times T)$	Reference
Archimedes	2500	Point absoarber	0.5 m × 0.5 s	[41]
Wavebob	1000	Point absoarber	0.5 m × 0.5 s	[41]
Aquabuoy	250	Point absoarber	0.5 m × 1.0 s	[41]
Wavestar C6	600	Point absoarber	0.5 m × 1.0 s	[41]
Wave Dragon	5900	Terminator	0.5 m × 1.0 s	[43]
CECO ($\alpha = 30°$)	692	Point absoarber	1.0 m × 2.0 s	[44]
SeaPower	3587	Attenuator	0.5 m × 1.0 s	[41]
OEbuoy	2880	Oscillating water column	0.5 m × 1.0 s	[41]
Pelamis	750	Attenuator	0.5 m × 1.0 s	[43]

2.4.1 WEC descriptions

Point absorbers

Archimedes: The Archimedes Waveswing is a submersible device which uses a direct-drive generator to convert wave energy to electricity [45]. Developed by AWS Ocean Energy, the system's working principle is based on changing water pressure due to wave transmission, which is then converted into mechanical energy [45]. A completed Archimedes Waveswing 16 kW unit is shown in Figure 2.4.

The output pattern of this device is however more variable as it doesn't have an effective rated power, which allows it to generate more energy in higher energy waters [46]. The information regarding the operation of this WEC technology, vis-a-vis the power matrix, is to be based on that which is available from the work of Kamranzad and Hadadpour [41], which is in turn based on the 2005 report by the Environmental Change Institute [46]. The current state of the Archimedes Wavestring technology has been developed

28

FIGURE 2.4: *16 kW Archimedes Waveswing [Image by AWS]*

and refined much further since its first test in 2004, and that as is reported in the aforementioned literature, and is now more adequate to suit the evolving market and customer needs [45]. The current device is suitable for depths > 25 m with configurations of ratings between 25 and 250 kW, with the 25 kW version being available for order [45].

Wavebob: The Wavebob is an axi-symmetric, self-reacting device and operates on the principle of differential vertical motion [47, 48]. The device's functioning relies on the differing properties of two floating buoys of which the WEC is made up of; this can be observed in Figure 2.5, where the buoys are of two types, a torus and Float-Neck-Tank (FNT) [49]. Figure 2.6 shows a 1:4 scale model of the WEC.

The relative vertical motion is generated in this case by the high natural frequency of the torus buoy, while the heavier FNT has a low natural frequency

29
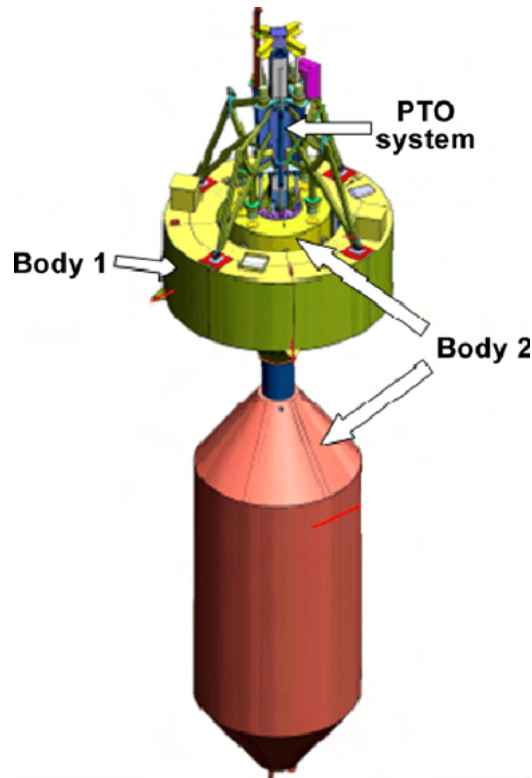
FIGURE 2.5: *Wavebob Schematic [Image by Wavebob Ltd.]*

and high inertia, causing a mismatch in oscillating period and amplitude between the two buoys [49]. The Power Take-Off (PTO), marked in Figure 2.5, then converts this motion to electricity [49].

The Wavebob company has been defunct since 2013 due to lack of funding; the development of the Wavebob has been halted since [50].

AquaBuoy: AquaBuoy, developed by the company AquaEnergy, also functions with the principle of vertical displacement. In this technology's case the generation of electricity is not direct as the system converts the vertical component of wave kinetic energy into pressurised water [51]. The pressurised water jets are generated through opposing full-cycle hose pumps, which alternately produce a pressurised water jet from the same output during upward and downward movement [51]. This jet is in turn directed

30

FIGURE 2.6: *1:4 Scale Wavebob model [49]*

towards a Pelton turbine coupled with a generator [51]. A schematic and image of the AquaBuoy are illustrated in Figures 2.7 and 2.8, respectively.
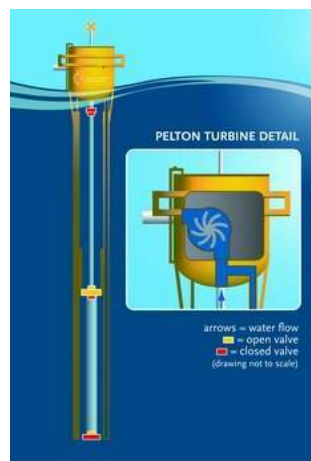
FIGURE 2.7: *AquaBuoy Schematic [52]*

Wavestar C6: The Wavestar C6 is a 600 kW-rated machine made up of large platform which is attached to the seabed [53]. Extending out of the platform are the energy extraction devices: arms connected to floats which rise and fall with the passing waves, transferring the energy from the waves to a generator via hydraulic connections to a PTO [53]. The 20 floats, on either side, are connected in such a way that the resulting energy production

31

FIGURE 2.8: *AquaBuoy [52]*

is continuous and steady, which is relatively hard to accomplish given the fluctuating nature of waves [53]. The WEC is made to operate in sea states of $H_s < 8$ m, above which the floats are lifted out of the water as a storm protection measure [54]. A visualisation of the full-scale WEC is given in Figure 2.9.
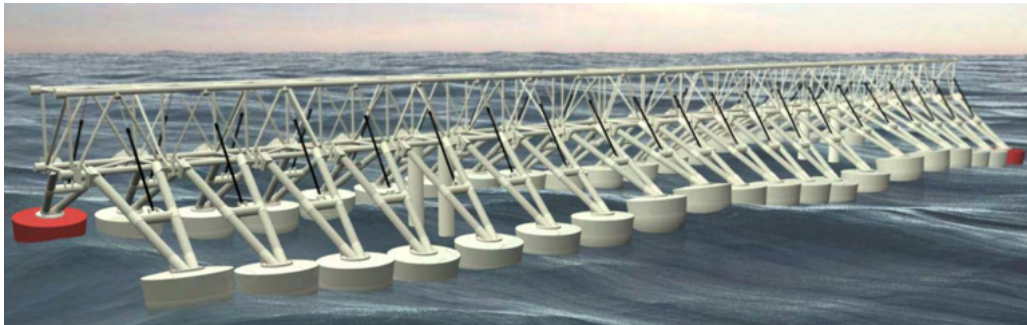
FIGURE 2.9: *Wavestar C6 full-scale system visualisation [Image by Wave Star Energy]*

In 2009 a test Section of the 600 kW machine was installed, consisting of two floats, and has been supplying energy to the grid since 2010 [55]. At the time of writing, the operation of Wavestar has been paused due to an ongoing rebuild; two more floats are to be added while the PTO system is to be upgraded with state of the art technology [53].

CECO: The CECO WEC utilises a concept which is not common amongst other technologies; it is designed in such a way that the device extracts energy from both the horizontal and vertical components of the wave through oblique oscillations, as opposed to extracting only the vertical or horizontal component [56]. This is achieved through relative motion between the floating component (two Lateral Mobile Modules (LMMs) attached to a sliding frame) and the supporting structure (which holds the PTO and is attached to the seabed) inclined at an angle α [56]. The system can be classified as a direct mechanical drive system [56]. Illustrations of the CECO described properties are shown in Figure 2.10.
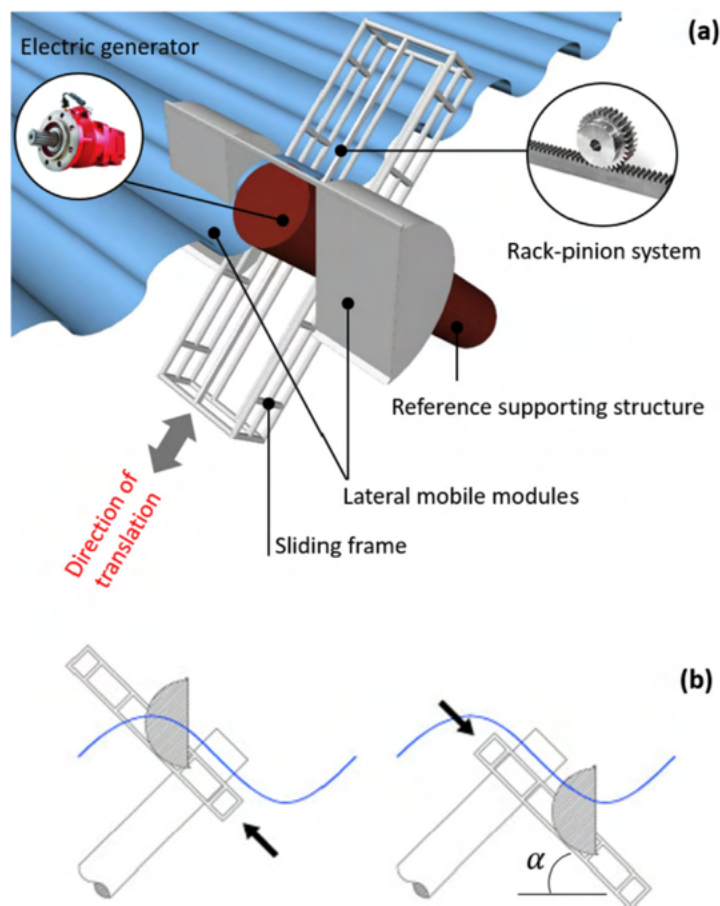
FIGURE 2.10: *3D sketch of the CECO concept (a) and its motion under wave action (b) [56]*

Performance of the CECO WEC is dependant on a variety of parameters: the

LMM's geometry, mass, dimensions and submergence levels, along with the inclination of the PTO system and its damping effect [56]. These parameters can then be altered in order to be able to develop a suitably efficient system at a specific location, keeping in mind that the oscillatory motions should be aligned with the dominant wave propagation direction [56]. The importance of the inclination of the system, that is the value of α, is here reiterated, since this has considerable effects on the output power [44]. Indeed, in [44], López et al. carried out an investigation in order to be able to quantify the effects of the PTO inclination on the performance of the CECO WEC. In the aforementioned work, five values of α were considered (15-75° in steps of 15°), for which the respective power matrices were obtained. In this work, the power matrix associated with $\alpha = 30°$ will be considered. This WEC is currently at a level 4 of technological readiness [56].

<div align="center">

Terminator

</div>

Wave Dragon   The Wave Dragon WEC takes an approach to energy generation from waves that aims to apply well-proven principles from hydro power plants [57]. The idea behind this device is to use the potential energy from the waves, rather than oscillatory motion as depended on by the point absorbers described. The structure of the WEC is such that it is both stationary and floating, in that, it is comparable to having a moored ship in deep water which is made to be as stationary as possible [57]. Wave Dargon is aimed at being set up in deep waters in order to be able to intercept waves of higher energy than coastal waves [57].

The Wave Dragon is comprised of two wave reflectors that redirect the waves up a ramp and into a reservoir [58]. The construction of the ramp is such that is is doubly curved, elliptical and circular, thus allowing for better overtopping into the reservoir [58]. As widely used in hydro plants, the Wave

Dragon is equipped with a propeller turbine which is rotated by water flow when the reservoir is emptied [58]. The turbines are coupled with permanent magnet generators, which are suitable for low and variable speeds, while also eliminating the need for a gearbox [58]. An image along with a diagram of the working principle of the Wave Dragon can be found in Figure 2.11
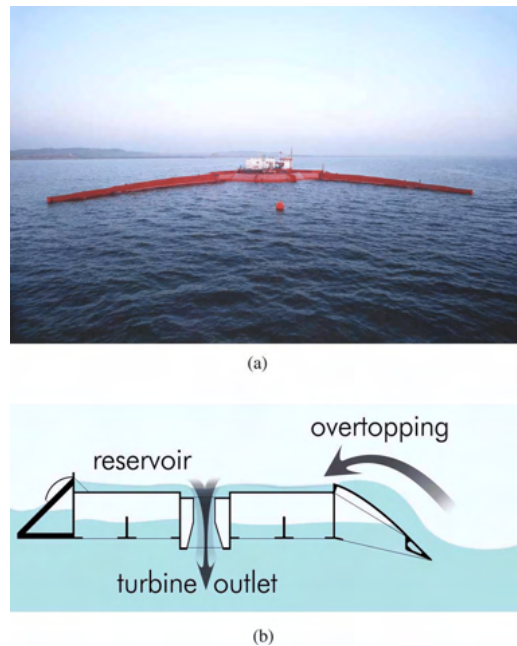
FIGURE 2.11: *Wave Dragon WEC image and diagram [59]*

Attenuator

SeaPower: The Seapower WEC is relatively simplistic in its design and construction, making it comparatively more cost effective than alternate attenuator technologies [60]. The device is made of a couple of hollow pontoons and a singular hinge, making it relatively low maintenance and durable [60]. Altering the dimensions of the pontoon properties and spacing is necessary in order to be able to make the WEC suitable for the location where it is to be installed [60]. A 1:4 scale prototype of the WEC installed in Foynes, Ireland is shown in Figure 2.12, where the describe features can be observed.

The principle of operation is illustrated in Figure 2.13, showing a diagram extracted from the patent for the Seapower technology.

Figure 2.12: *1:4 Scale Seapower model at Foynes, Ireland [Image by Seapower Ltd.]*

Two types of PTO are being developed for use with the Seapower, each having in scope different end user requirements [60]. One PTO is the Hydraulic Seawater to Freshwater PTO System, which is specifically designed for the purpose of desalination or pumped water storage [60]. The other PTO being developed is the Mechanical Direct Drive PTO module, which is rated at 1 MW with 25% capacity, and is intended for grid-connected direct electricity generation from deep water sites [60].

Pelamis: The Pelamis WEC was the world's first energy wave project to be implemeneted on a commercial scale; located 5km off the Portuguese Agucadoura coast, the system started delivering 2.25MW of power in September of 2008 [61]. This WEC is made up of four tube segments, each of length 120 m, attached together with joints which house the PTO systems, through which the mechanical energy is converted into electricity [43]. Figure 2.14 shows a full-scale version of the WEC installed in place. The Pelamis com-
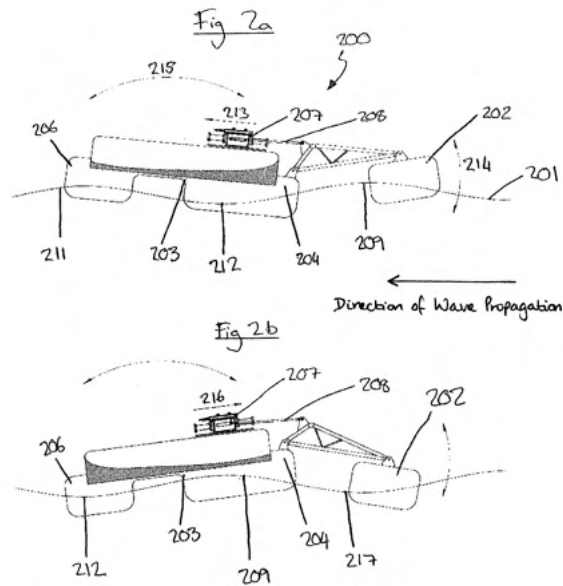
FIGURE 2.13: *Seapower diagram patent extract [Image by Seapower Ltd.]*

pany has been defunct since 2014, with the assets and intellectual properties now being owned by Wave Energy Scotland [62].

FIGURE 2.14: *Pelamis Wave Power WEC [Image by EMEC]*

Oscillating water column

OEbuoy: The OE buoy WEC, Figure 2.15, functions on the principle of an oscillating water column. The WEC is made up of a large floating platform with partially submerged water chambers wherein water can flow in and out. The oscillatory motion of the water in the chamber pushes air in and out

of the chamber through a turbine, which is in turn coupled to a generator which converts the rotation of the turbine into electricity [63].

FIGURE 2.15: *OE buoy [Image by OceanEnergy]*

2.5   Studies on Wave Power Potential

The measurements and models as described in Sections 2.1 and 2.2, accompanied by the methods mentioned in Section 2.3, allow for studies regarding the wave energy potential in an area to be carried out. Using statistical models, the different wave parameters over defined periods of time can be averaged out. To characterise an area's energy potential on a yearly, monthly and seasonal basis (as is most commonly required for the estimation of energy production from WECs) several years of data is required; often this data is acquired from wave models in hindcast. This multi-year data allows for not just a better statistical representation of the wave energy, but also for the calculation of the annual, monthly, and seasonal variability index, quantifying how the wave parameters and resource changes according to the period under consideration.

Several such investigations, the characterisation of the wave parameters and energy resource, have been carried out in different locations due to the in-

creasing interest in wave energy as a source of renewable energy. In an investigation by Mota and Pinto [64], the wave energy potential along the western Portuguese coast was considered. The study was aimed at identifying potential approperiate locations for the implementation of a WECs. The area identified by this study as the most appropriate was that from Peniche to Nazaré, having an annual wave energy of around 200 MWh/m. The first main conclusion from this work is that one cannot base nearshore energy assessments on those performed offshore when the coast is not facing the predominant wave direction. The second is that, in the case when the coast is exposed and oriented towards the predominant wave direction, than the wave power offshore and nearshore are more comparable.

Vicinanza et al. [65] investigated the wave energy potential along the north-west of Sardinia using two wave-data sources: buoy records and hindcast data. The main driver of this study is the potential exploitability of the sea as a source for electricity generation, since, Sardinia suffers from high costs of electricity due to it being an island. As a reference of the north-west coast of Sardinia, three locations along the Meridian with latitudes of 39.5°, 40°, and 41.5° were considered, with resulting annual wave power ranging from 8.19 kW/m to 10.29 kW/m. The resulting output power is mostly delivered through north-westerly waves.

Iglesias et al. [66], investigated the wave energy potential in Galicia, in the north-west of Spain, which experiences harsh wave climates. Using a third-generation WAM model, 18 of the closest points to the coast were selected, resulting in an annual energy ranging from 128.59 MWh/m to 438.89 MWh/m, with an associated average power ranging from 14.68 kW/m to 50.10 kW/m. It is noted in the study that wave energy is not the only factor to be consider when choosing a location for WEC installation; proximity to facilities, minimal environmental disturbance, non-interference with

marine traffic and, fishing and aquaculture are important to be considered.

Iglesias and Carballo [67], investigated the wave energy potential along the Death Coast, in the north-west of Spain. 10 locations were considered for this study; 8 coming from the 44-year hindcast wind, sea level and wave dataset, and 2 from *in-situ* wave buoy measurements. Additionally, 8 more points along the Galician coast were considered for means of comparison to the Death Coast area. It was found that the Death Coast showed the greatest energy potential in this area, with wave power of the order of 50 kW/m with maximums surpassing 1700 kW/m.

Akpınar and Kömürcü investigated the wave energy potential along the south-east coasts of the Black Sea. The study considered 7 points adn six-hourly data from a SWAN model covering the years 1995-2009. The results obtained from the model were validated using buoy data and then the energy potential was extracted. The majority of points indicated an annual wave energy of 6 MWh/m, while the Sinop point registered an annual wave energy of 10 MWh/m. In this study, annual and seasonal variations were also considered.

Sierra et al. [68], investigate the wave energy potential along the Atlantic coast of Morocco using a 44-year series of hindcast data from a third-generation wave model. In this case, 23 points were considered for the characterisation of the wave energy potential, with a resulting average annual wave power and energy of 30 kW/m and 262 MWh/m, respectively. The temporal variability was also investigated on an annual, monthly and seasonal scale, which resulted in a distinct seasonal pattern. In this study, a multi-criteria analysis was considered for the identification of a potential WEC location. This approach considered: the wave energy at a point, WEC capacity factor, energy temporal variability, distance to the coast, and water depth.

Lisboa et al. [69], investigate the wave energy potential in the south of Brazil using the numerical simulation Mike 21 SW spectral model. The study investigated the nearshore and offshore energy potential and variability. The model used considered a 10-year hindcast dataset. The nearshore points exhibited similar annual wave power, with the maximum reaching 6.7 kW/m; the wave power offshore reached a value of 22.3 kW/m. The annual, seasonal and monthly variability were also investigated, resulting in moderate and high variability, offshore and onshore, respectively. The prominant directions of wave propagation were south and north-east for the offshore case, and south-south-east and east for the nearshore case.

Though these works consider different areas, datasets and approaches, they all consider two important wave parameters; SWH and average period, among other things. As will be described in Chapter 3, these two parameters allow for the calculation of the wave power, which then can be used to find the wave power of the required period of time. Additionally, most of the studies ([64, 65, 66, 67, 68, 69]) consider also the wave direction, where either the values for SWH, peak period, or power (or all) are characterised by their direction of occurrence through directional histograms. The directionality of the wave power is imporant in the implementation of direction-dependant WECs.

2.6   Studies on Maltese waters

The first attempt to quantify the wave climatology in Maltese waters was that carried out by the Physical Oceanography Unit (PO-unit) as part of the Interreg IIIB MEDOCC WERMED Project [70], focused primarily on the Sicilian Channel and the Maltese Islands [9]. At the time, there were no *in-situ* measurements being taken in the area, and so, the approach was that

of numerical wave modelling [9]. The analysis considered three different grid runs of the WAM model; one grid over the Mediterranean with resolution 0.5°, and two nested grids on the eastern and central Mediterranean with resolutions of 0.25° and 0.125°, respectively [9]. Hourly values at every grid point were obtained for a 44-year period which allowed for a description of the wave variability, both spatial and temporal, to be obtained [9].

The PO-unit also took part in an initial feasibility study, headed by the company Seabased, through the deployment of a series of underwater wave buoys around the Maltese archipelago, meant to quantify the wave resource [9].

The Blue Ocean Energy project aimed to test the feasibility of extracting the energy resource around the Maltese islands, in the coastal areas, using the proposed DEXAWAVE converter; the project then required the testing of this new technology [71]. The PO-Unit then set out to make an assessment of the wave potential around the Maltese islands, through measurements using a Datawell [72] wave buoy and numerical modelling techniques [9]. The wave models considered were the Malta MARIA WAM model with a resolution of 0.125°, with a nested Malta SWAN model with a resolution of 0.002° in order to better simulate the coastal areas [9]. The model was fine-tuned using the *in-situ* buoy data, which was also used for data validation [9]. The resulting analysis of the wave resource showed a strong seasonality, with wave power reaching 13.15 kW m^{-1} in Winter, just above 6 kW m^{-1} in Spring and Autumn, and less than 1.72 kW m^{-1} in Summer [9].

The CALYPSO HF radar system, which initially consisted of four radar stations (two in Malta and two in Sicily), was subject to several validation and system performance exercises after its installation in order to be able to ensure a better quality of data output from the system [4]. The measurements used to validate the data were those acquired for near-surface

velocity measurements using Lagrangian drifters and ADCP current profilers [4]. The validation results were found to be consistent with other such exercises carried out for different networks [4].

The first analysis of the CALYPSO HF radar system, which at the time still consisted of four stations, was carried out in 2018 [73]. The HF radar measurements are beneficial since they cover a larger area of sea for data extraction. The main focus of the analysis was to compare the HF data obtained to the output from wave models and altimetry data during a period of extreme wave conditions as a first attempt to test the HF radar measurements in this area due to theoretical limits imposed by the technology at higher wave heights (associated with the capability of the inversion of the second-order spectrum) [73]. It has been shown, through this study, that the limitation was not a very fixed one, and the measurements were obtainable and valid at even more energetic wave conditions [73]. The data collected from the HF radar experiences degradation, spikes, and even data gaps due to corruption of the electromagnetic signal [74]. In particular, for the case of the CALYPSO system, daily strong interference has been noted at the 13.5 MHz frequency, which actively affects the HF outputs [74]. For the sake of quality control, then, a Hidden Markov Model sequence model is implemented in order to reconstruct the missing data by considering the other points in the time sequence output by the radar system; this is a very powerful tool for the processing of the SWH data [74].

The HIPOCAS (Hindcast of Dynamic Processes of the Ocean and Coastal Areas of Europe) was a project that spanned from June 2000 to May 2003, and was aimed at obtaining a 40-year hindcast of wind, wave, sea-level and current climatology for European waters and coastal seas [75, 76]. The resulting product could then be utilised for coastal and environmental decision processes [76]. The project consisted of seven work packages covering: 1)

atmospheric data, 2) circulation models, 3) wave hindcasting, 4) remote sensed data, 5) uncertainty of assessment data, 6) atlas of met-ocean data for European waters and coastal seas, and 7) management, dissemination and exploitation [76]. The atmospheric data was the first step of the project in order to be able to use the resulting 50 km × 50 km grid to feed into the wave and ocean models [76]. The resulting model had a forecasting resolution of 10 km in the spatial domain and 3 hrs in the temporal domain [76]. The participating parties in this project consisted of Instituto Superior Técnico (Portugal), Clima Maritimo, Puertos del Estado (Spain), GKSS Forschungszentrum (Germany), Méteómer (France), University College Cork (Ireland), University of Malta (Malta), Bulgarian Academy of Sciences (Bulgaria), and University of Gdansk (Poland) [76].

Since there are now more HF radars installed on the Maltese islands, along with more data having been collected over the years, further validation and assimilation with models and other data is now possible. Such exercises should be undertaken periodically in order to update the models and such to the current situation.

2.7 Summary

This section will summarise the information presented in this Chapter, and outline the salient points to this work.

Firstly, wave data acquisition systems were defined. These belong to two main groups: *in-situ* and remote sensing devices. For the case of *in-situ* devices, the working principles for wave buoys, and acoustic waves and current profilers were described. The same was done for the remote sensing devices, where X-band radar HF radar, satellite, and synthetic aperture radar were

described. The devices utilised in this work are the wave buoy, HF radar, and satellite.

Wave models and wind forecast models were also outlined in this Chapter. In the case of wave models, the third generation wave model WAM was described, along with its input source terms. The relevance of this generation of wave model is that it is the one generally in use nowadays. In the case of wind models, these are important due to their forcing of wave models, and so, different approaches to the forecasting of this parameter have be discussed.

The importance of validation and assimilation with regards to data is discussed; validation measures give indications as to how well one data set compares to another, while assimilation takes reliable measurements and includes them in the calculation of model outputs. Some details are given about the two main types of assimilation; sequential and variational. Validation techniques constitute a large portion of this work when comparing the different datasets available, whereas assimilation is relevant in the case of the wave models used.

Different types of classifications of WECs were discussed while also presenting the nine WECs considered in this work. These devices were the following: Archimedes, Wavebob, Aquabuoy, Wavestar C6, Wave Dragon, CECO, SeaPower, OEbuoy, and Pelamis. Their working principles and specifications were presented.

The main outputs and results from several studies, obtained from literature, investigating wave power potential in different locations were presented. These generally constituted of using the SWH and wave period to extract the power; most of such studies also carry out directional analysis of the wave power. Lastly, different studies carried out on Maltese waters are pre-

45

sented and discussed. In combination, these last two sections allows for the staring point of this work to be identified and for comparison with available literature treating the same area of the Maltese Islands.

CHAPTER 3

METHODS

In this Chapter, the different methods of analysis used are described. Firstly, in Section 3.1, the calculation of the distance between two points on the earth's surface is described. In Section 3.2, the correlation relations used, as well as other comparative parameters which give further significance to these correlations, are explained. In Section 3.3, the algorithms used to estimate the power potential, and to calculate the WEC output and the MCA index, are described.

3.1 Orthodromic distance

In order to be able to compare point data from buoy and satellite missions to model data, the closest grid cell from the model can be found by finding the smallest orthodromic distance between the data point and the grid cell; this distance is also known as the great circle distance. Figure 3.1 illustrates the problem, where the closest grid cell (blue point) to the required point (green cross) must be determined.

In order to calculate this distance, the Haversine formula is used;
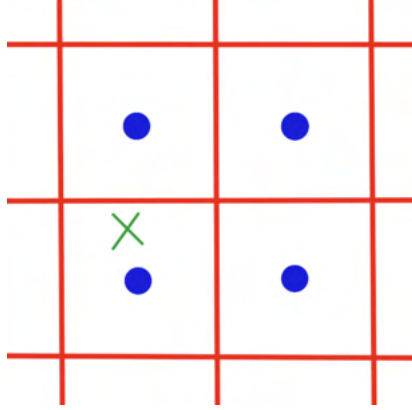
FIGURE 3.1: *Illustration of the closest grid cell problem*

$$a = \sin^2\left(\frac{\Delta\phi}{2}\right) + \cos\phi_1 \cdot \cos\phi_2 \cdot \sin^2\left(\frac{\Delta\lambda}{2}\right) \tag{3.1}$$

$$c = 2 \cdot \mathrm{atan2}\left(\sqrt{a}, \sqrt{1-a}\right)$$

$$d_O = R \cdot c,$$

where ϕ_i is latitude of point i, λ_i is longitude of point i, $\Delta\phi$ and $\Delta\lambda$ are the differences between the two points of latitude and longitude, respectively, and R is the radius of the earth (6371 km), where d_O is the required distance in meters [77].

3.2 Correlations and error metrics

3.2.1 Correlations

Several correlations were evaluated for different combinations of datasets. When evaluating these relations, some were forced to have a zero intercept, while others were not. m and c are used to represent the slope and intercept, respectively; the subscript 0 is used to indicated the forced zero intercept

case.

Forced-zero intercept

For this case, the slope of the best fit line was calculated by

$$m_0 = \frac{\sum_{i=1}^{n} x_i y_i}{\sum_{i=1}^{n} x_i^2}, \tag{3.2}$$

where n is the number of elements, and x_i and y_i are the ith elements of their respective datasets X and Y. Thus the relation is expressed as

$$y = m_0 x \tag{3.3}$$

Non-zero intercept

For this case, the slope of the best fit line was calculated by

$$m = \frac{\sum_{i=1}^{n} (x_i - \overline{x})(y_i - \overline{y})}{\sum_{i=1}^{n} (x_i - \overline{x})^2} \quad [78], \tag{3.4}$$

where $\overline{x}$ and $\overline{y}$ are the mean values of the elements of their respective datasets X and Y. The intercept is calculated as

$$c = \overline{y} - (m \times \overline{x}). \tag{3.5}$$

Thus the relation is expressed as

$$y = mx + c \tag{3.6}$$

Coefficient of determination (R^2)

For the calculation of the coefficient of determination, the calculation of Total Sum of Squares (TSS) along with that of Residual Sum of Squares (RSS) is required. TSS is given by

$$TSS = \sum_{i=1}^{n} (y_i - \bar{y})^2 \,, \tag{3.7}$$

while RSS is given by

$$RSS = \sum_{i=1}^{n} (y_i - \hat{y}_i)^2 \,, \tag{3.8}$$

where $\hat{y}_i$ is the ith predicted value from the model (i.e the result from Equations 3.3 and 3.6, in this case) [79].

The coefficient of determination is then calculated using the following expression,

$$R^2 = 1 - \frac{RSS}{TSS}. \tag{3.9}$$

This value is to be interpreted as how well the model, in this case a straight line, fits the data; the coefficient varies from 0 to 1, with values closer to 1 indicating a better fit [79]. However, a negative value for R^2 can result from regression. This is usually the result of a bad model-fit through the forcing of a value for the intercept, such as forcing a zero-intercept; in such a case, the mean value of the data is better at representing the relationship than the model under test [80].

The correlation coefficient (R)

For the calculation of the correlation coefficient, the MATLAB function `corr2()` was utilised. This function is capable of calculating the correlation coefficient of two two-dimensional inputs. It implements the following algorithm

$$R = \frac{\sum_{i=1}^{n} \sum_{j=1}^{m} (x_{ij} - \overline{x})(y_{ij} - \overline{y})}{\sqrt{\sum_{i=1}^{n} \sum_{j=1}^{m} (x_{ij} - \overline{x})^2} \sqrt{\sum_{i=1}^{n} \sum_{j=1}^{m} (y_{ij} - \overline{y})^2}} \quad [81], \qquad (3.10)$$

which reduces to the following in the one-dimensional case

$$R = \frac{\sum_{i=1}^{n} (x_i - \overline{x})(y_i - \overline{y})}{\sqrt{\sum_{i=1}^{n} (x_i - \overline{x})^2} \sqrt{\sum_{i=1}^{n} (y_i - \overline{y})^2}}. \qquad (3.11)$$

This coefficient represents the correlation between two datasets in that it indicates whether it is positive or negative, and how strong it is.

3.2.2 Error Metrics

Other parameters were calculated in order to obtain more statistical information regarding the relationship between the two sets of data under consideration, as described in Section 3.2.1. The parameters considered were obtained from Rusu and Raileanu [82], which were utilised in a similar analysis. The following are the expressions used and their description.

The mean error, referred to as the bias is given by the Equation,

$$\text{Bias} = \frac{\sum_{i=1}^{n} (y_i - x_i)}{n}, \qquad (3.12)$$

where this value represents the average bias between the corresponding values in datasets X and Y.

The MAE is given by

$$\text{MAE} = \frac{\sum_{i=1}^{n} |y_i - x_i|}{n}, \tag{3.13}$$

where the result can only be positive in this case, as opposed to the bias Equation in 3.12, since the positivity or negativity of the error between the values is being ignored.

The RMSE is given by

$$\text{RMSE} = \sqrt{\frac{\sum_{i=1}^{n} (y_i - x_i)^2}{n}}, \tag{3.14}$$

where this value is an absolute measure of how accurately the simulated values are predicted when compared to measured values; the lower this value is, the better the prediction is by the model [83]. When not comparing simulated and measured values, this measure shows how well the two datasets match.

The values of these parameters are related by the inequalities:

$$\text{Bias} \leq \text{MAE} \leq \text{RMSE} \quad [84]. \tag{3.15}$$

The SI is given by

$$\text{SI} = \frac{\sqrt{\sum_{i=1}^{n} (y_i - x_i - \text{Bias})^2}}{\overline{Y}} \tag{3.16}$$

3.2.3 Probability Density

Another quantitative estimate of the similarity between two datasets is the probability density of the values for either dataset. This can be computed by binning the data and plotting the value of the bin against the associated probability density. The probability density function is obtained using the MATLAB `histcounts()` function, where the normalisation was set to `pdf`. The function calculates the output value v_i for the ith bin according to the Equation

$$v_i = \frac{c_i}{N \cdot w_i},\tag{3.17}$$

where c_i is the number of elements in the bin, w_i is the width of the bin, and N is the number of elements in the input data [85].

3.2.4 SWH Threshold Analysis

It is is important to know how well a model can predict certain SWHs over specified thresholds [27]. In such a threshold analysis, the model is tested against an accurate source of wave data, such as buoy data, in order to establish the following:

1. The Probability of Detection (PD) by the models

2. and the Probability of False Alarm (PFA) (i.e the probability that a calculated above threshold value by the model is actually below the threshold)

In order to calculate these values, the following relations are used,

$$PD = \frac{\text{no. of } O \text{ events detected by } M}{\text{no. of events detected by } O} \times 100 \qquad (3.18)$$

$$PFA = \frac{\text{no. of } M \text{ events not detected by } O}{\text{no. of events detected by } M} \times 100 \qquad (3.19)$$

where 'events' refers to an occurrence of a SWH above the threshold value, O refers to the accurate source of wave data, and M refers to the model data under inspection.

3.3 Power Potential Calculations

The mechanical energy of a propagating wave, including both kinetic and potential energies, per unit surface area and averaged over a wave period, is given by

$$E = \frac{1}{8}\rho g H^2, \qquad (3.20)$$

where ρ is the liquid density, g is the acceleration due to gravity and H is the wave height [1]. The power of a wave can then be represented by the Equation

$$P = C_g E, \qquad (3.21)$$

where C_g is the group velocity of the wave, which is the partial derivative of the dispersion relation (σ) with respect to the wave number (k) [1]. σ is given by the Equation

$$\sigma = \sqrt{gk \tanh kd}, \tag{3.22}$$

resulting in a group velocity given by

$$C_g = \frac{\partial \sigma}{\partial k} = \frac{\sigma}{2k} \left[1 + \frac{2kd}{\sinh 2kd} \right], \tag{3.23}$$

where d is the still water depth [1].

Equation 3.23 considers a single monochromatic wave, in reality, sea waves are irregular and consist of several wave frequencies [1]. Irregular sea states can be broken down into multiple sine waves that are representative of the resulting state. Conversely, an irregular wave can be constructed from different sine waves [1]. Then, the energy from each sine wave must be added to produce the total energy:

$$E = \frac{1}{8} \rho g \sum_{i=1}^{N} H^2 \quad [1]. \tag{3.24}$$

Going a step further, the total energy can be expressed as follows for irregular waves

$$E_{\text{tot}} = \int_0^\infty E(\sigma) d\sigma, \tag{3.25}$$

which describes a continuous energy density spectrum, where $E(\sigma)$ is the energy density spectrum. This can be done by decomposing the time series into a great number of sine waves, such that the frequency difference between them approach zero [1].

The variance density spectrum $S(\sigma)$ is defined as

$$E(\sigma) = \rho g S(\sigma) \quad [1]. \tag{3.26}$$

Defining the moment of the variance density spectrum, with the rth moment being given by

$$m_r = \int_0^\infty \sigma^r S(\sigma) d\sigma, \tag{3.27}$$

is useful for the calculation of statistical wave properties, such as the significant wave height H_s, which is defined as the average of the top 1/3 of the wave heights in a time series, which can be expressed in moments by the following

$$H_s = 4\sqrt{m_0} \quad [1]. \tag{3.28}$$

The total wave energy can now be expressed as

$$E_{\text{tot}} = \rho g m_0 = \frac{1}{16} \rho g H_s^2, \tag{3.29}$$

by Equations 3.25, 3.26 and 3.27 [1].

The wave power can now be expressed as

$$P = \rho g \int_0^\infty C_g(\sigma) S(\sigma) d\sigma, \tag{3.30}$$

which is difficult to implement when considering C_g as expressed in Equation 3.23 [1]. To mitigate this, the deep water condition, where d is a very large value, is considered, resulting in the following approximation of C_g for deep

water

$$C_g = \frac{1}{2}\sqrt{\frac{g}{k}} = \frac{g}{2}\frac{1}{\sigma} = \frac{gT}{4\pi}, \qquad (3.31)$$

where T is the wave period [1]. Combining Equations 3.30 and 3.31, and using the definition of the moments (Equation 3.27), the wave power can expressed as

$$P = \frac{1}{2}\rho g^2 m_{-1}. \qquad (3.32)$$

Considering the parameter T_E to be the speed of propagation of wave energy, C_g can be expressed as

$$C_g = \frac{gT_E}{4\pi}, \qquad (3.33)$$

by Equation 3.31, which when combined with the expression for E_{tot} in Equation 3.29 as dictated by Equation 3.21, results in the following expression of wave power

$$P = \frac{1}{64\pi}\rho g^2 T_E H_s^2 \approx 479 T_E H_s^2. \qquad (3.34)$$

By equating Equations 3.32 and 3.34, and by the definition of H_s (Equation 3.28), T_E can be expressed as:

$$T_E = 2\pi\frac{m_{-1}}{m_0}. \qquad (3.35)$$

The two methods of obtaining the wave power described here are the spec-

tral method, Equation 3.30, and the statistical method, Equation 3.34. In general, for the latter method, the deep water condition assumed for the wave energy calculations, are often met by the WEC [1].

When calculating the power, sometimes the energy period T_E is unavailable as output of a model or from the measurements. However, the peak period T_p is most of the time available. In cases when T_E is to be estimated, it can be done using the Equation

$$T_E = \alpha T_p, \tag{3.36}$$

where α depends on the shape of the wave spectrum; a value of $\alpha = 0.86$ describes a Pierson-Moskowitz spectrum, while $\alpha = 0.90$ is considered a more conservative value and describes a standard JONSWAP spectrum with peak enhancement factor $\gamma = 3.3$ [86]. In this work, when T_E is unavailable, a value of $\alpha = 0.90$ is assumed.

3.3.1 MATLAB Application

The implementation of Equation 3.34 in the MATLAB environment to find the power and energy at a specific geographical point, is now described.

In order to create a statistical representation of the sea state, the bivariate histogram function, `histogram2` [87], is used to convert time-series data to a matrix representation. The function is used to bin the values of SWH (H_s) and energy period (T_E) into a two-dimensional histogram. The bin widths of H_s and T_E are taken to be 0.5 m and 1 s, respectively, such that the last bin contains the largest value in the data. The smallest bin mid-points are taken to be 0.25 and 1 for H_s and T_E, respectively. α_{ij} is then calculated as

follows,

$$\alpha_{ij} = \frac{M_{ij}}{N_t},$$ (3.37)

where M_{ij} is the number of data points in the ith T_E and j^{th} H_s bin, and N_t is the total number of data points in the time series. The power is then calculated, by Equation 3.34, using the following algorithm:

$$P = \sum_i \sum_j 0.479 \cdot T_i \cdot H_j^2 \cdot \alpha_{ij},$$ (3.38)

where T_i and H_j represent the mid points of the bins for T_E and H_s, respectively; this calulation outputs the power in kW / m. In order to obtain the energy value from P over a time t_h, where the time is given in hours, the following calculation is made

$$E = P \cdot t_h,$$ (3.39)

where E is in kWh.

Using this method, different time-spans of data can be used to represent the average power over that specific time-span. For example, 24 data points of hourly data can be used to produce a singular 24-hour averaged power representative of that one day's sea states. In the case when the hourly values of the power and energy are required (for hourly data), the above calculation is done without the involvement of α_{ij}, since the power can be directly computed from the values of H_s and T_E by Equation 3.34.

3.3.2 Variability

Measuring the variability of the wave resource and parameters is an important undertaking for the determination of a suitable location for the installation of a WEC.

One of the more straightforward measures which can be utilised to quantify the temporal variability of the wave power is that of the Coefficient of Variation (COV) [86]. This is given by,

$$COV = \frac{1}{\bar{x}} \sqrt{\frac{\sum_{i=1}^{n} x_i^2 - \left(\sum_{i=1}^{n} x_i\right)^2 \big/ n}{n-1}}, \tag{3.40}$$

where x_i is the ith element of the time series, $\bar{x}$ is the mean value of the time series, and n is the total number of elements [88]. In the ideal case when $COV = 0$, there is no variability present [68]. A value in the range $0.85 - 0.9$ would be indicative of an area of moderate variability, and those areas with values > 1.2 experience high variability; the lower this value is, the more suitable the area is for wave energy exploitation due to energy stability [68, 88].

Other measures that are able to quantify the variability of the wave energy resource are the monthly and seasonal index; the benefit of this type of measure is that the variability can be captured in a singular value [86]. The Seasonal Variability Index (SV) is defined in [86] as

$$SV = \frac{P_{S1} - P_{S4}}{P_{\text{yr}}}, \tag{3.41}$$

where P_{S1} and P_{S4} are the mean wave power for the most and least energetic seasons, respectively, and P_{yr} is the mean annual power. Similarly defined,

the Monthly Variability Index (MV) is defined as

$$MV = \frac{P_{M1} - P_{M4}}{P_{\text{yr}}},\tag{3.42}$$

where P_{M1} and P_{M4} are the mean wave power for the most and least energetic months, respectively. It is expected that the monthly variability index is higher than the seasonal one; values < 1 indicate moderate seasonal variability [68].

These values were introduced by M. Cornett in [86] as a new means, one easy to compute, of quantifying the seasonal and monthly variation of the wave power.

3.3.3 WEC power output

The wave power output from any specific WEC will vary according to several different parameters, as discussed in Section 2.4. The power available in the sea cannot be all converted to electricity through the use of WECs; the output power of WECs are described by their power matrices that give the power output for different combinations of H_s and T_E/T_p. In order to calculate the output power of a particular point from time-series data, the following procedure is followed.

Firstly, as discussed in Section 3.3.1, a statistical representation of the sea state is obtained by using the bivariate histogram function, `histogram2`. However, in this case, as shown in Table 2.1, the bin centres and widths will depend on the resolution of the WEC power matrix under consideration and the period is either the energy period (T_E) or the peak period (T_P), depending on the power matrix. Given then that $\mathcal{P}_{ij}$ represents the elements

of the WEC power matrix at the mid points T_i and H_j of the T_E/T_p and H_s bins, respectively, the output WEC power is found to be

$$P_{\text{WEC}} = \sum_i \sum_j \mathcal{P}_{ij} \cdot \alpha_{ij}, \tag{3.43}$$

where α_{ij} has the same meaning as in Section 3.3.1.

3.3.4 Multi-Criteria Approach

The MCA index that is based on the work by Kamranzad and Hadadpour [41], is now described.

The idea behind the definition of this index is to create a comparative tool for the selection of a WEC and its location by considering several different aspects that makes a WEC suitable or not; the index thus includes other measures apart from energy output alone. The MCA index defined by Kamranzad and Hadadpour [41] is as follows,

$$\text{MCA} = \left(\frac{\frac{E_e}{2000} \times accessibility \times availability \times \frac{E_0}{10000} \times \frac{5}{H_{s_{100}}}}{MVI_{E_0}} \right), \tag{3.44}$$

where E_e is the exploitable storage of wave energy, given by

$$E_e = P_{\text{mean}} \times t_e, \tag{3.45}$$

where t_e is the total number of hours where the wave power exceeds $2\,\text{kW/m}$, and P_{mean} is the mean wave power.

The terms *accessibility* and *availability* are not related to the performance of WECs, but rather to the sea condition. *Accessibility* is a measure of how suitable the area is for Operational and Maintenance (O&M) purposes; it is the percentage of time when $H_s < 1.5$ m in this case [41]. *Availability* is a measure of how often the sea state favours energy production; it is the percentage of time when $0.5 < H_s < 4$ m, which is a generalised range for WEC cut-in and cut-off H_s values [41].

E_0 is the annual energy yield from the WEC, that is, $P_{\text{WEC}} \times 8760$. MVI_{E_0} is the monthly variability index of the WEC output energy and is calculated in a similar way to the MV, Equation 3.42, but the monthly averaged wave power is substituted for the WEC monthly averaged output energy. $H_{s_{100}}$ is the design wave height and represents the design cost at the location under consideration. This parameter will be ignored in this work, and so, the MCA index will be defined as

$$\text{MCA} = \left(\frac{\frac{E_e}{2000} \times accessibility \times availability \times \frac{E_0}{10000}}{MVI_{E_0}} \right), \tag{3.46}$$

for the upcoming calculations.

CHAPTER 4

DATASETS

In this Chapter, the datasets considered in this work are described. The model, remotely sensed, and *in-situ* datasets are described in Sections 4.1 and 4.2, respectively. In Section 4.3, the model grids, buoy position, and other relevant positions are plotted atop bathymetry data for the purpose of investigating the possible error sources between the datasets because of varying sea-bed depths.

4.1 Models

In this work, two different wave model data products were considered; Copernicus and ROSARIOSWAN data. These datasets were both used in two ways. The first, the extraction of time series data at specific coordinates for comparison with buoy data or for isolated analysis, and the second, the use of a range of coordinates to illustrate spatial variation of different parameters.

4.1.1 Copernicus Model

The gridded dataset used in this work from Copernicus was the 'Mediterranean Sea Waves Analysis and Forecasting Product' [89]. The data used, `med-hcmr-wav-an-fc-h` from product `MEDSEA_ANALYSISFORECAST_WAV_006_-017`, is hourly instantaneous data for the variables summarised in Table 4.1. The model is forced by 10m ECMWF above-sea-surface winds, and uses an optimal interpolation scheme with the available along-track satellite SWH observations by CMEMS [90].

Table 4.1: *Copernicus model output variables*

Name	Description	Standard Name	Units
VHM0	Spectral significant wave height (Hm0)	sea_surface_wave_significant_height	m
VTM10	Spectral moments (-1,0) wave period (Tm-10)	sea_surface_wave_mean_period_from_variance_spectral_density_inverse_frequency_moment	s
VTM02	Spectral moments (0,2) wave period (Tm02)	sea_surface_wave_mean_period_from_variance_spectral_density_second_frequency_moment	s
VTPK	Wave period at spectral peak / peak period (Tp)	sea_surface_wave_period_at_variance_spectral_density_maximum	s
VMDR	Mean wave direction from (Mdir)	sea_surface_wave_from_direction	degree
VPED	Wave principal direction at spectral peak	sea_surface_wave_from_direction_at_variance_spectral_density_maximum	degree
VSDX	Stokes drift U	sea_surface_wave_stokes_drift_x_velocity	m s^{-1}
VSDY	Stokes drift V	sea_surface_wave_stokes_drift_y_velocity	m s^{-1}
VHM0_WW	Spectral significant wind wave height	sea_surface_wind_wave_significant_height	m
VTM01_WW	Spectral moments (0,1) wind wave period	sea_surface_wind_wave_mean_period	s
VMDR_WW	Mean wind wave direction from	sea_surface_wind_wave_from_direction	degree
VHM0_SW1	Spectral significant primary swell wave height	sea_surface_primary_swell_wave_significant_height	m
VTM01_SW1	Spectral moments (0,1) primary swell wave period	sea_surface_primary_swell_wave_mean_period	s
VMDR_SW1	Mean primary swell wave direction from	sea_surface_primary_swell_wave_from_direction	degree
VHM0_SW2	Spectral significant secondary swell wave height	sea_surface_secondary_swell_wave_significant_height	m
VTM01_SW2	Spectral moments (0,1) secondary swell wave period	sea_surface_secondary_swell_wave_mean_period	s
VMDR_SW2	Mean secondary swell wave direction from	sea_surface_secondary_swell_wave_from_direction	degree

Based on the WAM Cycle 4.6.2, the output grid data is the result of a fine grid nested in a larger grid, which spans 75°W to 10°E in longitude and 70°N to 10°S in latitude with resolution 1/6° [90]. The spatial coverage of the nested finer dataset spans from longitude 18.125°W to 36.2917°E and latitude 30.1875°N to 45.9792°N with a spatial resolution of 1/24°, approximately 4.6km, which is illustrated in Figures 4.1 and 4.2 [90].
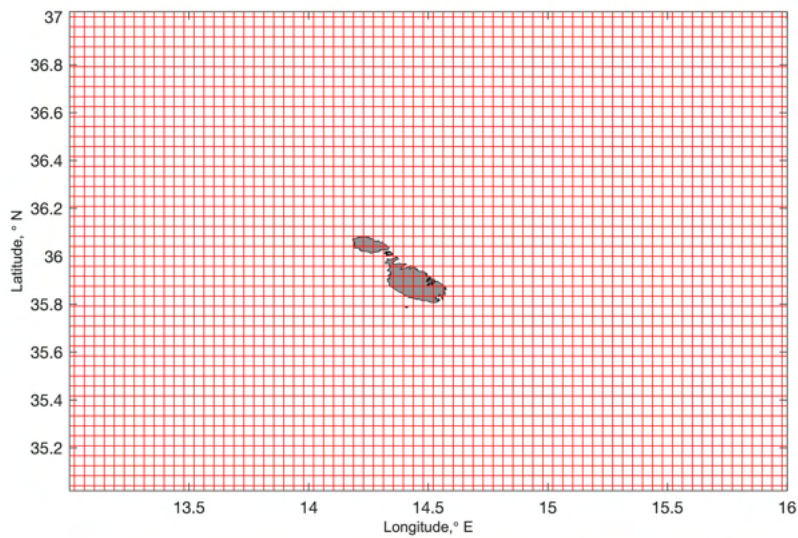
FIGURE 4.1: *Copernicus Model Grid of the entire spatial domain considered overlaying the Maltese Archipelago*

Both the analysis and forecast are updated twice daily in this wave product at 06:00 UTC and 20:00 UTC; the forecast horizon is that of ten days [90].

The spatial subset considered here is, unless other wise stated, that data which spans from longitude 13°E to 16°E and latitude 35°N to 37°N.
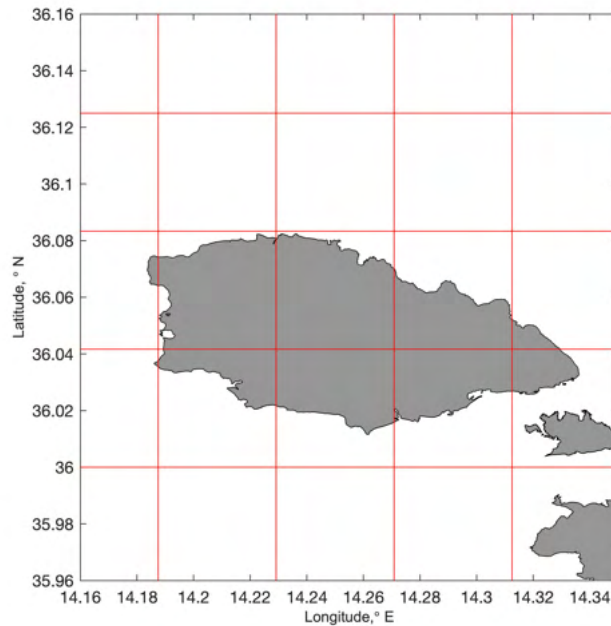
FIGURE 4.2: *Copernicus Model Grid zoomed in to the Gozo region*

4.1.2 ROSARIOSWAN

The third-generation wave model ROSARIOSWAN used in this work is a SWAN model which is nested in the Copernicus model; the model covers the Malta Shelf Area, which includes the sea between Malta and Sicily and is a model which has yet to undergo extensive validation. The two variations of the model considered here are one forced by the SKIRON atmospheric forecast and the other by the MARIA atmospheric forecast.

The model covers an area bounded by $35.376°-37.124°$N in latitude and $13.75°-15.45°$E in longitude with a spatial resolution of $1/500°$. This is shown in Figure 4.3 and the grid sizes are equivalent to about 0.2km.

Unlike the case for Copernicus Model, the grid for the entire domain cannot be visualised due to the much higher resolution of the ROSARIOSWAN dataset, making the grid lines indiscernible; the increased resolution can be
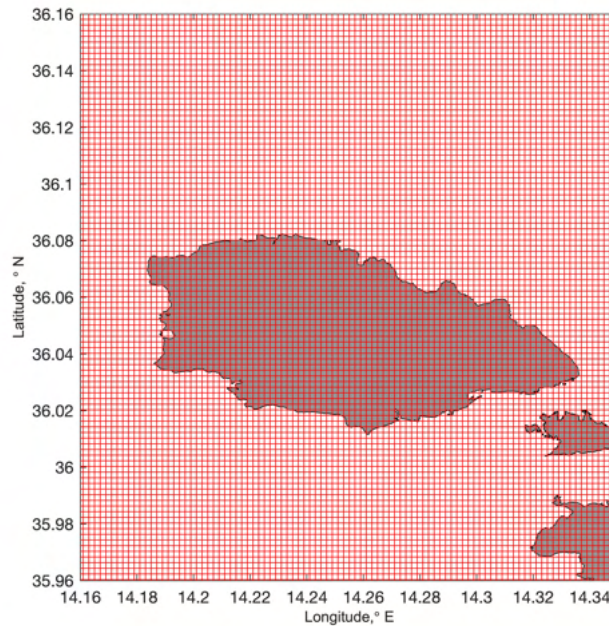
FIGURE 4.3: *ROSARIOSWAN Model Grid zoomed in to the Gozo region*

noted when comparing Figures 4.2 and 4.3.

ROSARIOSWAN data constitutes of hourly data of the variables summarised in Table 4.2. The model produces an hourly forecast for 2.5 days, starting at midnight of the first day and ending at noon two days later [91]. This data was provided by the Physical Oceanography Research Group [92], which falls under the Department of Geosciences at the University of Malta.

TABLE 4.2: *ROSARIOSWAN output variables*

Name	Standard Name	Units
hs	sea_surface_wave_significant_height	m
tp		s
tm01	sea_surface_wave_mean_period_from_variance_spectral_density_first_frequency_moment	s
theta0	sea_surface_wave_from_direction	degrees
depth	sea_floor_depth_below_sea_level	m
hswe	sea_surface_swell_wave_significant_height	m

69

4.2 In-situ and remote sensing

4.2.1 Buoy

The buoy deployed off the Maltese coast of Marsalforn, Gozo (36.081N, 14.2816E) is a Directional Wave Spectral Drifter (DWSD) developed by the Scripps Institution of Oceanography's (SIO) Lagrangian Drifter Laboratory [93]. This buoy returns both directional wave spectra data, along with sea surface temperature in real time, and is a cost effective solution for wave measurements. The DWSD, Figure 4.4, is a 35cm spherical float which measures orbital wave motion with remote user-programmable sampling window [93, 94]. Data is stored on board the DWSD, that has up to 16GB of internal storage, but can also communicate remotely and send data in real-time via the Iridium short burst data telemetry system. [94]. The DWSD has been shown to be an accurate wave parameter measurement device, and is easily deployable [95].

By measuring the time-series of the vertical, zonal and meridional velocity components, w, u and v, respectively, the power spectral density, co-spectra and quadrature-spectra can be derived through Fourier transformations [96]. Given that the directional variance spectra of each sea-state is expressed by the truncated Fourier series,

$$S(f,\theta) = \frac{a_0}{2\pi}\left[1 + 2\sum_{m=1}^{2}(a_m\cos(m\theta) + b_m\sin(m\theta))\right], \qquad (4.1)$$

the DWSD is able to output the first five coefficients (a_0, a_1, a_2, b_1 and b_2) from 0.03-0.50 Hz with a bandwidth $\Delta f = 1/256$ Hz; from these coefficients, the wave parameters can be obtained [96]. The mean wave direction and the principle wave direction, θ_1 and θ_2, respectively, are given by the following
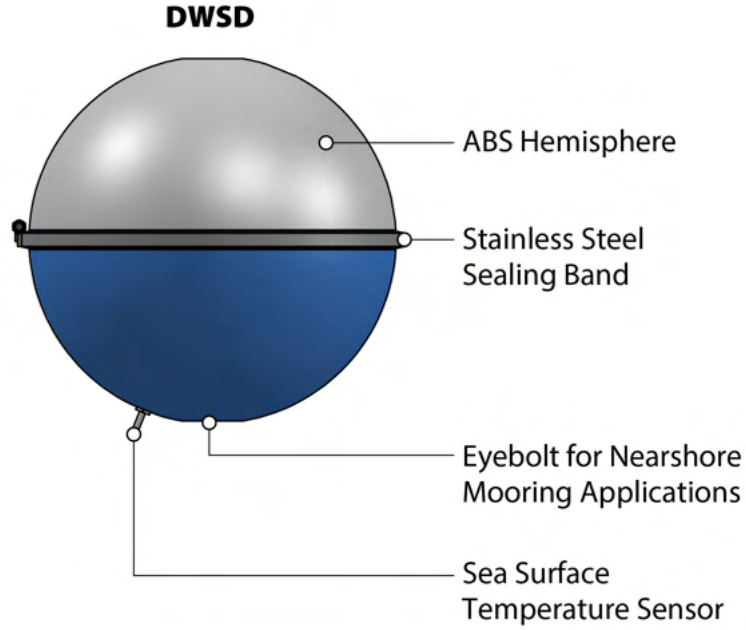
FIGURE 4.4: *Schematic of the Directional Wave Spectra Drifter [Image by SIO]*

equations,

$$\theta_1 = \arctan\left(\frac{b_1}{a_1}\right), \tag{4.2}$$

and

$$\theta_2 = \frac{1}{2}\arctan\left(\frac{b_2}{a_2}\right) \quad [96]. \tag{4.3}$$

The expression for the SWH, given previously by equation 3.28, is found by considering the following summation for m_0:

$$m_0 = \pi \Delta f \sum_{n=1}^{N_b} a_{0,n}, \tag{4.4}$$

where N_b is the number of bands in the frequency range [96]. Similarly, m_1

is expressed as

$$m_1 = \pi \Delta f \sum_{n=1}^{N_b} f_n \cdot a_{0,n}, \qquad (4.5)$$

such that the mean period can be calculated as,

$$T_m = \frac{m_0}{m_1} \quad [96]. \qquad (4.6)$$

f_p is defined as the center frequency of the non-directional spectral band with maximum spectral density; the peak period can then be expressed as

$$T_p = \frac{1}{f_p} \quad [96]. \qquad (4.7)$$

The wave peak direction is given by

$$D_p = \arctan\left(\frac{b_1}{a_1}\right)_{f=f_p} \quad [96]. \qquad (4.8)$$

The dataset from the DWSD that has been acquired for use in this work consists of the following parameters:

- Date and time

- Latitude (°)

- Longitude (°)

- Sea temperature (°C)

- SWH (m)

- Wave direction (°)

- Dominant wave period (s)

- Mean wave period (s)

The dataset available from this buoy spans over one year from 04/08/2020 08:00 to 12/07/2021 06:00. Measurements of the wave parameters by this instrument are no longer being made since the buoy drifted away from its anchored point on the 23/10/2021 and ceased to transmit its location on 09/11/2021 [97]. This data was provided by the Physical Oceanography Research Group [92].

4.2.2 HF Radar

The station used in this work from the CALYPSO HF radar system, described in Section 2.6, is the SOPU station, located at 36.0563667°N and 14.3084000°E. In particular, the second annular ring, located at a radius of 5.85144 km, is considered here as this is the closest measurement to the buoy position, see Figures 4.5 and 4.6 [98]. Wave height, mean period, and direction are measured by the radar every 10 minutes; the radar also produces measurements for wind direction and height standard deviation.

The available dataset for this radar station spans from 01/01/2020 to 19/11/2021. However, there are many erroneous entries for the annular ring required in this work. In addition to this, there is a gap of data due to malfunction of the HF Radar after being struck by lightning. As a result of this, only 817 points are available for this whole period, which, when averaged on the hour, result in a total of 339 data points. This data was also provided by the Physical Oceanography Research Group of the University of Malta [92].

4.2.3 Satellite

In order to compare the data from different satellite missions with other datasets, the satellite data 'GLOBAL OCEAN L3 SIGNIFICANT WAVE HEIGHT FROM NRT SATELLITE MEASUREMENTS' [99] was considered. The satellite data product used, `WAVE_GLO_WAV_L3_SWH_NRT_OBSER-VATIONS_014_001`, gives altimetry measurements of SWH along the satellite tracks of the Saral/AltiKa (al), Cryosat-2 (c2), CFOSAT (cfo), Hai Yang-2B measurements (h2b), Jason-3 (j3), Sentinel-3A (s3a) and Sentinel-3B (s3b) missions [100]. The dataset also gives the 10-meter wind speed [100]. In upcoming analyses, the data from s3a has been omitted.

4.3 Bathymetry

When comparing datasets, the proximity of model data points to measured data locations is important to note for the establishment of possible error sources. Increased distance between measurement and model leads to higher variation in the underlying bathymetry; this variation in depth adds to the errors when the model and *in-situ* data are compared. In order to visually inspect these features, the plots of the respective grids and data points used for either wave model are plotted over EMODnet Bathymetry data [101] (in case of the ROSARIOSWAN data, the bathymetry data displayed is a combination of EMODnet and survey data which was provided by the Physical Oceanography Research Group [92]), along with the position of the buoy (as described in Section 2.1.1) and the second HF radar annular ring. The resulting plots are given in Figures 4.5 and 4.6.

In order to select the closest model data point to the buoy, the orthodromic distance between the data positions and buoy position was calculated, as de-
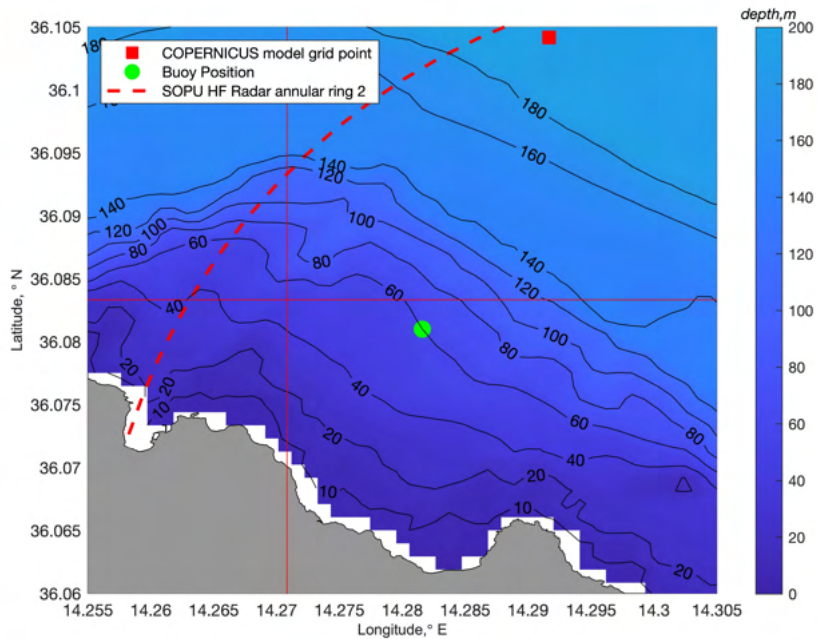
FIGURE 4.5: *Copernicus Model grid, grid point utilised, buoy position and SOP HF Radar second annular ring overlaying bathymetry data*

scribed in Section 3.1. The cell that was found to have the smallest distance, and which corresponded to a valid point in the land/sea mask, was considered. The resulting model points from this process are (36.1042N, 14.2917E) and (36.0812N, 14.282E) for the Copernicus and ROSARIOSWAN models, respectively. Given the higher spatial resolution of the ROSARIOSWAN data, the grid point chosen is much closer to the buoy position than the grid point chosen from the Copernicus data. The result of this is that a larger variation in depth exists for the case of the Copernicus model data. Looking at Figure 4.5 for the Copernicus model, the buoy is located on the 60 m depth isoline, whereas the model point is located between the 180 and 200 m depth isoline; this indicates a difference of at least 120 m between the two points. Looking at Figure 4.6 for the ROSARIOSWAN model, the buoy and model grid point are in very close proximity when compared to the Copernicus Model case; indeed, both points are close to the 60 m isoline,
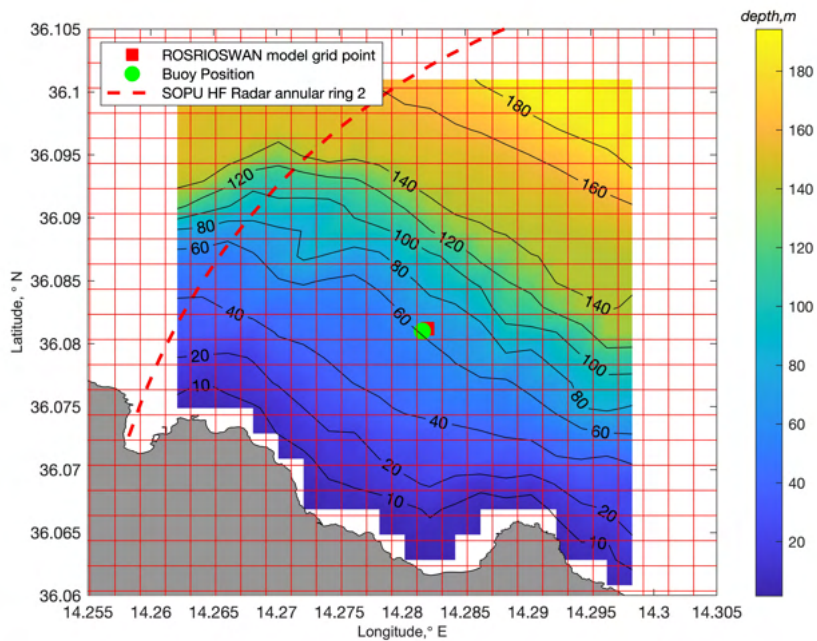
FIGURE 4.6: *ROSARIOSWAN model grid, grid point utilised, buoy position and SOP HF Radar second annular ring overlaying bathymetry data*

and the difference in depth is less than 20 m.

For the case of the SOPU radar annular ring, it can be noted that this measurement area crosses several bathymetric isobars, since, the radar outputs only one value per annular ring. The output measurement is then sampled from a sea state with increased bathymetric variation, and so, this can be a source of error in the output.

CHAPTER 5

RESULTS AND DISCUSSION

In this Chapter, the results from the investigations carried out in this study are presented and discussed. In Sections 5.1-5.4 the comparative methods described in Section 3.2 are applied in order to investigate the relationship between the different datasets described in Chapter 4. Results of the wave power available at the buoy position as well as over mapped regions are presented in Section 5.5 and their respective variability results in Section 5.6. Finally, in Section 5.7, the WEC power outputs are presented along with an MCA analysis. The code and data used in this analysis can be accessed through the link `http://ioi.research.um.edu.mt/staff/martina/SeaWavesDataAnalysis.zip`; the documentation can be found through the link `http://ioi.research.um.edu.mt/staff/martina/documentation.pdf`.

5.1 Data Comparison: Buoy vs Models

In this Section, the relationship between the buoy measurement dataset and the numerical models under consideration, are investigated.

5.1.1   Buoy vs Copernicus Model

Using the Copernicus Model time-series data from the grid point as described
in Section 4.3, and as illustrated in Figure 4.5, a temporal comparison be-
tween the buoy data and Copernicus model can be made. The data being
compared here is the SWH, wave direction, mean period, and peak period;
the time series of these are overlaid for visual inspection as shown in Figure
5.1. In addition, the probability density of each of the parameters from both
datasets were overlaid for ease of comparison; the resulting distributions are
given in Figure 5.2.

From the time series and probability density plots, some information can
already be obtained regarding the relationship between the two datasets.
Starting from the SWH and wave direction parameters, one can note that
the relationship between the datasets in this case show a relatively good
agreement where, the time series and probability densities tend to overlap
quite well. One can note from Figure 5.2b, that there are two clear peaks
in the data, which correspond to, roughly, the East and North-West direc-
tions. Looking at the mean period, one can note, from both the time series
and probability distribution plots, that the Copernicus model data seems to
correlate to the buoy data, albeit with a downwards shift. From Figure 5.2c,
one can observe that the peak of the Copernicus data occurs at ~ 3.5 s and
that of the buoy data at ~ 5.2 s. Finally, in the case of the peak period, not
much can be inferred from Figure 5.1d. However, Figure 5.2d has a bit more
to offer. From the probability density plot, it can be noted that, for the
case of Copernicus, the peak curve is similar to that of the buoy data. It is,
however, the case that the Copernicus data points are concentrated between
0 and 10 s, whereas the buoy plot has a lower peak with values beyond 10
s; there are no values beyond 15 s belonging to the Copernicus model data.
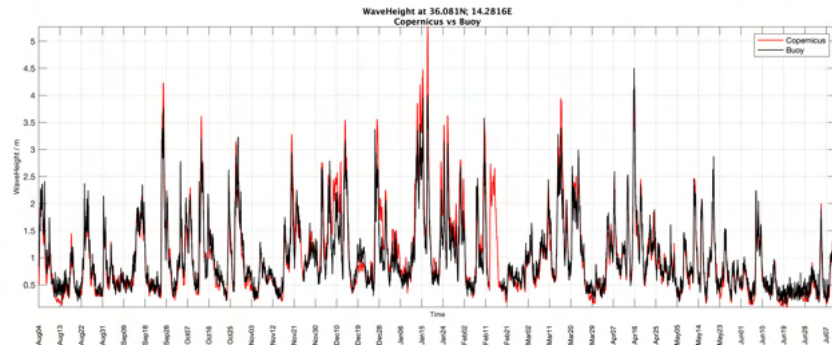
(A) *Significant Wave Height*
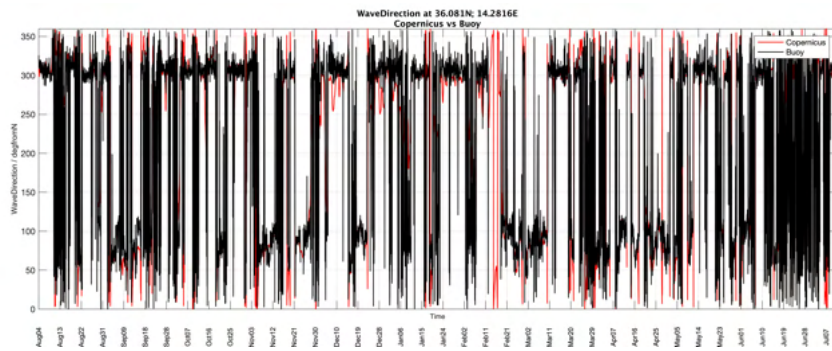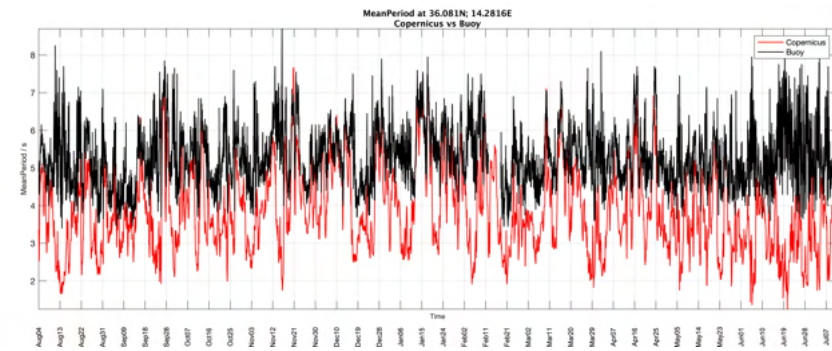
(B) *Wave Direction*
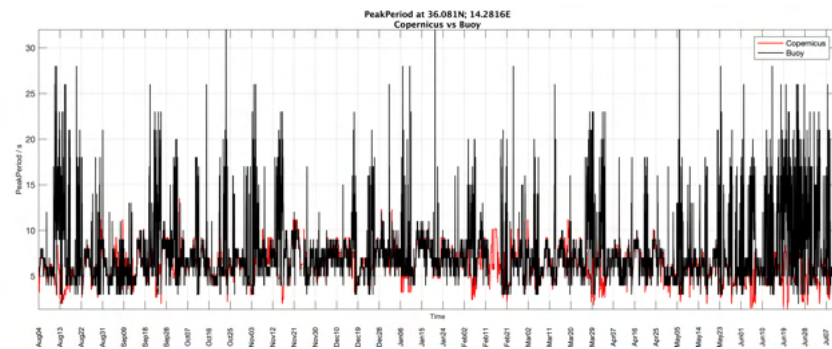
(C) *Mean Period*

(D) *Peak Period*

FIGURE 5.1: *Copernicus model (red) and Buoy (black) time series data from August 4th 2020 to July 12th 2021*

79
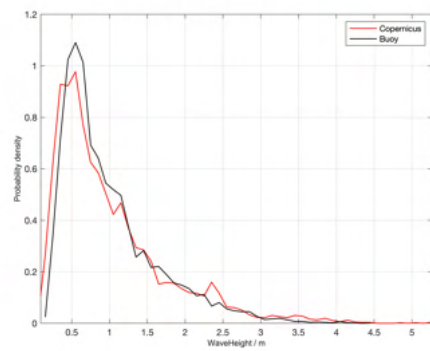
(A) *Significant Wave Height*
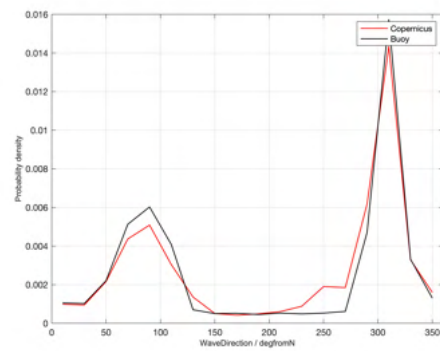
(B) *Wave Direction*
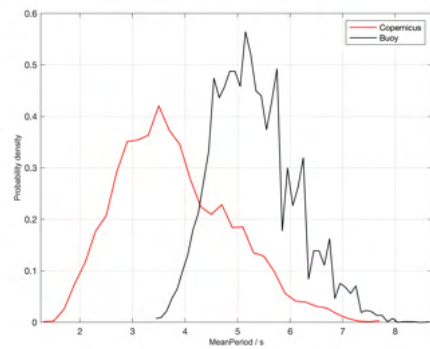
(C) *Mean Period*
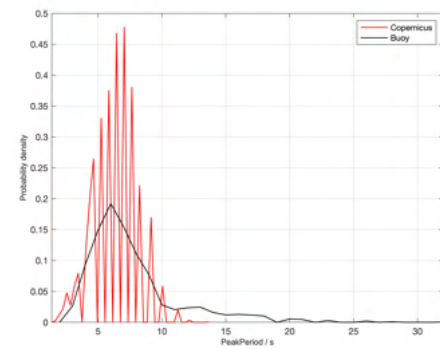
(D) *Peak Period*

FIGURE 5.2: *Probability Density of Copernicus model (red) and Buoy (black) data*

Correlation and other error metrics were computed for these datasets as described in Sections 3.2.1 and 3.2.2. Scatter plots between each parameter of the dataseries were plotted and linear regression was performed. The resulting plots are given in Figures 5.3 and 5.4 for the forced-zero intercept and non-zero intercept regressions, respectively.

(A) *Significant Wave Height*

(B) *Wave Direction*

(C) *Mean Period*

(D) *Peak Period*
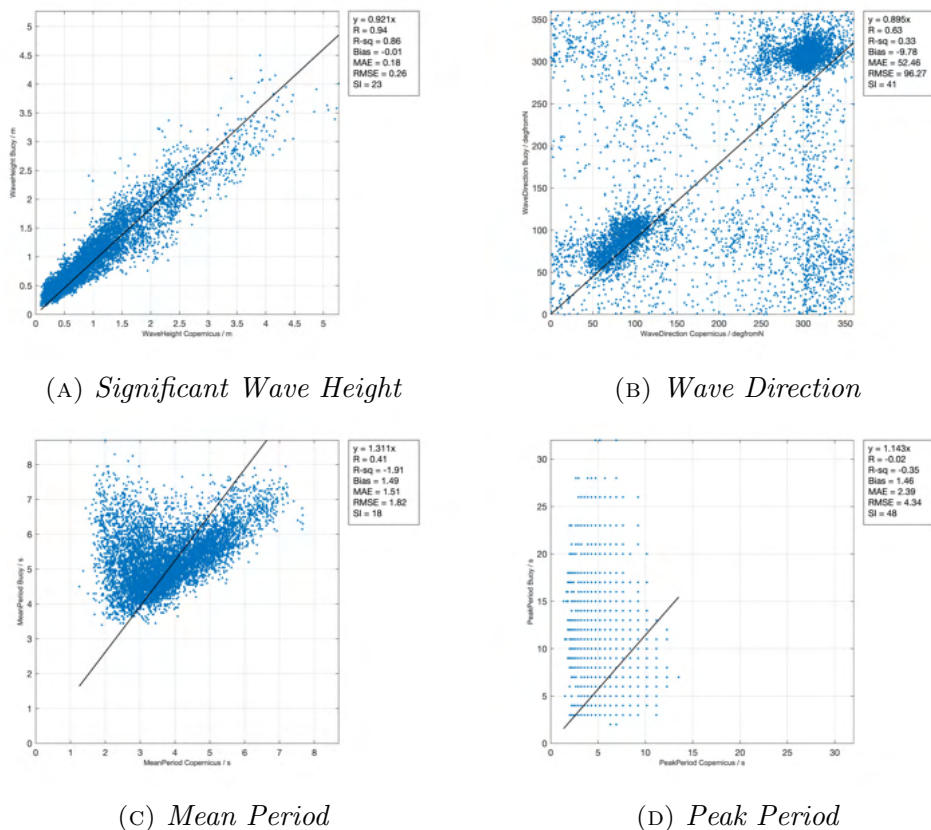
FIGURE 5.3: *Correlation plots between Copernicus model and Buoy; forced-zero intercept regression*

The best linear fit from the four parameters is given by that of the SWH, clearly illustrated in Figures 5.3a and 5.4a; the R^2 values are 0.86 and 0.89, for the forced-zero intercept and non-zero intercept case, respectively. The model fit is then slightly better in the case where there is no forced intercept, indicating an offset of the Copernicus model data from the buoy data. The strong correlation between the two datasets is confirmed with the high correlation value of R that results to be equal to 0.94. Additionally, the

(A) *Significant Wave Height*

(B) *Wave Direction*

(C) *Mean Period*

(D) *Peak Period*
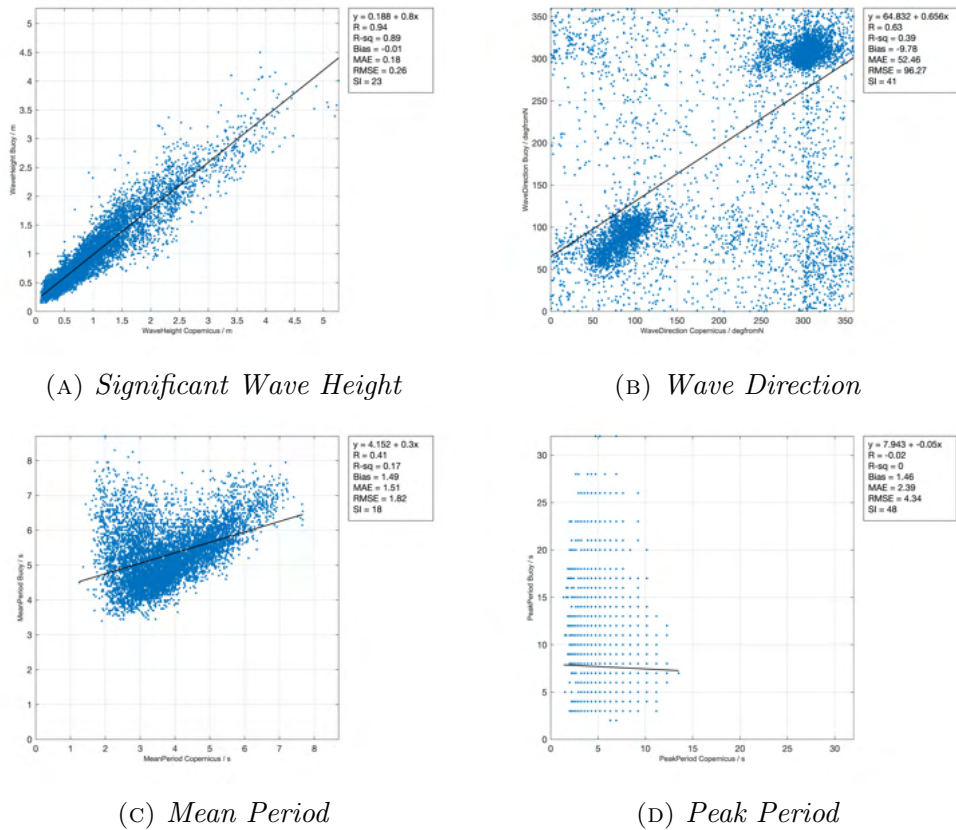
FIGURE 5.4: *Correlation plots between Copernicus model and Buoy; non-zero intercept regression*

good correlation is also supported by the bias, -0.01, and the MAE, 0.18 as well as the RMSE, 0.26. The SI is also not too high a value at 23%.

As can be seen in Figures 5.3b and 5.4b, for wave direction, a concentration of points can be seen in two directions. These are roughly Easterly and North-Westerly, matching the observations made from the probability density plots. The linear fit performs slightly better in the non-zero intercept case, with $R^2 = 0.39$ as opposed to $R^2 = 0.33$, both indicative of a weak relationship. Upon visual inspection, however, in the case of the non-zero intercept, it can be noted that the line almost completely misses the directions, as described above, with high density of points. This result might be due to the high number of scattered points which are the likely cause for the very high MAE

and RMSE, 52.46 and 96.27, as well as a SI of 41%.

It is notable that the line fit for the mean period cases, Figures 5.4c and 5.3c, is especially poor; $R^2 = -1.91$ and 0.17 for the forced-zero intercept and non-zero intercept case, respectively. The negative value of R^2 indicates a poor fit due to the forced intercept, however, not forcing an intercept still results in a low goodness-of-fit, which can be easily seen from Figure 5.4c, where, the V-like distribution of the data points cannot be modelled well using linear regression. The correlation, as reflected by $R = 0.41$, is weak, but the SI is the lowest from all the parameters at 18%, indicating that the variation of each point from the expected error is less than in the case of the SWH. It can also be noted that the bias and MAE are very close in value. This implies that, the difference between the two datasets has mostly the same sign, in this case positive. Therefore, the buoy data is systematically larger than the Copernicus model data; this can be confirmed from Figure 5.1c, where the red lines (Copernicus) have a shift with respect to the black lines (buoy).

The line fit for the peak period cases, shown in Figures 5.4d and 5.3d, is the worst from all cases. This can be visually noted in both scatter plots and from the values of R^2, which is negative for the forced-zero intercept case (-0.35) and 0 for the non-forced intercept case. In terms of the correlation, R gives a slightly negative value, which is reflected in the slight negative slope in Figure 5.3d. The RMSE= 4.34, which is a relatively high value, and this can be explained by noting that the values from the Copernicus model never exceed 15 s, whereas those for the buoy go beyond 30 s, thus resulting in a high error for the higher values. This case has the highest value for SI, 48%, indicating that the bias is not a good representation of the differences found between the two datasets.

Plotting the data, classified according to different parameters

In order to be able to understand better the origin of the features of the scatter plots for the mean period (the V-shape) and the wave direction (background scattered points), the two datasets were plotted such that different subsets of the data were classified based on different parameters; these parameters were

1. Months,

2. Seasons,

3. and SWH,

with the resulting plots given in Figures 5.5, 5.6 and 5.7, respectively.

Noting the plots in Figure 5.5, the colour-coding of points from July 2020 through June 2021 by month showed no clear clustering of points and so, not much could be concluded from these plots. In Figure 5.6, a more general clustering is made by season, where the seasons are taken as follows: Autumn: 14/09/2020 - 30/11/2020, Winter: 01/12/2020 - 29/02/2021, Spring: 01/03/2021 - 31/05/2021, and Summer: 01/06/2021 - 13/09/2021.

This allows for seasonal effects to be noted more clearly rather than considering the individual months. In this case, more information can be obtained from the plots. For the SWH that is shown in Figure 5.6a, one can note that the point values associated with Autumn, Winter and Spring have a larger variability than those belonging to Summer, as these are more localised at smaller wave heights. In the case of Autumn, in the case of higher wave heights, some values scatter more on the upper side of the plot, indicating that the Copernicus model could be potentially slightly underestimating

(A) *Significant Wave Height*

(B) *Wave Direction*

(C) *Mean Period*

(D) *Peak Period*
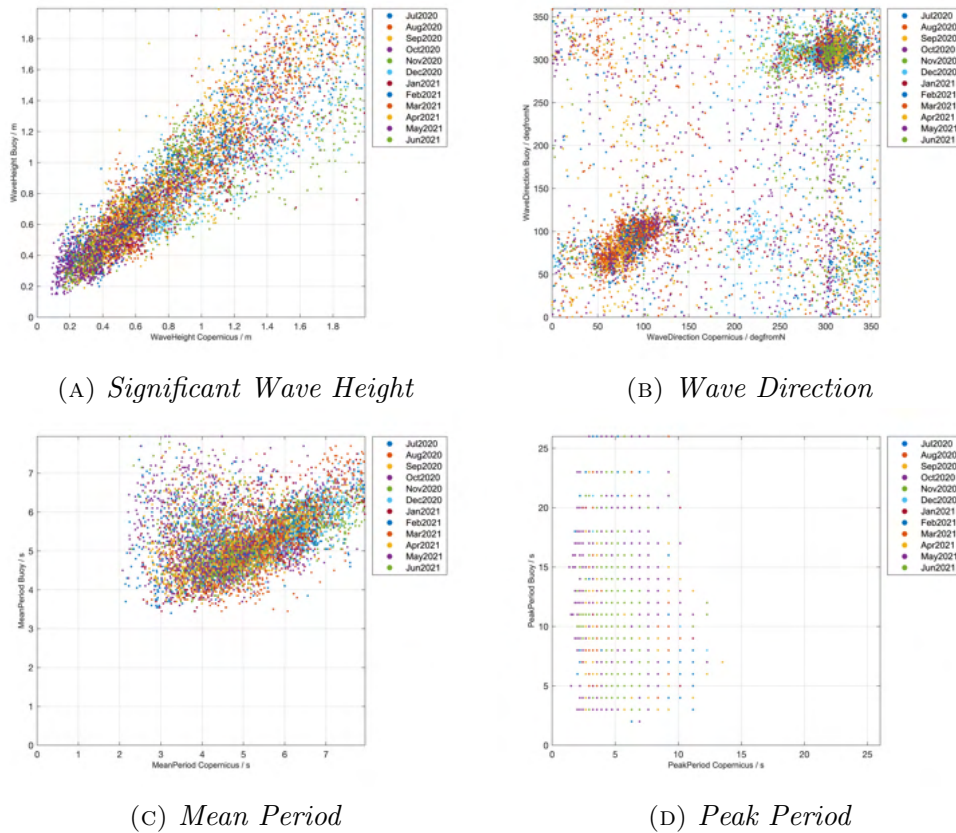
FIGURE 5.5: *Correlation plots between Copernicus model and Buoy; classified by month*

these values. The opposite can be observed for the higher values during Winter, where some values scatter more on the lower side of the plot, indicating that the Copernicus model could be potentially slightly overestimating these values. In the case of Spring, the scattering behaviours is like that of Autumn, albeit with a few points scattering similarly to Winter.

For the wave direction parameter, shown in Figure 5.7b, Winter an Summer winds are predominantly clustered at the NW direction, while Autumn and Spring are more divided between the two dominant directions. The 'background' scattered points are contributed from all the different seasons, however, less so from Winter. For the mean period parameter, Figure 5.6c, not much can be said regarding the different clusters, since all contribute to

(A) *Significant Wave Height*

(B) *Wave Direction*

(C) *Mean Period*
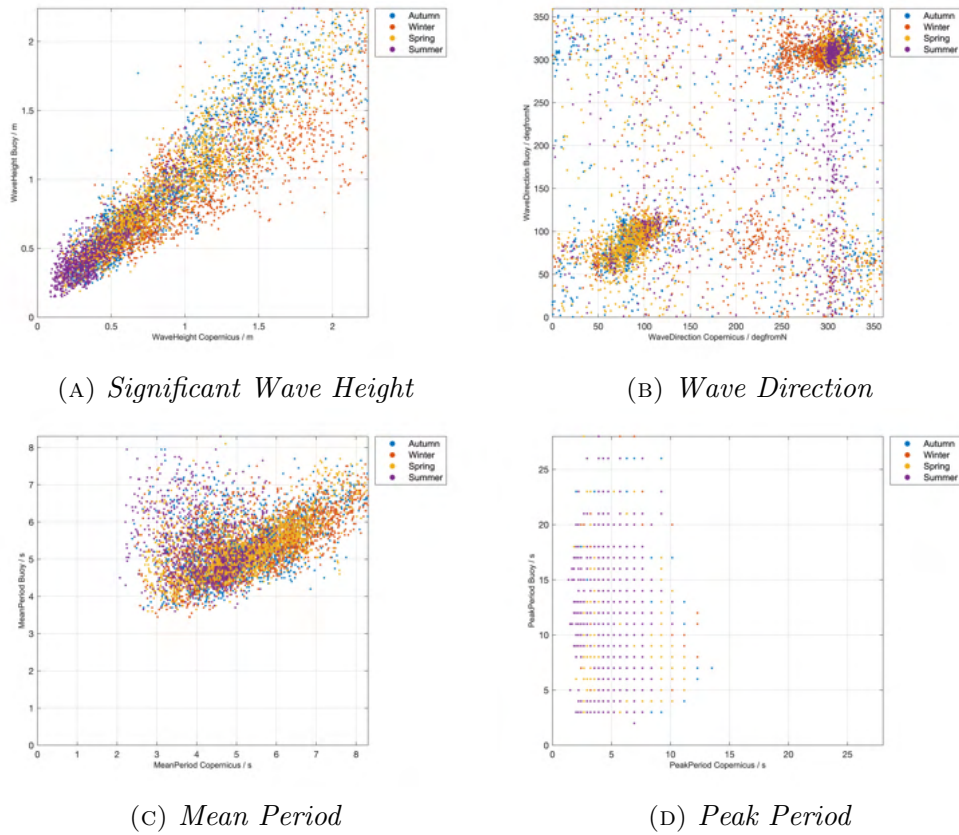
(D) *Peak Period*

FIGURE 5.6: *Correlation plots between Copernicus model and Buoy; classified by season*

the resulting V-shaped plot.

In terms of the peak period, shown in Figure 5.6d, the seemingly more discretised values overlap significantly, making this plot not ideal to assess in terms of clustering.

The clustering according to seasons, however, failed to give more insight into what caused the 'background' scattered points in the mean direction and the V-shaped distribution in the mean period data. In light of this, the clustering according to the SWH comes into play, where clustering was performed in ranges of SWH, increasing with a step of 1m, up to 5m. These plots, shown in Figure 5.7, indeed give some more information regarding the resulting data distributions; the SWH plot, Figure 5.7a, will not be discussed for obvious

(A) *Significant Wave Height*

(B) *Wave Direction*

(C) *Mean Period*

(D) *Peak Period*
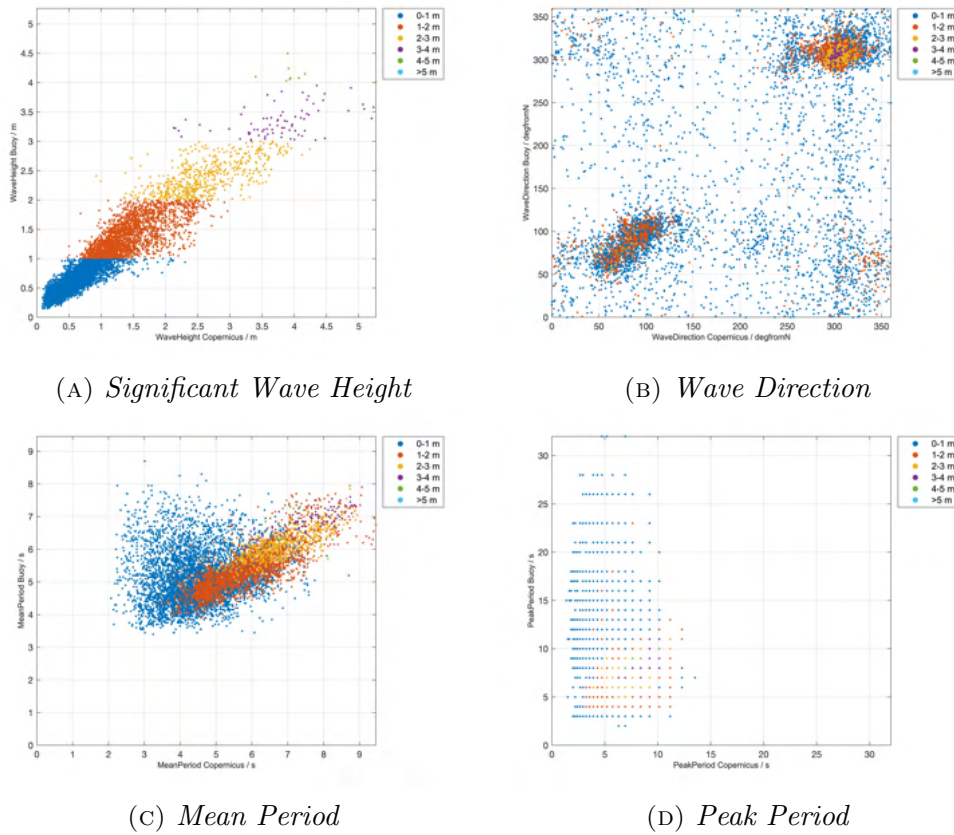
FIGURE 5.7: *Correlation plots between Copernicus model and Buoy; classified by Significant Wave Height*

reasons. Looking firstly at the wave direction case, Figure 5.7b, one can note now, that most of the 'background' scattered points are attributed to wave heights in the 0-1 m range, which suggests that the correlation between the buoy and Copernicus model mean direction data weakens significantly at lower wave heights. Similarly for the case of the mean period, Figure 5.7c, the 0-1 m wave height range significantly contributes to the part of the distribution that alters the linear distribution, again, suggesting that the correlation of the mean period of the smaller wave heights is weak. In the case of the peak period, Figure 5.7d, it can be noted that the points corresponding to the 0-1 m wave height range are more prevalent towards the upper part of the plot. This could be indicative of the Copernicus model data underestimating the peak period measured by the buoy.

Plotting filtered data

Given the above investigation, the SWH is seemingly a significant parameter that affects how well the correlation between the two datasets performs. In this regard, the Copernicus model and Buoy data correlation, regression and measure calculations are carried out again with a dataset excluding the 0-1 m wave height range; the resulting plots are given in Figure 5.8, where a non-zero intercept regression has been carried out. The below comparisons will hence be made with the non-zero intercept plots for the non-filtered case, Figure 5.4.

(A) *Significant Wave Height*

(B) *Wave Direction*

(C) *Mean Period*

(D) *Peak Period*
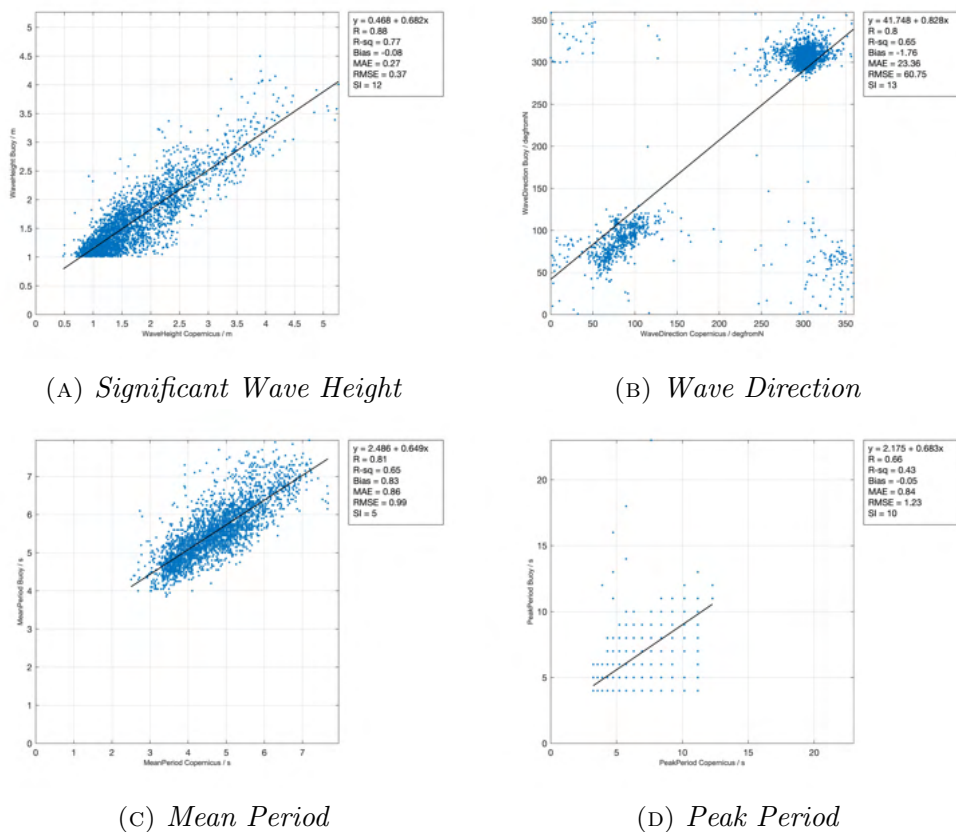
FIGURE 5.8: *Correlation plots between Copernicus model and Buoy; 0-1 m wave height range data points excluded*

Apart from the case of the SWH, the filtering caused overall improved correlations in the wave parameters. In the case of the SWH, Figure 5.8a, all

the measures but the SI are slightly worse, where, SI dropped from 23% to 12%; the measures still, however, indicate a good correlation and linear fit. In the case of the wave direction, Figure 5.8b, it can be clearly noted that the 'background' scattered values have been largely filtered out, with the exception of two small clusters at the top-left and bottom-right of the Figure. These clusters are likely the result of the fact that 0° and 360° are the same and so, small values and large values in the range correspond to similar directions. The value of R increased from 0.63 to 0.8, and the fit better represents the data with an R^2 value of 0.65 (up from 0.39), indicating that the linear regression represents a moderate relationship. Additionally MAE, RMSE and SI all improved with values decreased by approximately 55%, 37% and 68% respectively. The resulting bias is also closer to zero at -1.76.

For the case of the mean period, it can be clearly observed, Figure 5.8c, that the V-shaped distribution has been removed and a more linear plot is obtained. Indeed, the linear fit performs better with and increase in R^2 from 0.17 to 0.65, indicating that the linear regression represents a moderate relationship. The correlation measure R also improved, almost doubly, from a value of 0.41 to 0.81. Additionally MAE, RMSE and SI all improved with values decreased by approximately 43%, 46% and 72%, respectively. The resulting bias is also closer to zero at 0.83.

In the peak period plot, Figure 5.8d, it can also be noted that much of the points associated with the higher peak period values from the buoy dataset have been filtered out, resulting in a less scattered plot. The correlation between the datasets improved, R increased from -0.02 to 0.66, suggesting a moderate relationship. As a result, the linear fit also performed better with R^2 going up to 0.43 from 0. Additionally MAE, RMSE and SI all improved with values decreased by approximately 64%, 72% and 79%, respectively.

The resulting bias is also closer to zero at -0.05. The measure calculations are then most improved in this case, with higher percentage decreases than those in the other parameters.

<div align="center">

SWH Threshold Analysis

</div>

The probability of the Copernicus model being able to detect SWHs above a given threshold is plotted against the probability of it being a false alarm, using the method described in Section 3.2.4, where the model is compared to the buoy data. The resulting plot is given in Figure 5.9, where thresholds are taken from $H_s = 0.5$m to 5m in steps of 0.5m.
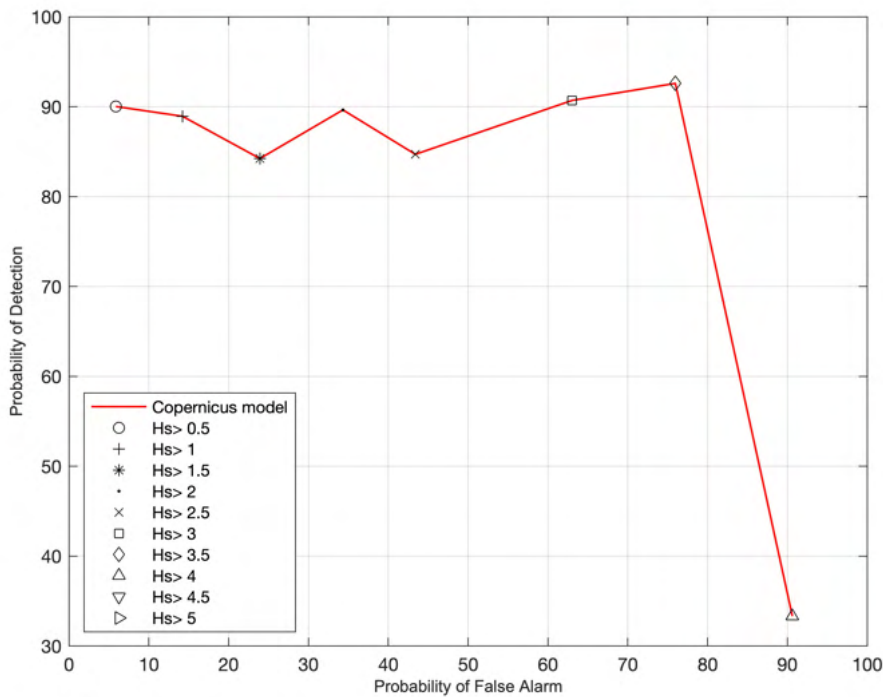
FIGURE 5.9: *Copernicus model Data SWH Threshold Analysis; tested against buoy data*

From this plot, it can be observed that the Copernicus model has a good PD of sea states when thresholds of H_s fall in the range 0.5-3.5; these values all

lie in the 80-95% probability range. With increase in the threshold, however, there is also an increase in the PFA where, from $H_s > 0.5$ to $H_s > 3.5$, this probability goes up from $\sim 5\%$ to $\sim 75\%$. There is then a sudden drop in PD for the case of $H_s > 4$, with a value of $\sim 33\%$ and an associated PFA of $\sim 90\%$; this is likely the result of a small number of events with $H_s > 4$.

5.1.2   Buoy vs ROSARIOSWAN Maria Model

Using the ROSARIOSWAN Maria model time series data from the grid point as described in Section 4.3, and as illustrated in Figure 4.6, a temporal comparison between the buoy data and ROSARIOSWAN Maria model can be made. The data being compared here is the SWH, wave direction, mean period and peak period; the time series of these are overlaid for visual inspection in Figure 5.10. In addition, the probability density of each of the parameters from both datasets were overlaid for ease of comparison; the resulting distributions are given in Figure 5.11.

From the time series and probability density plots, some information can already be obtained regarding the relationship between the two datasets. In this case, it is only in the wave direction parameter that the datasets show a very good agreement; again in this case one can note from Figure 5.11b, that there are two clear peaks in the data, which correspond to, roughly, the East and North-West directions. This is not to say that in the other parameters there isn't a good agreement, but in the cases of the SWH, mean period and peak period, there seems to be an underestimation by the ROSARIOSWAN Maria model when compared to the buoy data. This is represented in a downwards shift in the visual plots and a leftwards shift in the probability density functions. The shape of the data does, however, show a good match.

Looking now at the peaks in the data, from the probability density func-
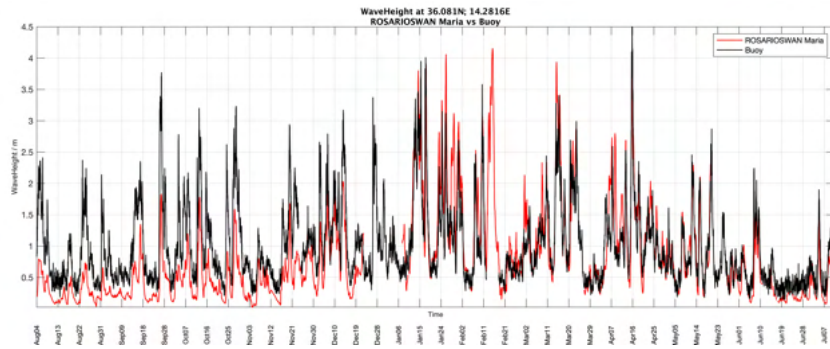
(A) *Significant Wave Height*
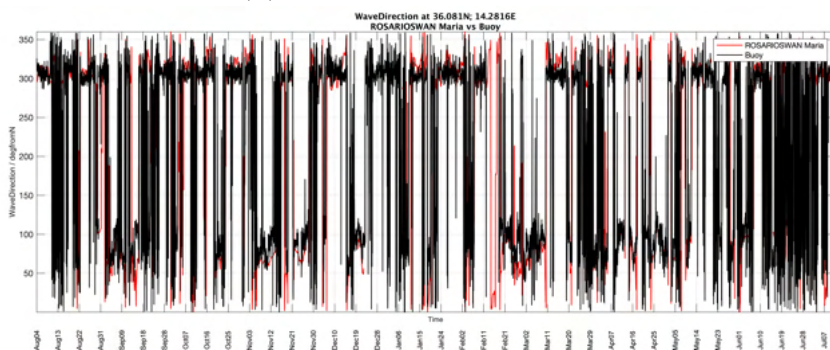
(B) *Wave Direction*
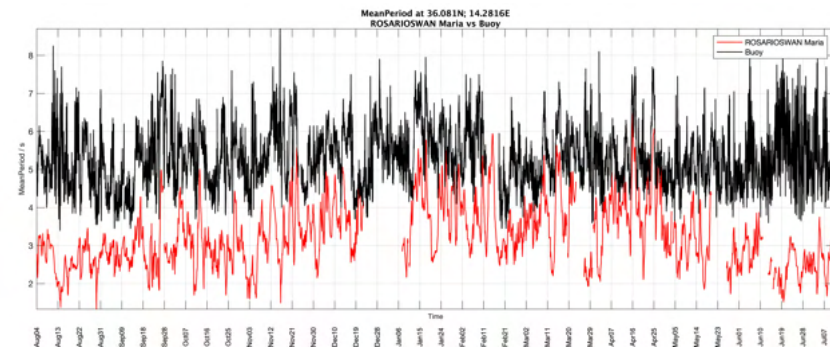
(C) *Mean Period*
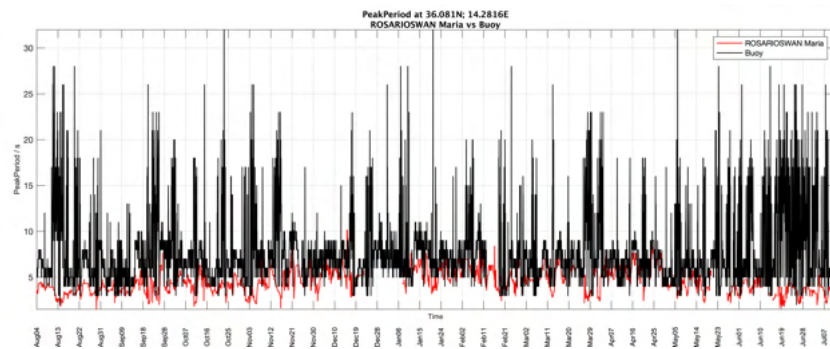
(D) *Peak Period*

FIGURE 5.10: *ROSARIOSWAN Maria model (red) and Buoy (black) time series data from August 4th 2020 to July 12th 2021*

(A) *Significant Wave Height*

(B) *Wave Direction*

(C) *Mean Period*

(D) *Peak Period*
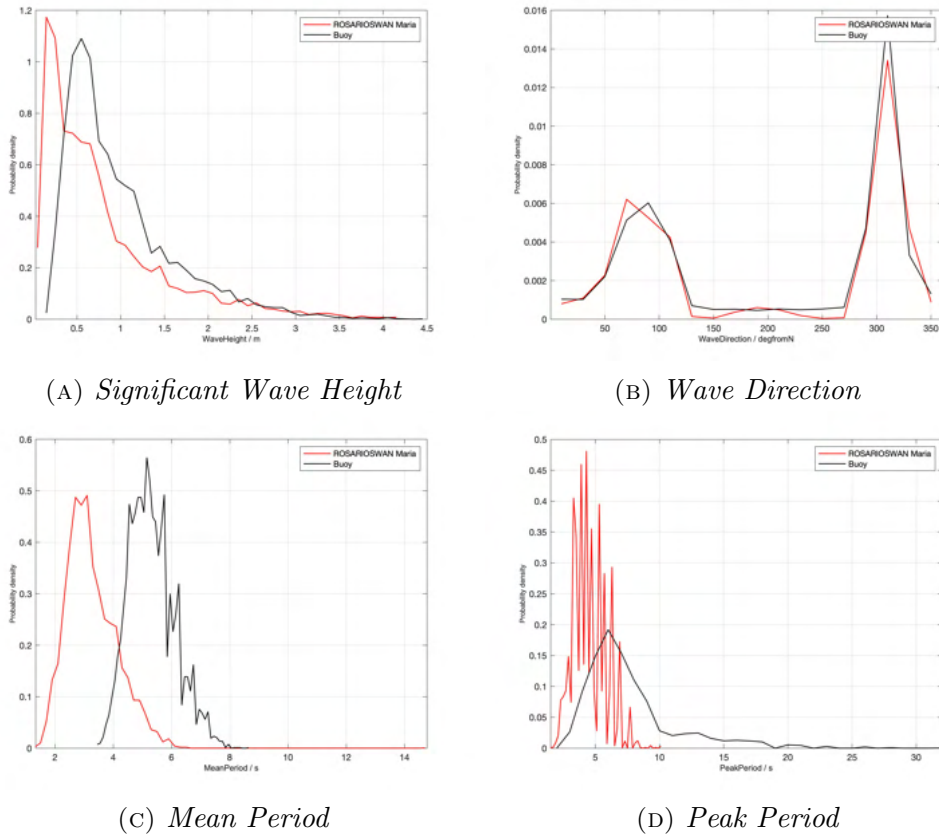
FIGURE 5.11: *Probability Density of ROSARIOSWAN Maria model (red) and Buoy (black) data*

tions, allows for a quantification of these shifts between the two datasets. Starting with the SWH, Figure 5.11a, it can observed that the peak of the ROSARIOSWAN Maria data occurs at ~ 0.17 m and that of the buoy data at ~ 0.55 m. In the case of the mean period, Figure 5.11c, it can observed that the peak of the ROSARIOSWAN Maria data occurs at ~ 3.0 s and that of the buoy data at ~ 5.5 s. Finally, in the case of the peak period, it is more difficult to infer where the peak lies for the ROSARIOSWAN Maria data; it is here considered that this peak is at ~ 4.0 s and that of the buoy data at ~ 6.0 s. Similar to the situation of the Copernicus model data, Section 5.1.1, it is the case that the ROSARIOSWAN Maria data points are concentrated in the area below 10 s, resulting in a higher peak, whereas the buoy plot has a lower peak with some values beyond 10 s; there are no values

beyond 10 s belonging to the ROSARIOSWAN Maria data.

Correlation and other error metrics were computed for these datasets as described in Sections 3.2.1 and 3.2.2. Scatter plots between each parameter of the dataseries were plotted and linear was regression performed. The resulting plots are given in Figures 5.12 and 5.13 for the forced-zero intercept and non-zero intercept regressions, respectively.

(A) *Significant Wave Height*

(B) *Wave Direction*

(C) *Mean Period*

(D) *Peak Period*
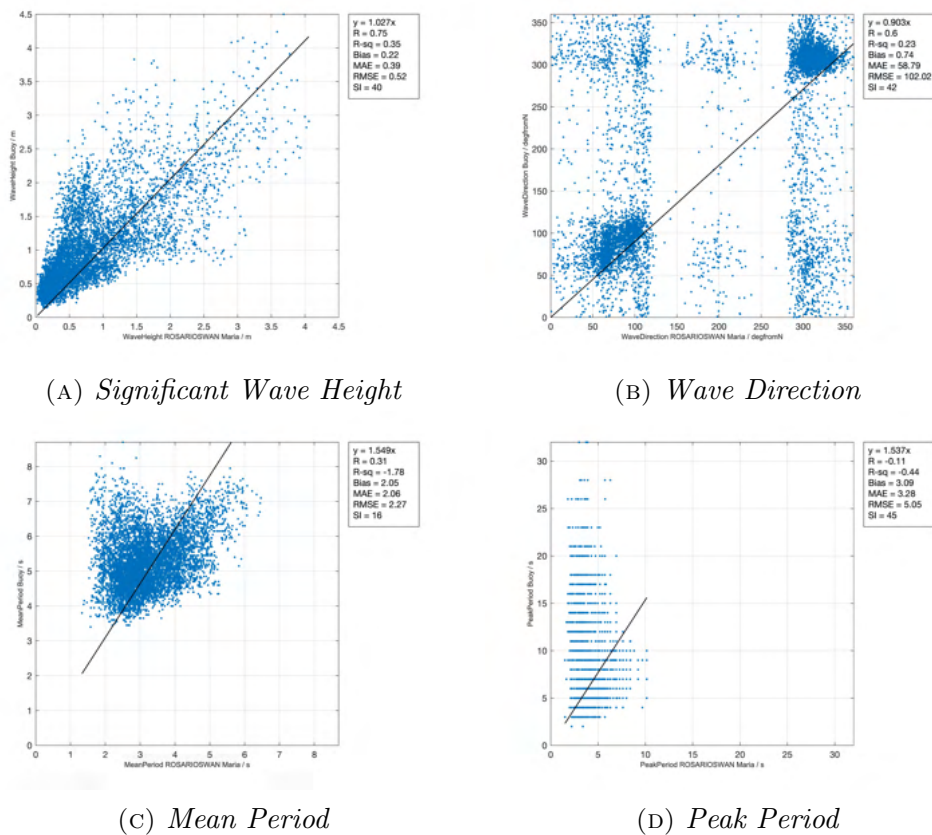
FIGURE 5.12: *Correlation plots between ROSARIOSWAN Maria model and Buoy; forced zero-intercept regression*

The best linear fit from the four parameters is given by that of the SWH, illustrated in Figures 5.12a and 5.13a; the R^2 values are 0.35 and 0.57, for the forced-zero intercept and non-zero intercept case, respectively. Despite this, however, these fits are still relatively weak, given the low values of R^2, with the non-zero intercept case being more of a moderately good fit rather

(A) *Significant Wave Height*

(B) *Wave Direction*

(C) *Mean Period*

(D) *Peak Period*
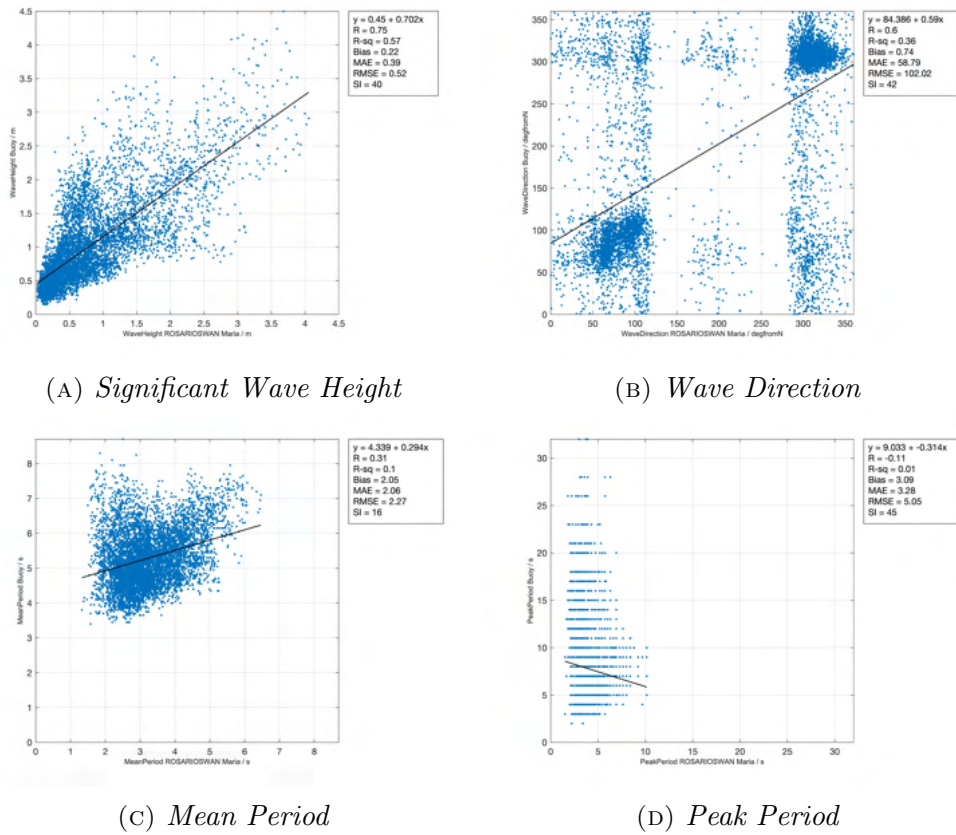
FIGURE 5.13: *Correlation plots between ROSARIOSWAN Maria model and Buoy; non-zero-intercept regression*

than weak. Thus, the model fit is slightly better in the case where there is no forced intercept, indicating an offset of the ROSARIOSWAN Maria data from the buoy data; this is consistent with what was discussed above regarding the offsets in the time-series and probability density function plots; the offset is here equal to 0.45 m. The good correlation between the two datasets is primarily represented in the value of R, 0.75, which shows that there is a relatively well established relationship between them. Additionally, the other parameters of the relationship as given by the bias, 0.22, and the MAE, 0.39 as well as the RMSE, 0.52 are not insignificant given that the maximum data points do not exceed 4.5 m. For the case of the SI, 40%, the high scatter is evident from the plots, which gets worse with increasing SWH value.

For the case of the wave direction, a concentration of points can be again seen in two directions, see Figures 5.12b and 5.13b, which are roughly Easterly and North-Westerly, matching the observations made from the probability density plots. The linear fit performs better in the non-zero intercept case, with $R^2 = 0.36$ as opposed to $R^2 = 0.23$, being still both indicative of a weak relationship. Upon visual inspection, however, in the case of the non-zero intercept, it can be noted that the line almost completely misses the directions with high density of points. This misfit might be a result of the high number of scattered points, especially for values $< 130°$ and $> 280°$ in the ROSARIOSWAN data (x-axis), which are the likely cause for the very high MAE and RMSE, 58.79 and 102.02, as well as a SI of 42%.

It is notable that the line fit for the mean period cases, Figures 5.13c and 5.12c, is especially poor; $R^2 = -1.78$ and 0.1 for the forced-zero intercept and non-zero intercept case, respectively. The negative value of R^2 is telling of a poor fit due to the forced intercept, however, not forcing an intercept still results in a low goodness-of-fit, which can be easily seen from Figure 5.13c. Although less prominent than in the case of the Copernicus model vs the buoy data, Section 5.1.1, the V-like distribution of the data points for this parameter is still present and is difficult to model well using linear regression. The correlation, as reflected by $R = 0.31$, is weak, but the SI is the lowest from all the parameters at 16%, indicating that the variation of each point from the expected error is less than in the case of the the SWH. It can also be noted that the bias and MAE are, again, very close in value. What this implies is that, the difference between the two datasets has mostly the same sign, in this case positive. In this case that translates to the buoy data having systematically larger values than the ROSARIOSWAN Maria data; this can be indeed confirmed from Figure 5.11c, where the red lines (ROSARIOSWAN Maria) are shifted down from the black lined (buoy), as has been mentioned previously.

The line fit for the peak period cases, Figures 5.13d and 5.12d, is the worst from all cases. This can be visually noted in both scatter plots and from the values of R^2, which is negative for the forced-zero intercept case (-0.44) and 0.01 for the non-forced intercept case. In terms of the correlation, R gives a negative value, which is reflected in the negative slope in Figure 5.12d. The RMSE= 5.05, which is a relatively high value, and this can be explained by noting that the values of ROSARIOSWAN Maria values never exceed ~ 10 s, whereas those for the buoy go beyond 30 s, thus resulting in a high error for the higher values. This case has the highest value for SI, 45%, indicating that the bias is not a good representation of the differences found between the two datasets.

Plotting filtered data

Following the same reasoning behind the decision to filter out the data corresponding to SWH less than 1 m in Section 5.1.1, the ROSARIOSWAN Maria and Buoy data correlation, regression and measure calculations are carried out again here with a dataset excluding the 0-1 m wave height range; the resulting plots are given in Figure 5.14, where a non-zero intercept regression has been carried out. The below comparisons will hence be made with the non-zero intercept plots for the non-filtered case, Figure 5.13.

Apart from the case of the SWH, the filtering caused overall improved correlations in the wave parameters. In the case of the SWH, Figure 5.14a, all the measures but the SI are slightly worse, where, SI dropped from 40% to 21%; the measures now, however, indicate a weaker correlation and goodness-of-fit for the linear regression. In the case of the wave direction, Figure 5.14b, it can be clearly noted that the 'background' scattered values have been largely filtered out, with the exception of two horizontal distributions of points level with the clustered values. The value of R increased from 0.6 to

(A) *Significant Wave Height*

(B) *Wave Direction*

(C) *Mean Period*

(D) *Peak Period*
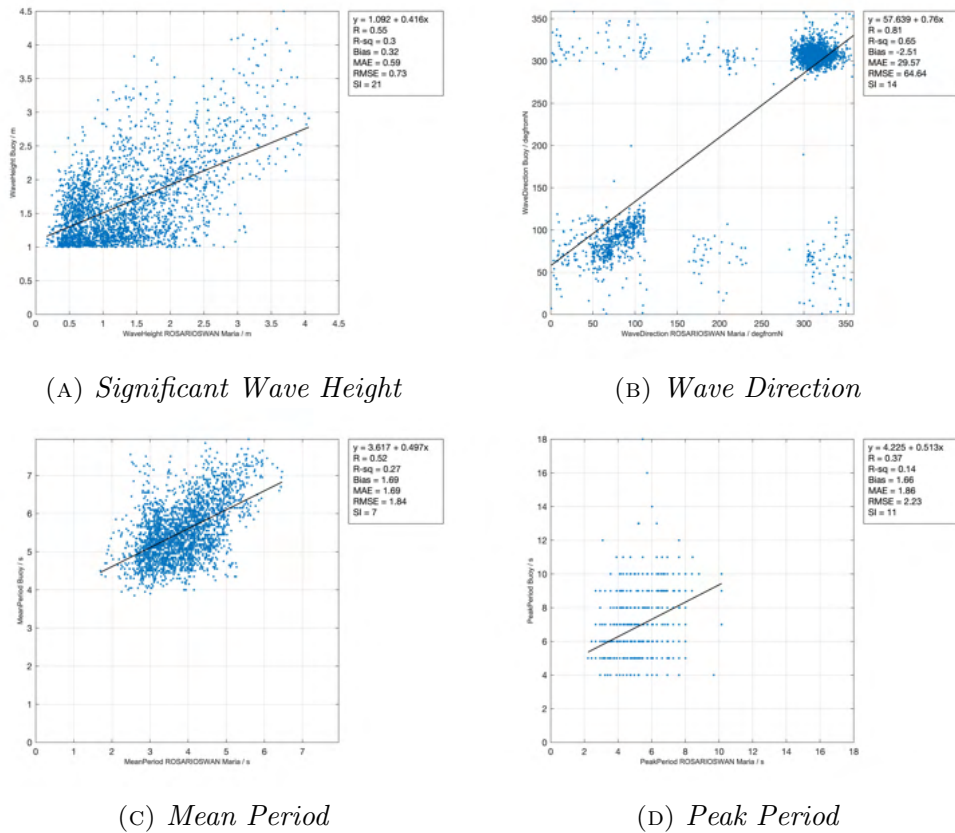
FIGURE 5.14: *Correlation plots between ROSARIOSWAN Maria model and Buoy; 0-1 m wave height range data points excluded*

0.81, and the fit better represents the data with an R^2 value of 0.65 (up from 0.36), indicating that the linear regression represents a moderate relationship. Additionally MAE, RMSE and SI all improved with values decreased by approximately 50%, 37% and 67% respectively. The resulting bias in this case actually increased to -2.51, taking it further away from zero. For the case of the mean period, the V-shaped distribution has been removed and a slightly more linear plot is obtained. Indeed, the linear fit performs better with and increase in R^2 from 0.1 to 0.27, however still indicating that the linear regression represents a very weak relationship. The correlation measure R also improved from a value of 0.31 to 0.52. Additionally MAE, RMSE and SI all improved with values decreased by approximately 18%, 19% and 56%, respectively. The resulting bias is only slightly lower at 1.84.

Overall, the improvement resulting from filtering was not very extensive in this case, where the correlation is still relatively weak.

In the peak period plot, Figure 5.14d, it can also be noted that much of the points associated with the higher peak period values from the buoy dataset have been filtered out, resulting in a less scattered plot. The correlation between the datasets improved, R increased from -0.11 to 0.37, suggesting a weak relationship. As a result, the linear fit also performed better with R^2 going up to 0.14 from 0.01, however this is, again, still indicative of an ill-fit. Values of MAE, RMSE and SI all improved with values decreased by approximately 43%, 56% and 76%, respectively. The resulting bias is also slightly closer to zero at 1.77. The measure calculations are then most improved in this case, with higher percentage decreases than those in the other parameters.

SWH Threshold Analysis

The probability of the ROSARIOSWAN Maria model being able to detect SWHs above a given threshold is plotted against the probability of it being a false alarm, using the method described in Section 3.2.4, where the model is compared to the buoy data. The resulting plot is given in Figure 5.15, where thresholds are taken from $H_s = 0.5$ to 5 in steps of 0.5.

From this plot, it can be observed that the ROSARIOSWAN Maria model has a relatively good PD of sea states when the threshold of H_s is at 0.5 m, with a value of about $\sim 62\%$, with an associated PFA of $\sim 8\%$. Unlike the case of the Copernicus model in Section 5.1.1, the power PD starts degrading immediately with increasing threshold value; there is a generally downwards trend apart from a 'bump' between the thresholds 1.5 and 3 m. In addition, with increase in the threshold there is also an increase in the PFA where,
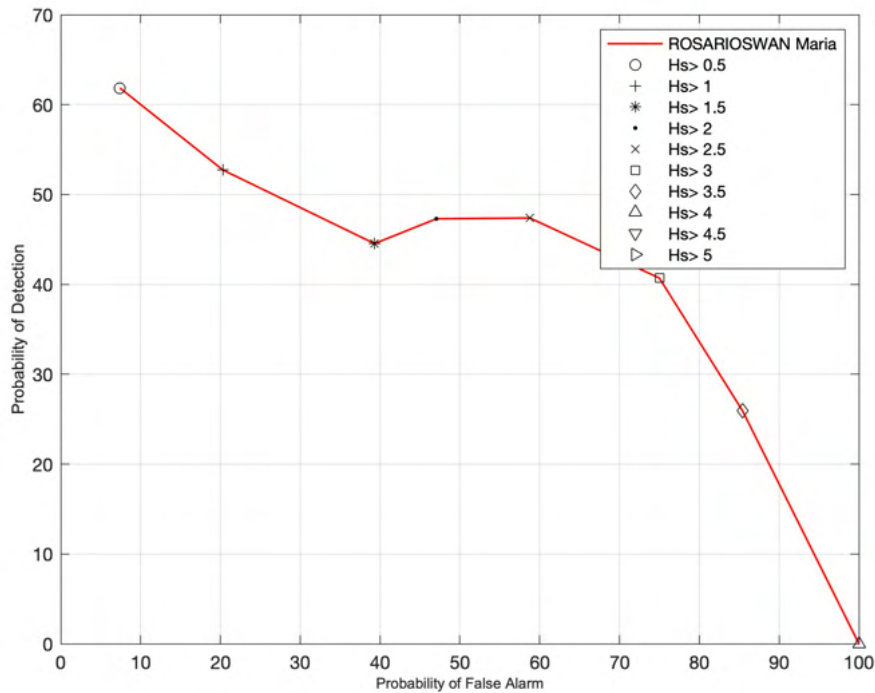
FIGURE 5.15: *ROSARIOSWAN Maria model Data SWH Threshold Analysis; tested against buoy data*

from $H_s > 0.5$ to $H_s > 3.5$, this probability goes up from $\sim 8\%$ to $\sim 85\%$ and the PD decreases from $\sim 62\%$ to $\sim 26\%$. For the case of $H_s > 4$, the value of PD falls to 0% with an associated PFA of 100%; in this case, it is likely a very limited number of points exist that satisfy this threshold, thus the extreme values.

5.1.3   Buoy vs ROSARIOSWAN Skiron Model

Using the ROSARIOSWAN Skiron model time series data from the grid point as described in Section 4.3, and as illustrated in Figure 4.6, a temporal comparison between the buoy data and ROSARIOSWAN Skiron model can be made. The data being compared here is the SWH, wave direction, mean period and peak period; the time series of these are overlaid for visual inspection in Figure 5.16. In addition, the probability density of each of the parameters from both datasets were overlaid for ease of comparison; the resulting distributions are given in Figure 5.17.

Given that ROSARIOSWAN Skiron uses the same model as the ROSARIOSWAN Maria with a different wind forcing model, the results for the Skiron forced model turn out to be quite comparable to those of the Maria forced model. In light of this, the discussion is not here repeated, but the regression plots are presented in Figures 5.19 and 5.18. The values for the resulting parameters are summarised in Tables for convenience in Section 5.1.4.

<div align="center">

Plotting filtered data

</div>

Again, the data is filtered based on SWH values such that the ROSARIOSWAN Skiron and Buoy data correlation, regression and measure calculations are carried out again here with a dataset excluding the 0-1 m wave height range; the resulting plots are given in Figure 5.20, where a non-zero intercept regression has been carried out.
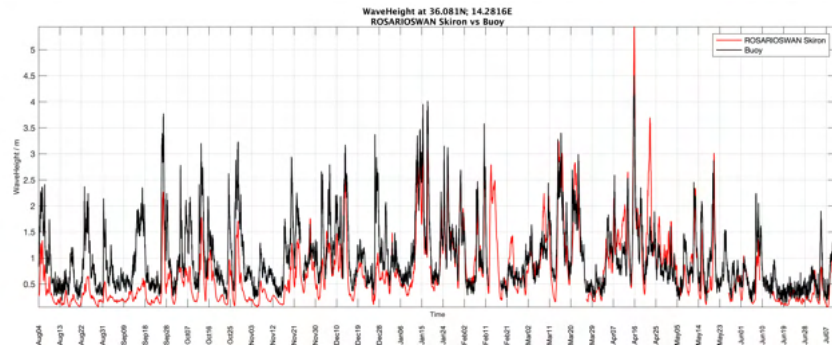
(A) *Significant Wave Height*
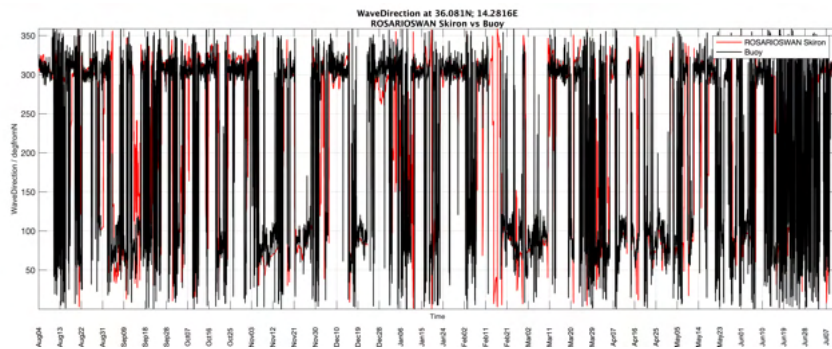
(B) *Wave Direction*
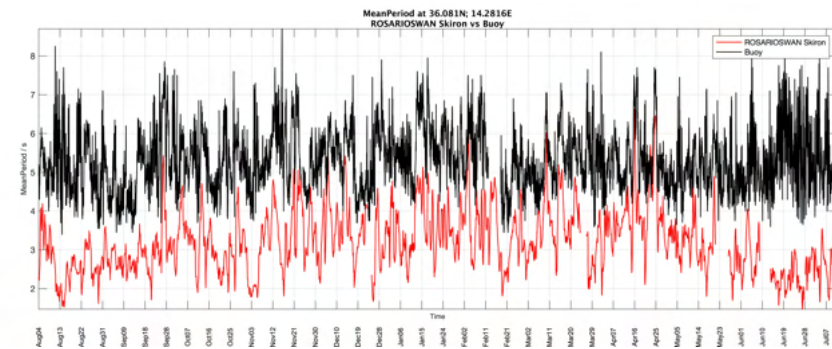
(C) *Mean Period*
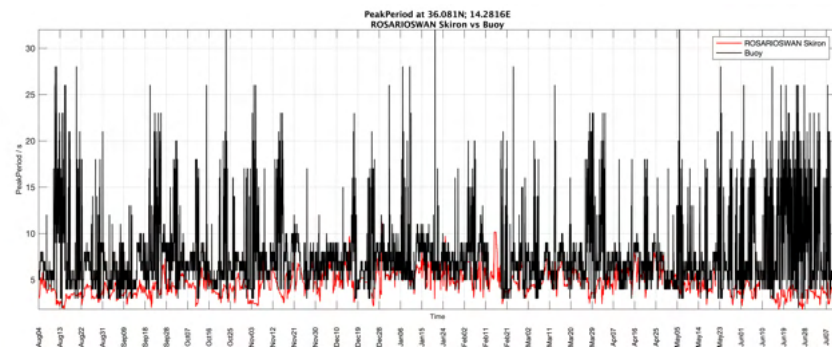
(D) *Peak Period*

FIGURE 5.16: *ROSARIOSWAN Skiron model (red) and Buoy (black) time series data from August 4th 2020 to July 12th 2021*

(A) *Significant Wave Height*

(B) *Wave Direction*

(C) *Mean Period*

(D) *Peak Period*
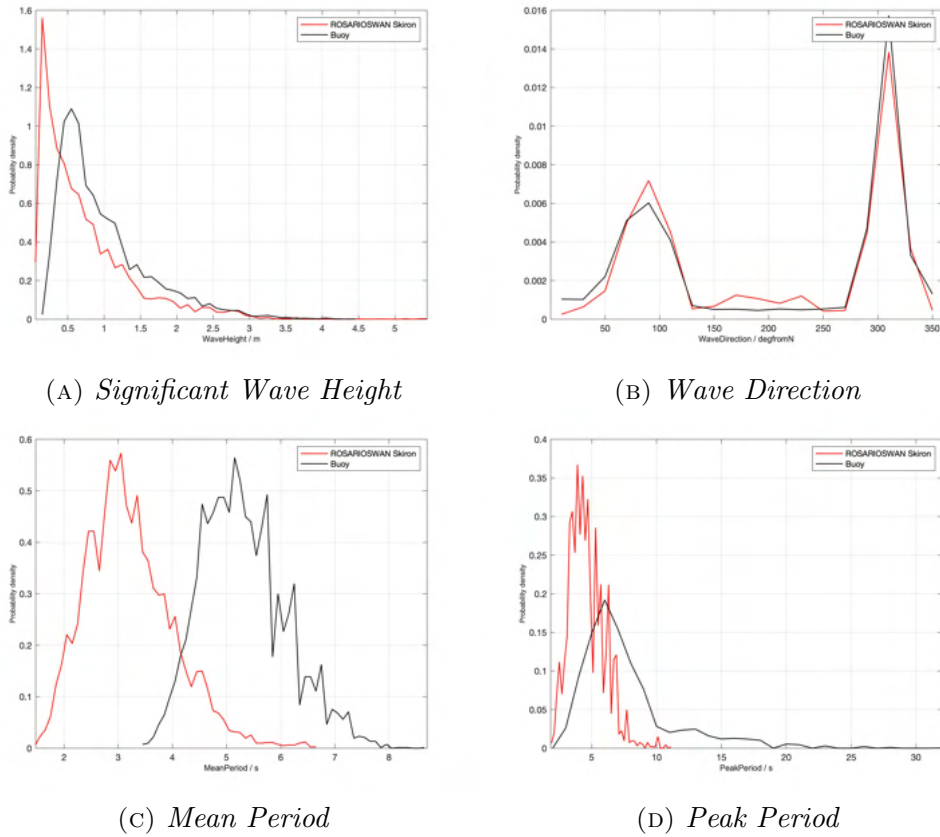
FIGURE 5.17: *Probability Density of ROSARIOSWAN Skiron model (red) and Buoy (black) data*

SWH Threshold Analysis

The probability of the ROSARIOSWAN Skiron model being able to detect SWHs above a given threshold is plotted against the probability of it being a false alarm, using the method described in Section 3.2.4, where the model is compared to the buoy data. The resulting plot is given in Figure 5.21, where thresholds are taken from $H_s = 0.5$ to 5 in steps of 0.5.

From this plot, it can be observed that the ROSARIOSWAN Skiron model has a relatively good PD of sea states when the threshold of H_s is at 0.5 m, with a value of about $\sim 62\%$. Like in the case for the ROSARIOSWAN Maria model in Section 5.1.2, the PD starts degrading immediately with

(A) *Significant Wave Height*

(B) *Wave Direction*

(C) *Mean Period*

(D) *Peak Period*
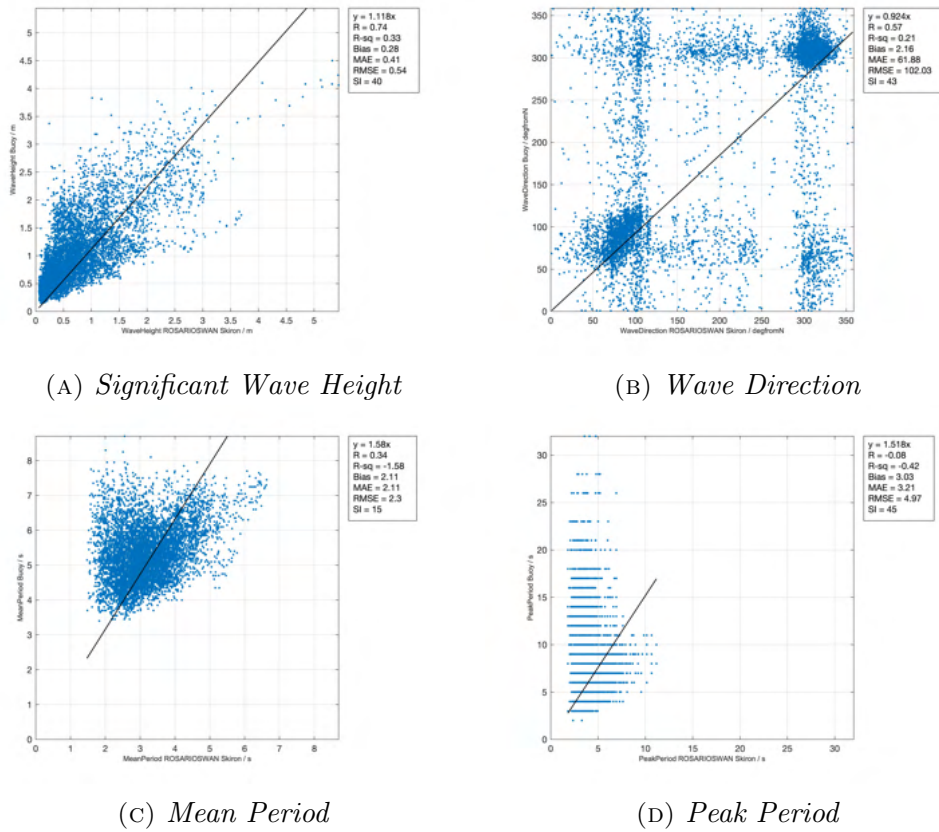
FIGURE 5.18: *Correlation plots between ROSARIOSWAN Skiron model and Buoy; forced zero-intercept regression*

increasing threshold value, with a general downwards trend up to $H_s > 2.5$. In addition, with increase in the threshold there is also an increase in the PFA where, from $H_s > 0.5$ to $H_s > 2.5$, this probability goes up from $\sim 8\%$ to $\sim 54\%$, and the associated PD decreases from $\sim 62\%$ to $\sim 34\%$. For the case of $H_s > 3$ and $H_s > 3.5$, the PFA goes down to $\sim 50\%$ again, and the associated PD values are $\sim 28\%$ and $\sim 41\%$, respectively. For the case of $H_s > 4$, the value of PD actually increases up to $\sim 98\%$ and the PFA falls to $\sim 44\%$. In this case it is again likely that a very limited number of points exist that satisfy this threshold, thus resulting in extreme values.

(A) *Significant Wave Height*

(B) *Wave Direction*

(C) *Mean Period*

(D) *Peak Period*
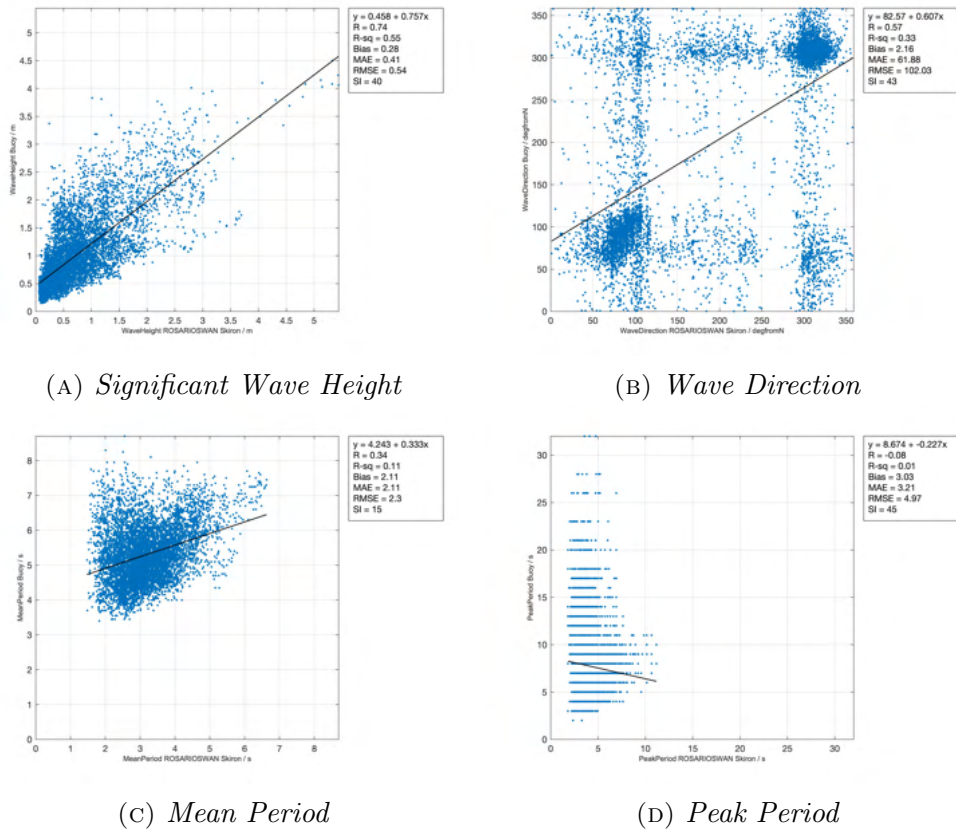
FIGURE 5.19: *Correlation plots between ROSARIOSWAN Skiron model and Buoy; non-zero-intercept regression*

(A) *Significant Wave Height*

(B) *Wave Direction*

(C) *Mean Period*

(D) *Peak Period*
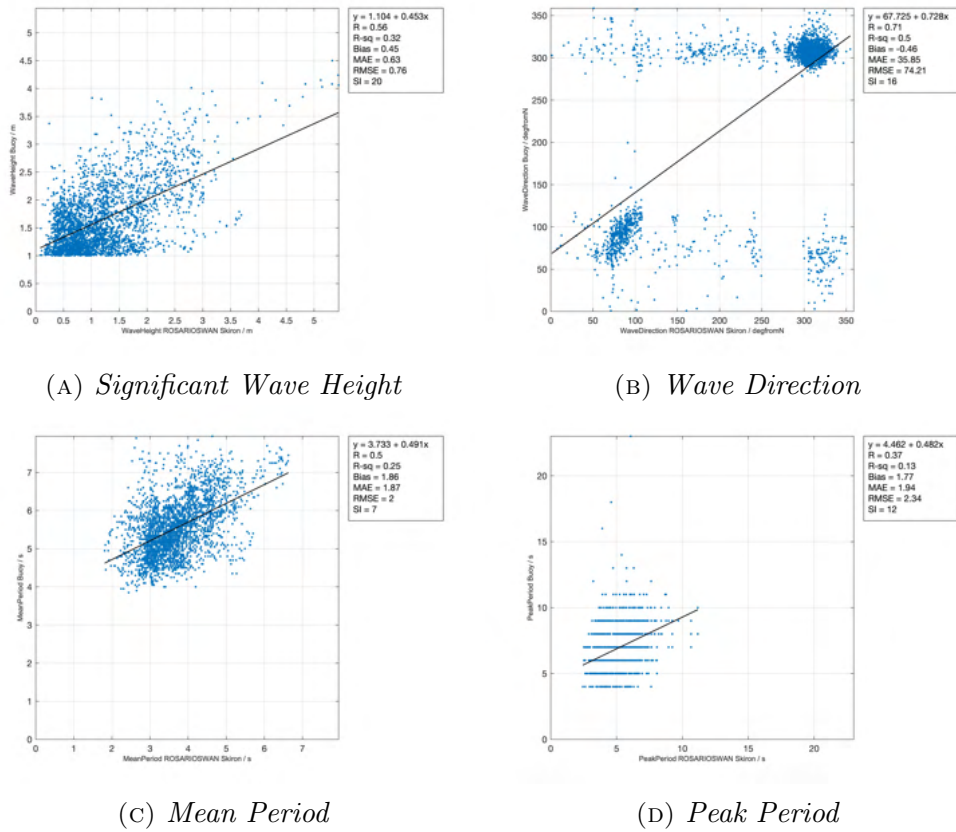
FIGURE 5.20: *Correlation plots between ROSARIOSWAN Skiron model and Buoy; 0-1 m wave height range data points excluded*
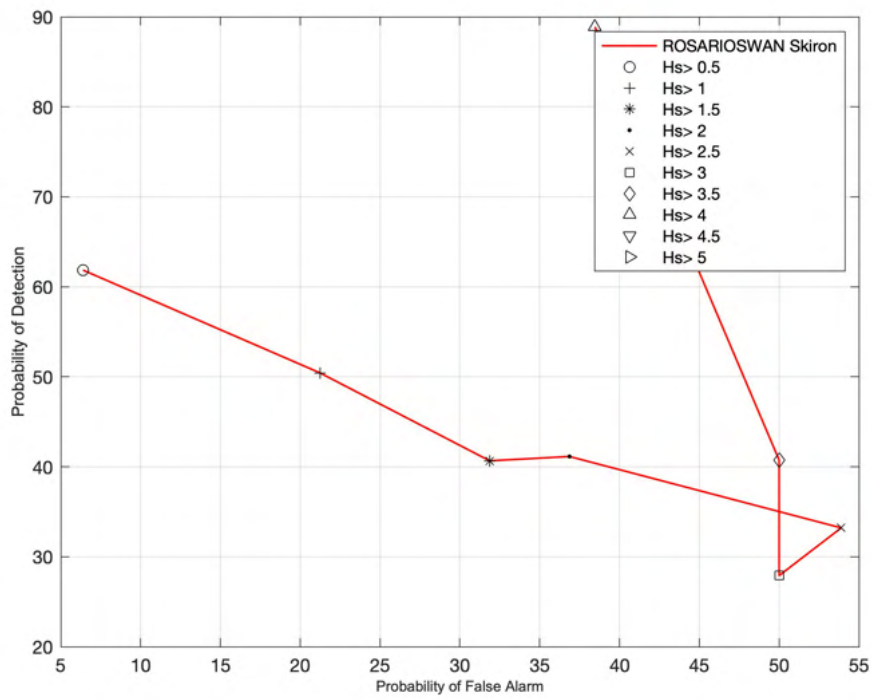
FIGURE 5.21: *ROSARIOSWAN Skiron model Data SWH Threshold Analysis; tested against buoy data*

5.1.4 Summary

In this Section, the R value, bias, MAE, RMSE and SI for the comparisons mentioned above are summarised in Tables for the SWH, wave direction, mean period and peak period in Tables 5.1-5.4, respectively, for both the full datasets and the SWH-filtered datasets.

TABLE 5.1: *SWH parameters from buoy and model data comparison for the period 04/08/2020 - 12/07/2021*

Original data set	R	Bias	MAE	RMSE	SI
Copernicus	0.94	-0.01	0.18	0.26	23
ROSARIOSWAN Maria	0.75	0.22	0.39	0.52	40
ROSARIOSWAN Skiron	0.74	0.28	0.41	0.54	40
Filtered data set					
Copernicus	0.88	-0.08	0.27	0.37	12
ROSARIOSWAN Maria	0.55	0.32	0.59	0.73	21
ROSARIOSWAN Skiron	0.56	0.45	0.63	0.76	20

TABLE 5.2: *Wave Direction parameters from buoy and model data comparison for the period 04/08/2020 - 12/07/2021*

Original data set	R	Bias	MAE	RMSE	SI
Copernicus	0.63	-9.78	52.46	96.27	41
ROSARIOSWAN Maria	0.60	0.74	58.79	102.02	42
ROSARIOSWAN Skiron	0.57	2.16	61.88	102.03	43
Filtered data set					
Copernicus	0.80	-1.76	23.36	60.75	13
ROSARIOSWAN Maria	0.81	-2.51	29.57	64.64	14
ROSARIOSWAN Skiron	0.71	-0.46	35.85	74.21	16

In light of the preceding discussions and comparisons of the buoy measurement data with model data from Copernicus, ROSARIOSWAN Maria and Skiron, and by comparing the Tables 5.1-5.4, it can be noted that the buoy measurements tend to have a stronger correlation with the Copernicus model rather than either of the ROSARIOSWAN models. This is exemplified by higher values of R and lower values of bias, MAE and RMSE. The two

TABLE 5.3: *Mean Period parameters from buoy and model data comparison for the period 04/08/2020 - 12/07/2021*

Original data set	R	Bias	MAE	RMSE	SI
Copernicus	0.41	1.49	1.51	1.82	18
ROSARIOSWAN Maria	0.31	2.05	2.06	2.27	16
ROSARIOSWAN Skiron	0.34	2.11	2.11	2.30	15
Filtered data set					
Copernicus	0.81	0.83	0.86	0.99	5
ROSARIOSWAN Maria	0.52	1.69	1.69	1.84	7
ROSARIOSWAN Skiron	0.50	1.86	1.87	2.00	7

TABLE 5.4: *Peak Period parameters from buoy and model data comparison for the period 04/08/2020 - 12/07/2021*

Original data set	R	Bias	MAE	RMSE	SI
Copernicus	-0.02	1.46	2.39	4.34	48
ROSARIOSWAN Maria	-0.11	3.09	3.28	5.05	45
ROSARIOSWAN Skiron	-0.08	3.03	3.21	4.97	45
Filtered data set					
Copernicus	0.66	-0.05	0.84	1.23	10
ROSARIOSWAN Maria	0.37	1.66	1.86	2.23	11
ROSARIOSWAN Skiron	0.37	1.77	1.94	2.34	12

ROSARIOSWAN models, Maria and Skiron, are for the most part comparable in their correlation with the buoy measurements, thus having similar parameters in Tables 5.1-5.4.

5.2 Data Comparison: Radar vs Models

In this Section, the relationship between the SOPU HF radar measurement dataset and the numerical models under consideration are investigated. In this case, unlike that for the comparisons between the buoy and model data (Section 5.1), no filtering will be considered due to the limited amount of data available; see Section 4.2.2.

5.2.1 Radar vs Copernicus Model

In order to find the Copernicus model grid points that intersect with the SOPU radar's second annular ring, which is 5.85 km away from the station (a radius of about 0.0527°), a ring segment extending from shore to shore is considered. The ring is made of two concentric circles of radii 0.0580° and 0.0474°, see Figure 5.22. From this Figure it can be seen that two points fall in this region from which data corresponding to each Radar data point available could be extracted. Given that there are 339 radar data points, see Section 4.2.2, a total of 678 data points can be compared.

Correlation and other error metrics were computed for these datasets as described in Sections 3.2.1 and 3.2.2. Scatter plots between each parameter of the dataseries were plotted and linear regression was performed. The parameters considered in this case were the SWH, Direction and mean period. The resulting plots are given in Figures 5.23 and 5.24 for the forced-zero intercept and non-zero intercept regressions, respectively.

The best linear fit from the three parameters is given by that of the wave direction, although this is not immediately evident from visual inspection of Figures 5.23b and 5.24b; the R^2 values are 0.28 and 0.32, for the forced-zero intercept and non-zero intercept case, respectively. The model fit is then only
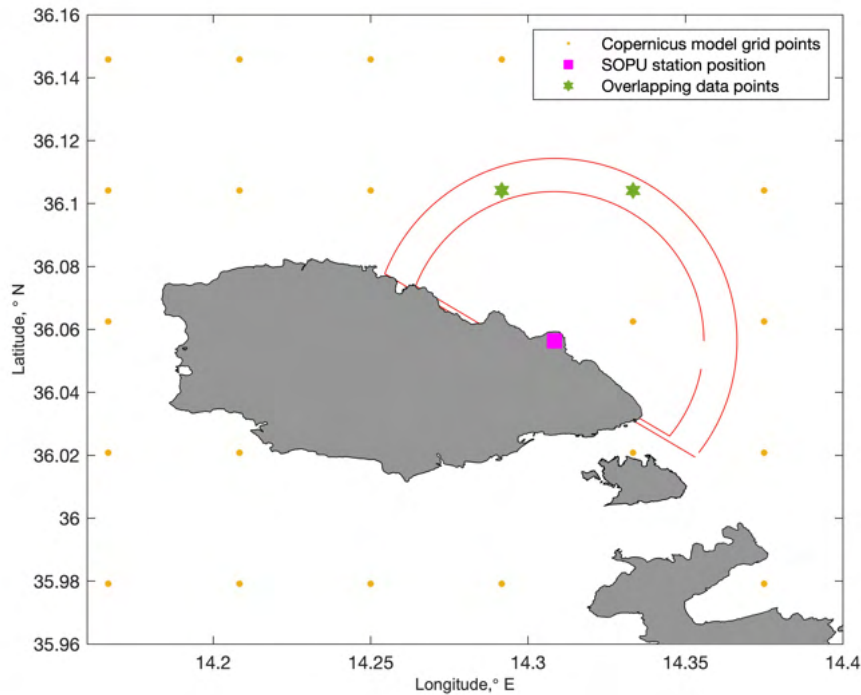
FIGURE 5.22: *Copernicus model grid points overlapping the SOPU radar measurement area*

slightly better in the case where there is no forced intercept. It is telling from this data comparison, where the best linear fit from all the parameters is very weak for either case, that more data would be ideal for comparison. Further analysing the Direction data comparison, the correlation between the two datasets is not as weak, as indicated by the value of R, 0.57, which indicates a moderate correlation. The bias, -26.97, and the MAE, 71.55 as well as the RMSE, 118.19, are not insignificant. It is likely that these errors are introduced through the clustering of points at the top left and bottom right areas of the plot, similar to the case of comparison of the Buoy and Copernicus model data in Section 5.1.1. The SI is not too high a value at 17%.

For the case of SWH, Figures 5.23a and 5.24a, the correlation between the two datasets is quite weak, with $R = 0.21$. The linear fit in this case performs

(A) *Significant Wave Height*

(B) *Wave Direction*

(C) *Mean Period*
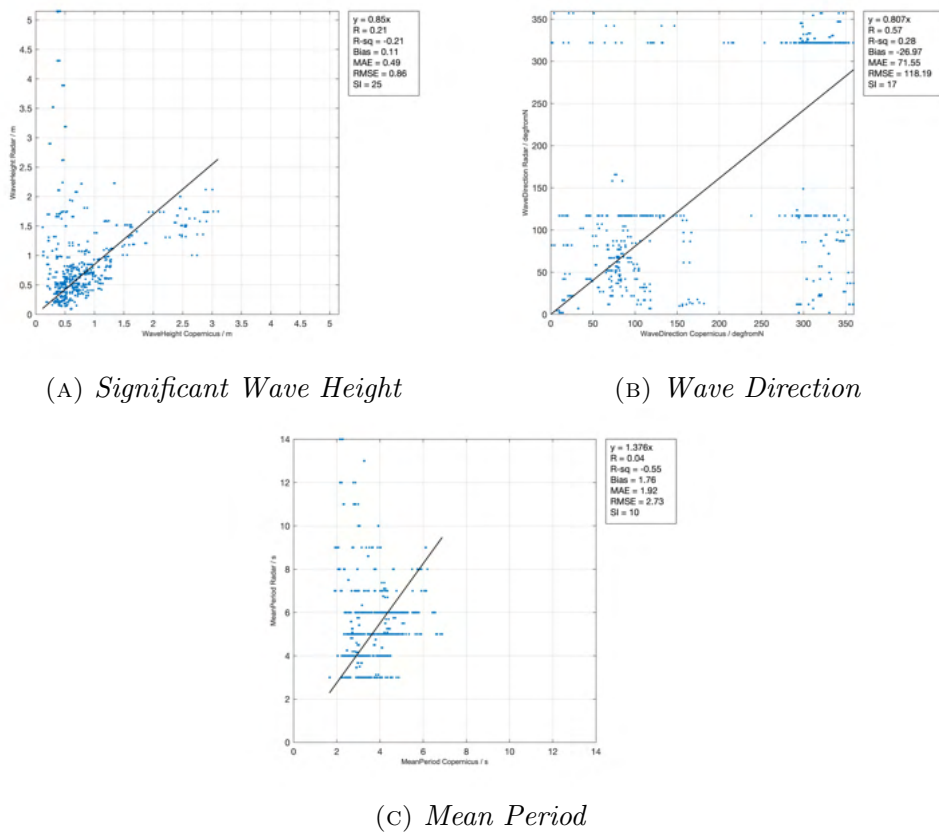
FIGURE 5.23: *Correlation plots between Copernicus model and Radar; forced-zero intercept regression*

terribly for both the forced-zero and the non-zero intercept case, with $R^2 = -0.21$ and $R^2 = 0.05$, both indicative of an ill-fitting model. Upon visual inspection it can be noted that, at lower values of the Copernicus model, there are high values from the Radar measurements; in particular, between wave heights of 0 and 0.5 m for the Copernicus model, there are radar measurements of the SWHs ranging between 0 and 5.5 m. This feature of the plot could then be a possible reason for the misfit of the linear regression. The values of MAE and RMSE, 0.49 and 0.86, are not insignificant due to the order of the wave heights. The bias and SI are not too high in this case at 0.11 and 25%, respectively.

It can be noted that the line fit for the mean period cases, Figures 5.23c

(A) *Significant Wave Height*

(B) *Wave Direction*

(C) *Mean Period*
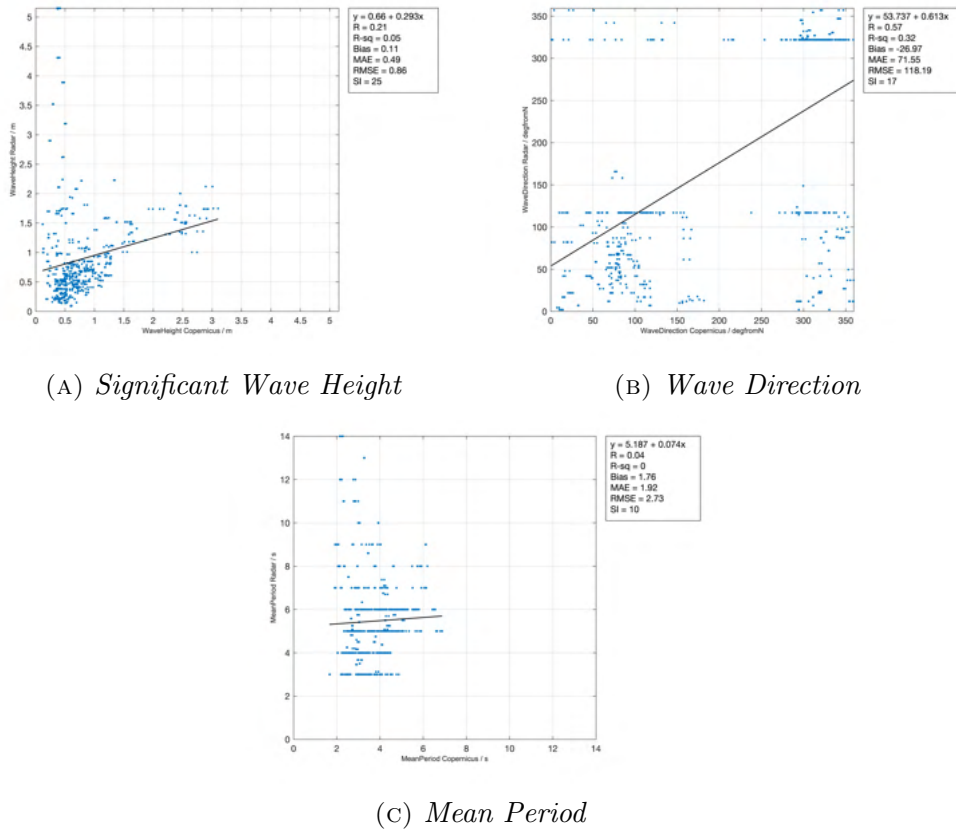
FIGURE 5.24: *Correlation plots between Copernicus model and Radar; non-zero intercept regression*

and 5.24c, is the worst from all cases. This can be visually noted in both scatter plots and from the values of R^2, which is negative for the forced-zero intercept case (-0.55) and 0 for the non-forced intercept case. In terms of the correlation, $R = 0.04$, which is very close to zero, indicating that there exists almost no correlation. The bias, MAE and RMSE, have values of 1.76, 1.92 and 2.73, which are relatively high; this could possibly be explained by noting that the values of Copernicus never exceed 8 s, whereas those for the radar go up to about 14 s, thus resulting in a high error for the higher values. This case has the lowest value for SI, 10%.

113

5.2.2   Radar vs ROSARIOSWAN Model

In the case of the comparison between radar data and the ROSARIOSWAN model (Maria and Skiron) data, the model point closest to the buoy position was considered, see Section 4.3. This was considered since the radar annular ring in use, the second, is the closest to the buoy position and is what is used for comparison with such *in-situ* data. From the 339 radar data points, only 150 and 30 data points overlapped with the model for the Maria and Skiron variations, respectively, since some missing data exists in these model datasets as well. This portion makes up about 44% and 9% of the radar dataset for the Maria and Skiron models, respectively, which is already a very small set compared to the time range over which this data was collected, see Section 4.2.2.

Correlation and other error metrics were computed for these datasets for the parameters of SWH, Direction and mean period. The limited number overlapping points, over an almost two-year period, mean that the correlation analysis and regression did not yield very useful results, and are thus not plotted here; the resulting correlation and regression measures are however presented in Tables 5.5 and 5.6, respectively, where both versions of the ROSARIOSWAN model are included.

As can be seen from these Tables, the limited data affects negatively the capability of comparing the two datasets well. In terms of correlation, the only moderate correlation is that for the Maria model's wave direction parameter, $R = 0.47$, where the associated non-zero intercept linear fit has the highest R^2 at 0.22; this value is quite a low one. The bias for this same value is, unexpectedly, relatively low at -8.43. The second best non-zero intercept linear fit is the case of the mean period parameter for the Skiron model, where $R^2 = 0.17$. In this case, however, both the R value and the

TABLE 5.5: *Wave parameters' resulting correlation measures from SOPU radar and ROSARIOSWAN model data comparison for the period 04/08/2020 - 12/07/2021*

Wave Parameter	R	Bias	MAE	RMSE	SI
Maria					
SWH	0.16	0.37	0.61	1.02	12
Mean Period	−0.15	2.87	2.92	3.77	5
Direction	0.47	−8.43	77.77	124.45	9
Skiron					
SWH	0.16	0.48	0.71	0.99	5
Mean Period	−0.41	3.1	3.52	4.33	3
Direction	0.08	−73.77	128.18	170.24	6

TABLE 5.6: *Wave parameters' resulting linear regressions (non-zero and forced-zero intercept) from SOPU radar and ROSARIOSWAN data comparison for the period 04/08/2020 - 12/07/2021*

Wave Parameter	$y = mx + c$	R^2	$y = mx$	R^2
Maria				
SWH	$0.828 + 0.218x$	0.03	$0.883x$	−0.49
Mean Period	$7.251 - 0.356x$	0.02	$1.72x$	−0.83
Direction	$84.478 + 0.489x$	0.22	$0.816x$	0.08
Skiron				
SWH	$0.921 + 0.177x$	0.03	$0.884x$	−1
Mean Period	$9.127 - 0.881x$	0.17	$1.658x$	−1.41
Direction	$123.174 + 0.085x$	0.01	$0.54x$	−0.22

sign of the gradient in the equation indicate a negative correlation. This is very undesirable since, in the ideal case, the resulting correlations are positive and equal to one. For all the other parameters, the linear fits are ill-fitting, more so for the forced-zero intercept (as is expected), and the values of R, bias, MAE and RMSE further support this. The SI are quite low, but this is likely the case because of the limited amount of points available for comparison.

5.3 Data Comparison: Models vs Models

In this Section, model data comparison is made between the Copernicus model, see Section 4.1.1, and the ROSARIOSWAN model's two variations, Maria and Skiron, see Section 4.1.2. The comparisons will be made at the grid points of the models closest to the buoy position as described in Section 4.3.

5.3.1 ROSARIOSWAN Maria vs Skiron

Here, a comparison between the ROSARIOSWAN Maria and Skiron configurations is made. Differing in their wind forcing source data, and not in the model itself, it is useful to see how these two datasets differ from one-another. First, the time series of these are overlaid for visual inspection in Figure 5.25. In addition, the probability density of each of the parameters from both datasets were overlaid for ease of comparison; the resulting distributions are given in Figure 5.26.

From these Figures, it is already clear that both model versions show a strong correlation. Some further things can be said about each parameter from the probability density plots in Figure 5.26, even though, overall, these show very good matches. For the case of the SWH, it can be noted that the Skiron model tends to produce a slightly higher probability density at the distributions peak, despite it being the same peak. This can also be said for the case of the wave direction, where this is the case for values of direction in the, approximate, range 70-270°. The opposite is the case, Maria model has higher probability densities, for values $< 70°$ and $> 325°$. For the remaining range, $270 - 325°$, the models have a very similar probability density. Not much can be said for the case of the mean period, as the probability densities
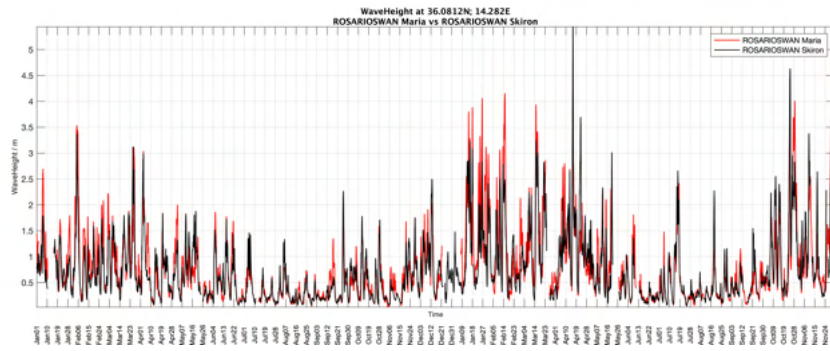
(A) *Significant Wave Height*
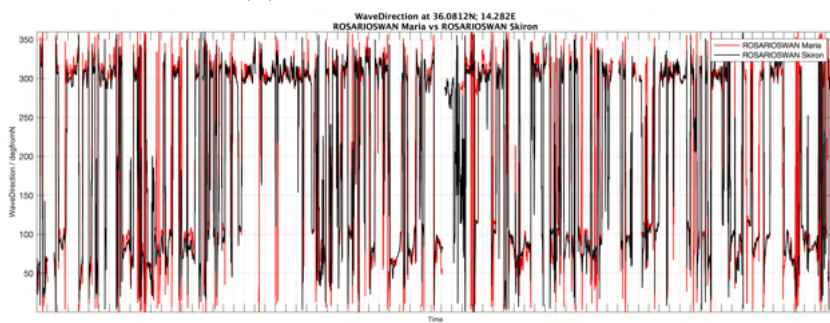
(B) *Wave Direction*
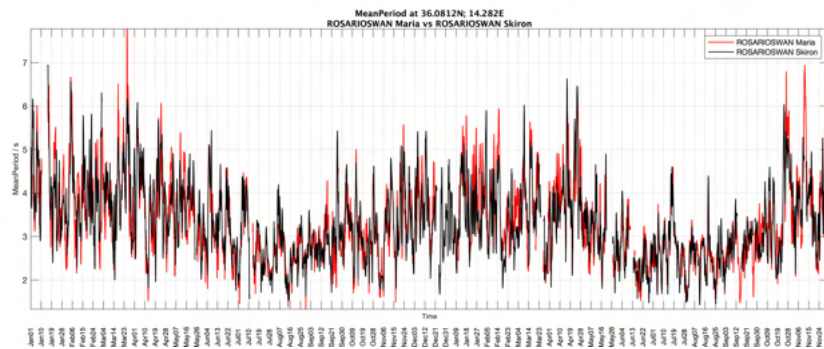
(C) *Mean Period*
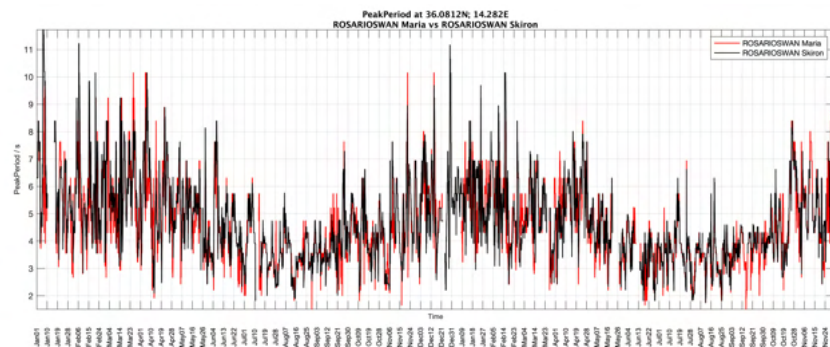
(D) *Peak Period*

FIGURE 5.25: *ROSARIOSWAN Skiron (black) and ROSARIOSWAN Maria (red) models' time series data from January 2020 to November 2021*

117

(A) *Significant Wave Height*

(B) *Wave Direction*

(C) *Mean Period*
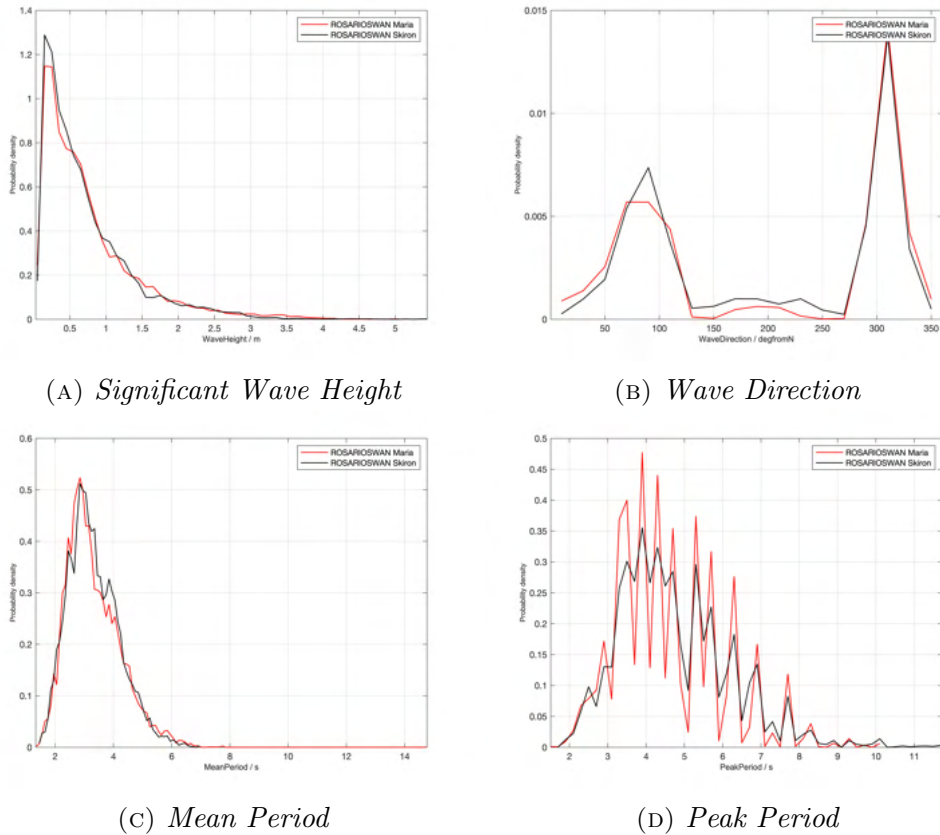
(D) *Peak Period*

Figure 5.26: *Probability Density of ROSARIOSWAN Maria (red) and ROSARIOSWAN Skiron (black) model data*

overlap quite well in this case. For the case of the peak period, in general, the probability densities match in the position of peaks and troughs in the distribution. However, for the case of the Maria model, peaks are generally higher and troughs lower than those resulting from the Skiron model.

Correlation and other error metrics were computed for these datasets, the resulting plots are given in Figures 5.27 and 5.28 for the forced-zero intercept and non-zero intercept regressions, respectively.

From these plots, it can be seen that all the wave parameters show a strong correlation between the datasets, as is expected. In all cases but the Wave direction, the data points spread further out away from the origin of the plots, indicating larger differences between higher values. For the case of the

(A) *Significant Wave Height*

(B) *Wave Direction*

(C) *Mean Period*

(D) *Peak Period*
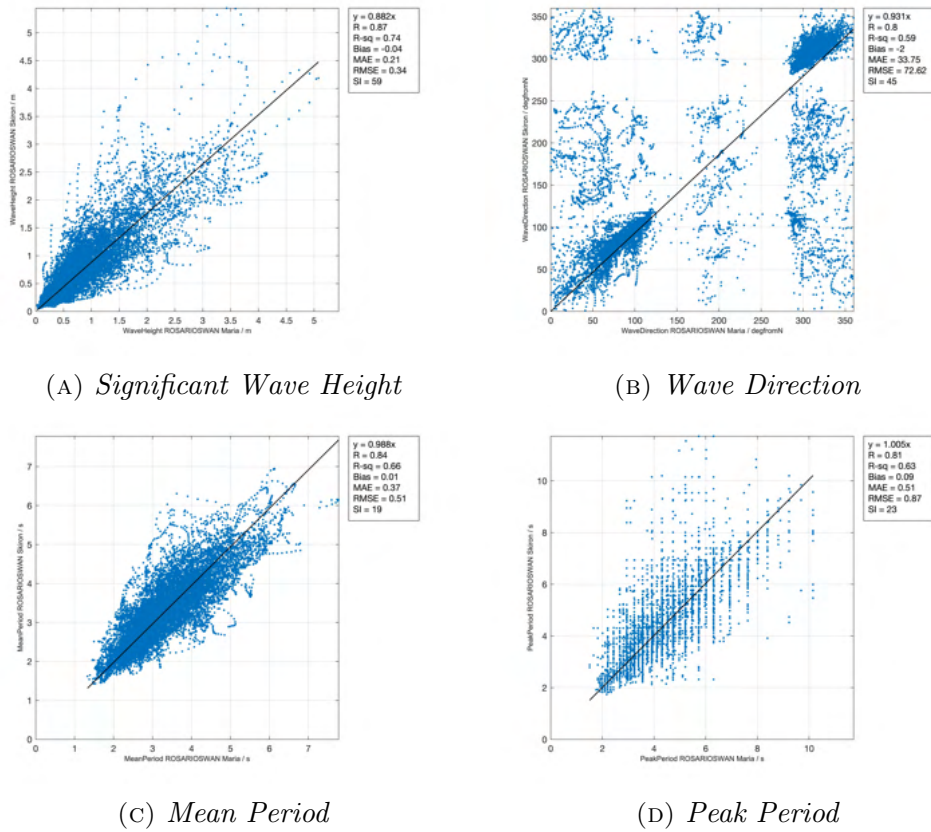
FIGURE 5.27: *Correlation plots between ROSARIOSWAN Maria and ROSARIOSWAN Skiron models; forced-zero intercept regression*

wave direction, a concentration of points can again be seen in two directions, see Figures 5.27b and 5.28b, which are roughly Easterly and North-Westerly. In this plot it can be noted that there is 'background' scattered points which do not show a correlation.

Since all of the plots show a relatively good correlation and linear fit, the parameters have been summarised in Tables 5.7 and 5.8 for ease of analysis.

As one case see from Table 5.7, all of the R values in this case are ≥ 0.80, which is indicative of the aforementioned strong correlation. In addition to this, the biases are all < 0.1, apart from the direction case, therefore, are quite close to zero. In the direction case the bias is -2; this is likely a result of the 'background' scatter mentioned above. The MAE and RMSE are not

119

(A) *Significant Wave Height*

(B) *Wave Direction*

(C) *Mean Period*

(D) *Peak Period*
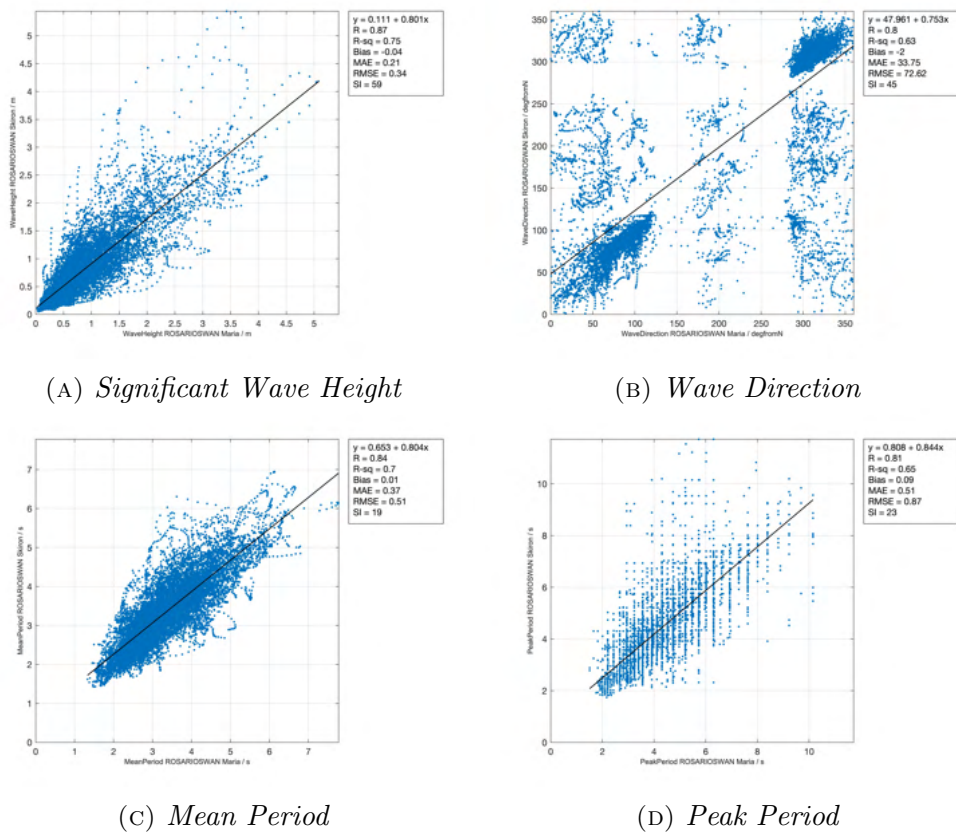
FIGURE 5.28: *Correlation plots between ROSARIOSWAN Maria and ROSARIOSWAN Skiron models; non-zero intercept regression*

insignificant for all cases, and this can be attributed to the spread of the points, which can be seen in the scatter plots. Indeed, as a reflection of this, the SI is the highest for the SWH case (59%) and lowest for the mean period case (23%).

Further indication of the strong correlation between the datasets are the R^2 values for the forced-zero and non-zero intercept regressions, see Table 5.8. What can be noted here is that the R^2 values for the non-zero intercept linear fits are very close to the forced-zero intercept cases. This indicates that a linear relationship of the form $y = mx$, with $0.882 \leq m \leq 1.005$ in these cases (which are relatively close to 1), is not too far off from the best linear fit.

Table 5.7: *Wave parameters' resulting correlation measures from ROSARIOSWAN Maria and ROSARIOSWAN Skiron model data comparison for the period January 2020 - November 2021*

Wave Parameter	R	Bias	MAE	RMSE	SI
SWH	0.87	-0.04	0.21	0.34	59
Direction	0.8	-2	33.75	72.62	45
Mean Period	0.84	0.01	0.37	0.51	19
Peak Period	0.81	0.09	0.51	0.87	23

Table 5.8: *Wave parameters' resulting linear regressions (non-zero and forced-zero intercept) from ROSARIOSWAN Maria and ROSARIOSWAN Skiron model data comparison for the period January 2020 - November 2021*

Wave Parameter	$y = mx + c$	R^2	$y = mx$	R^2
SWH	$0.111 + 0.801x$	0.75	$0.882x$	0.74
Direction	$47.961 + 0.753x$	0.63	$0.931x$	0.59
Mean Period	$0.653 + 0.804x$	0.7	$0.988x$	0.66
Peak Period	$0.808 + 0.844x$	0.65	$1.005x$	0.63

5.3.2 Copernicus model vs ROSARIOSWAN

In this Section, the Copernicus Model will be compared to the ROSARIOSWAN model; the time-series plot for the Copernicus model and the Maria and Skiron models have been plotted in Figures 5.29 and 5.33 respectively for the period January 2020 - November 2021; as analysed and discussed in Section 5.3.1, there is quite a good correlation between the Maria and Skiron versions of the ROSARIOSWAN Models. Because of this, the comparison of the ROSARIOSWAN models with the Copernicus model will not be done separately for the two versions since the resulting correlation measures and regressions are very similar. This can be seen from the scatter plots for the Maria and Skiron models in Figures 5.30 and 5.31, and 5.34 and 5.35, respectively, as well as from the probability density plots in Figures 5.32 and 5.36 for Maria and Skiron, respectively. The resulting parameters have been summarised in Tables 5.9 and 5.10 for ease of comparison.
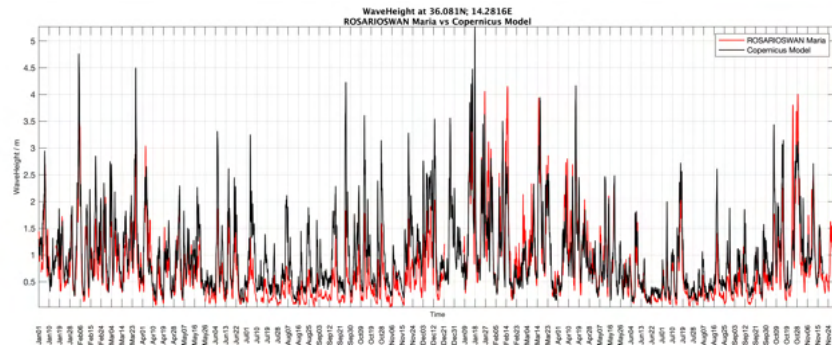
(A) *Significant Wave Height*
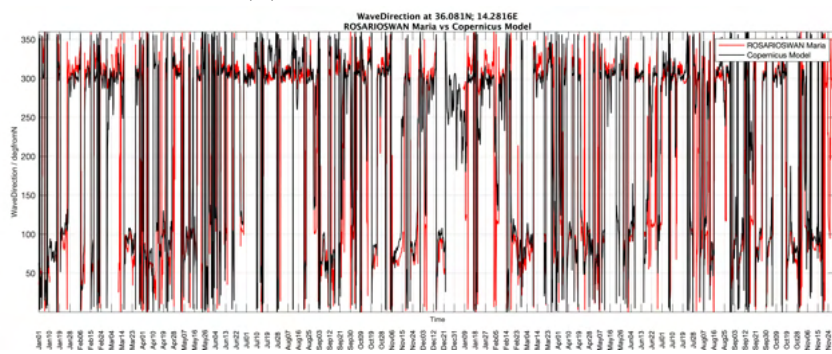
(B) *Wave Direction*
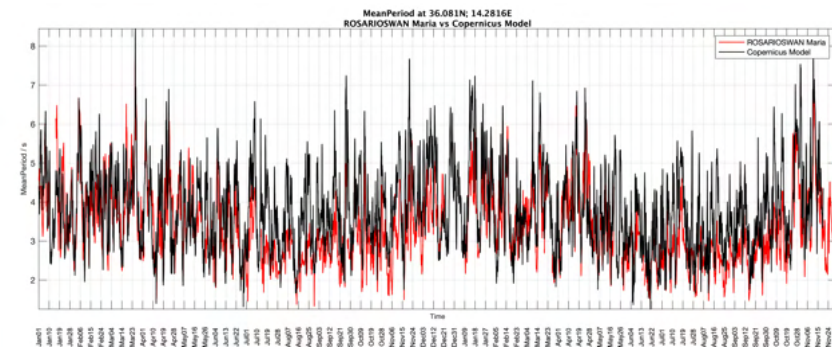
(C) *Mean Period*
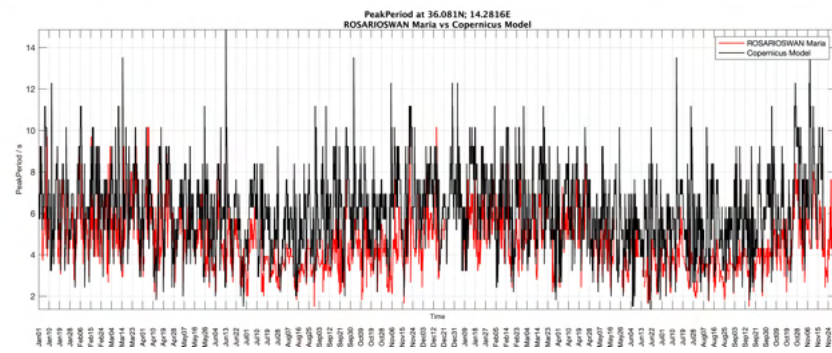
(D) *Peak Period*

FIGURE 5.29: *ROSARIOSWAN Maria model (red) and Copernicus model data (black) from January 2020 to November 2021*

(A) *Significant Wave Height*

(B) *Wave Direction*

(C) *Mean Period*
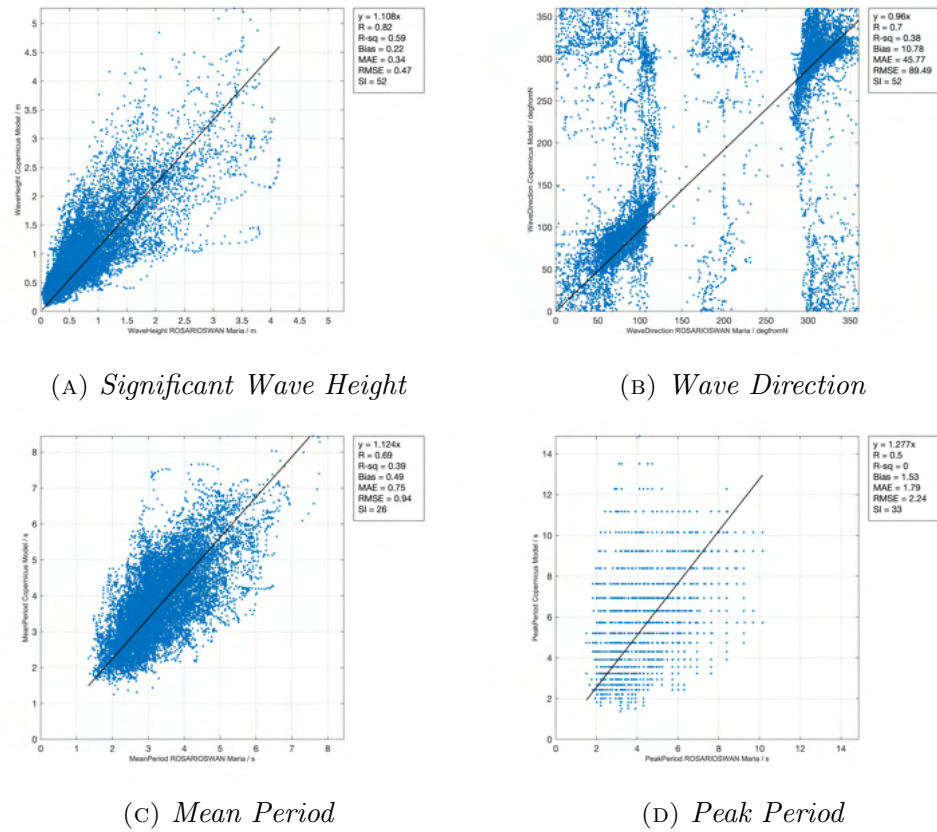
(D) *Peak Period*

FIGURE 5.30: *Correlation plots between ROSARIOSWAN Maria model and Copernicus model; forced-zero intercept regression*
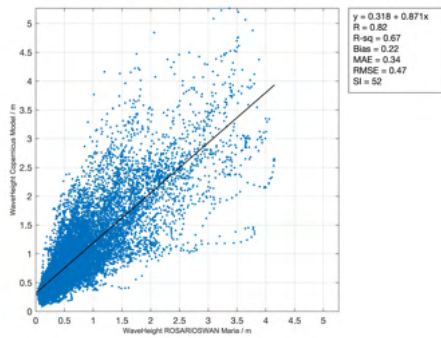
(A) *Significant Wave Height*
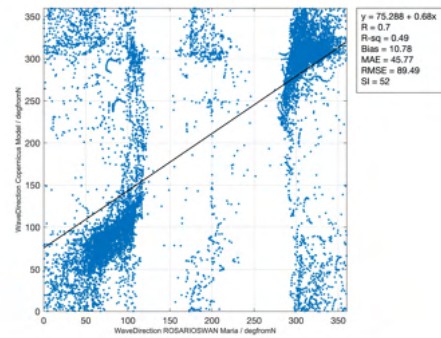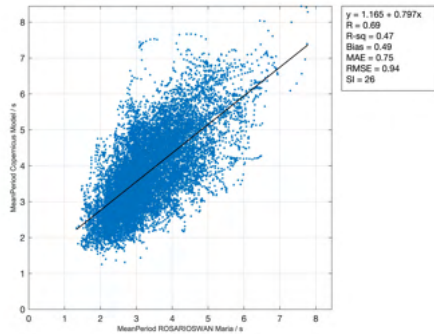
(B) *Wave Direction*
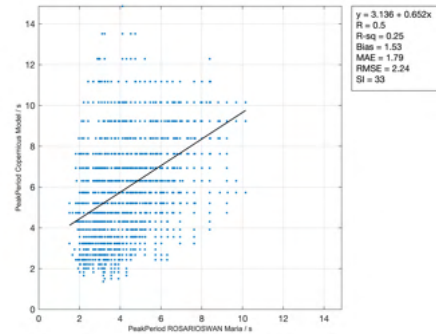
(C) *Mean Period*

(D) *Peak Period*

FIGURE 5.31: *Correlation plots between ROSARIOSWAN Maria model and Copernicus model; non-zero intercept regression*
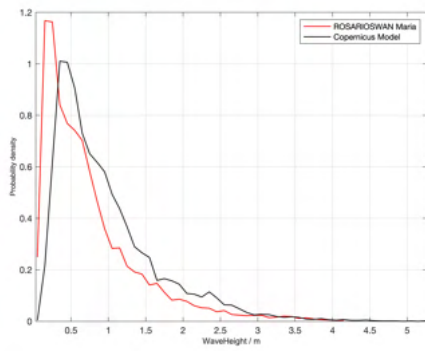
(A) *Significant Wave Height*
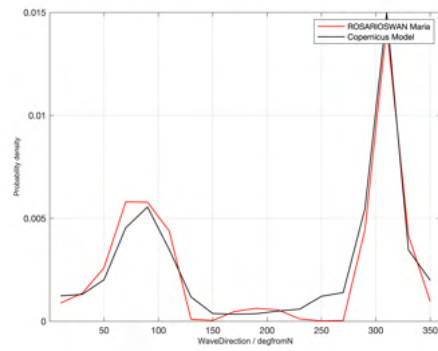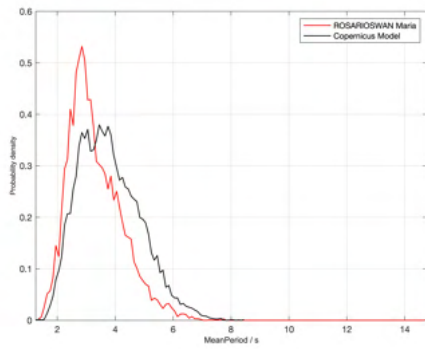
(B) *Wave Direction*
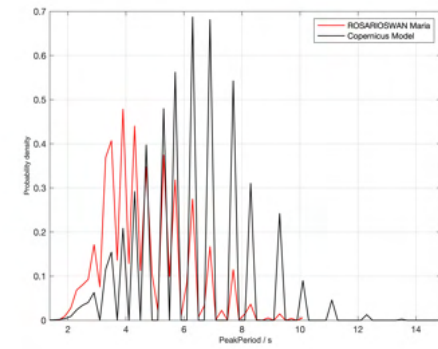
(C) *Mean Period*

(D) *Peak Period*

Figure 5.32: *Probability Density of ROSARIOSWAN Maria model (red) and Copernicus model (black) data*
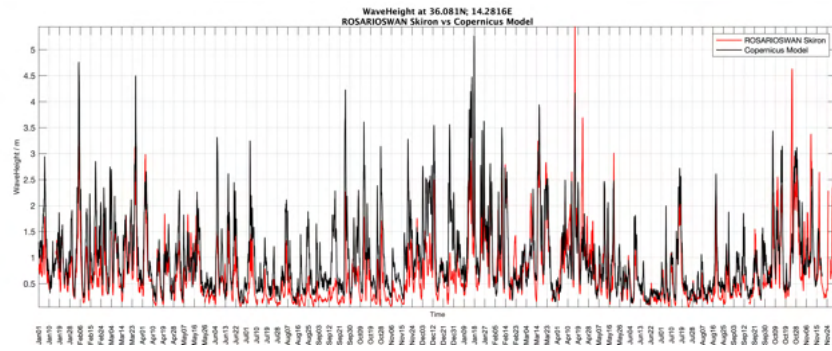
(A) *Significant Wave Height*
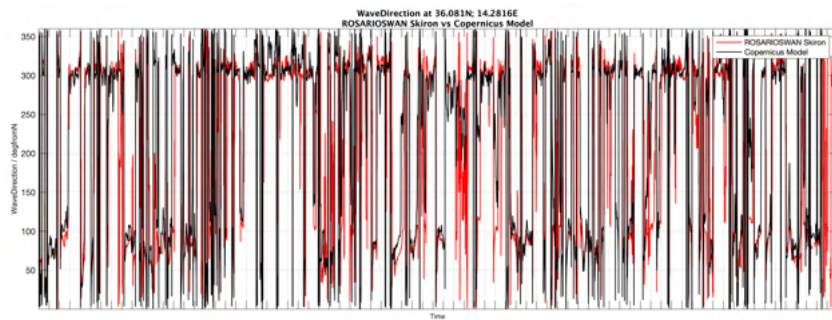
(B) *Wave Direction*
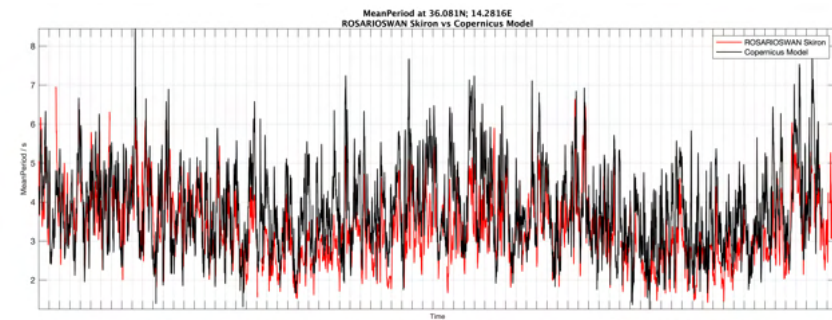
(C) *Mean Period*
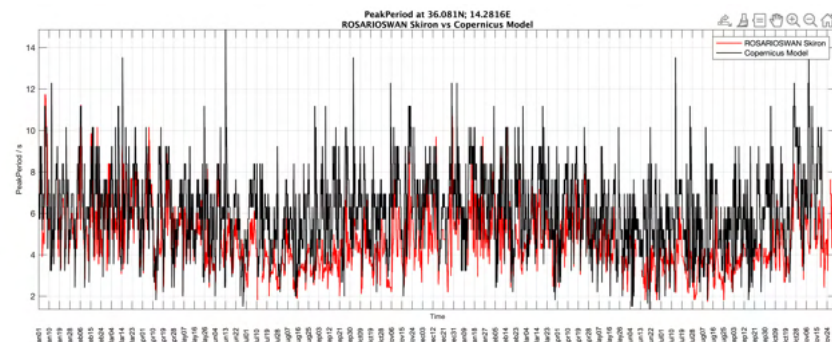
(D) *Peak Period*

FIGURE 5.33: *ROSARIOSWAN Skiron model (red) and Copernicus model data (black) from January 2020 to November 2021*

126

(A) *Significant Wave Height*

(B) *Wave Direction*

(C) *Mean Period*

(D) *Peak Period*
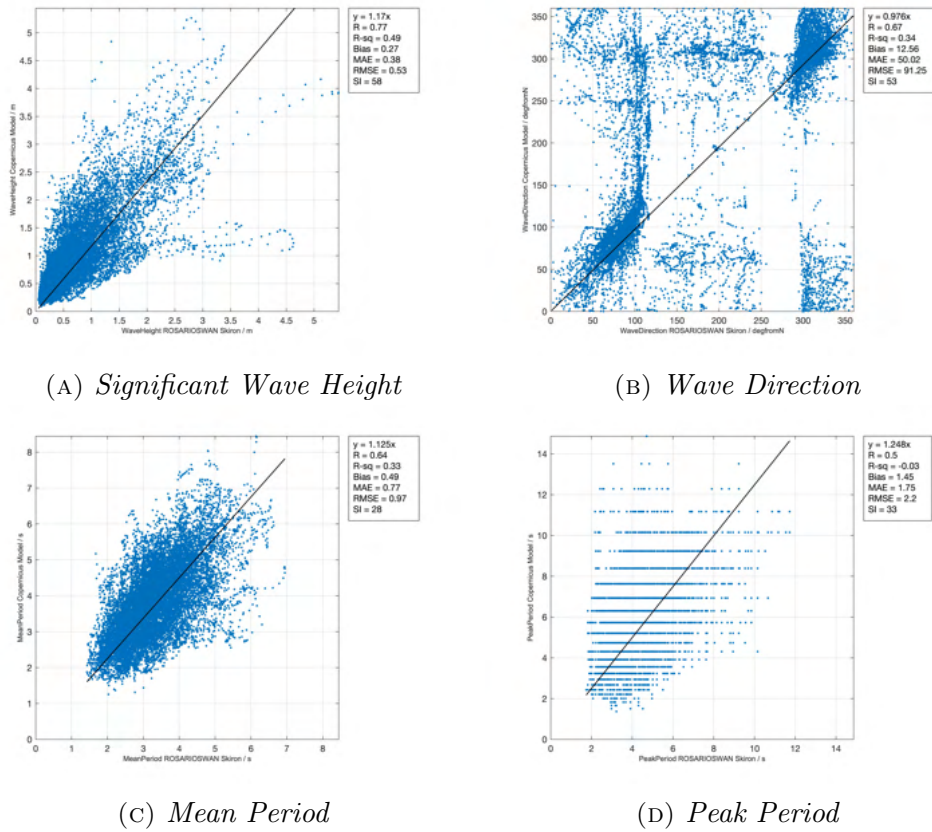
FIGURE 5.34: *Correlation plots between ROSARIOSWAN Skiron model and Copernicus model; forced-zero intercept regression*

(A) *Significant Wave Height*

(B) *Wave Direction*

(C) *Mean Period*
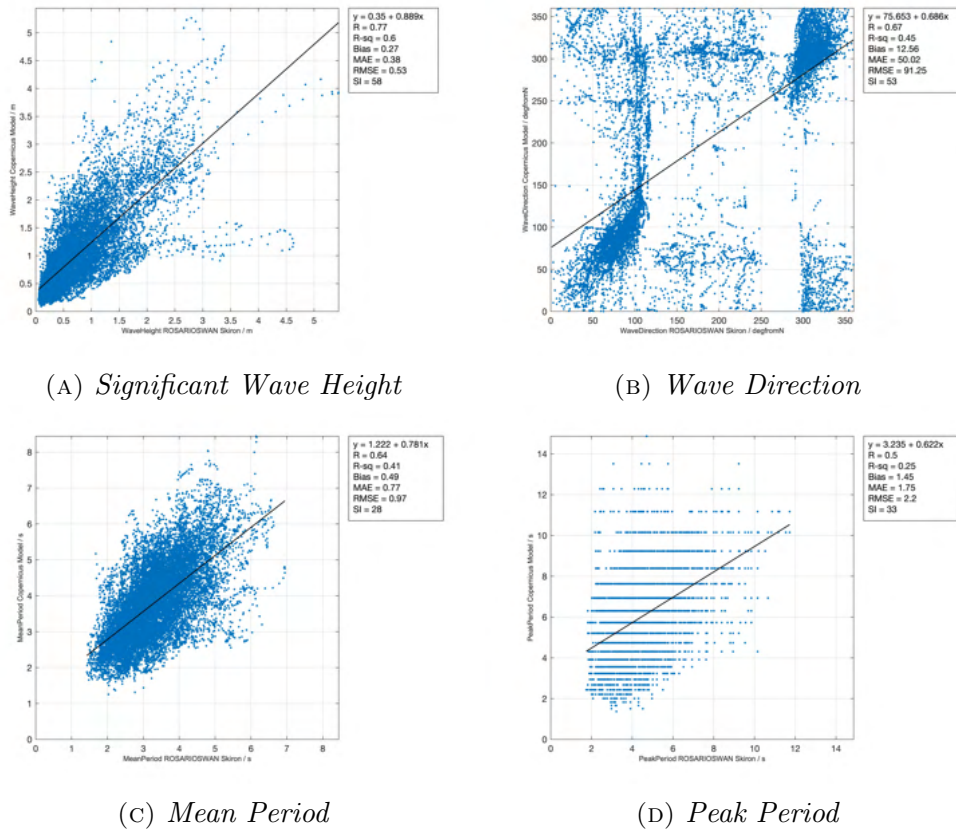
(D) *Peak Period*

FIGURE 5.35: *Correlation plots between ROSARIOSWAN Skiron model and Copernicus model; non-zero intercept regression*
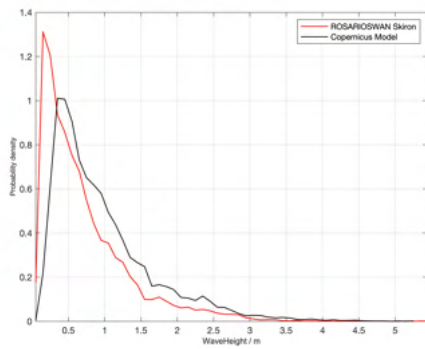
(A) *Significant Wave Height*
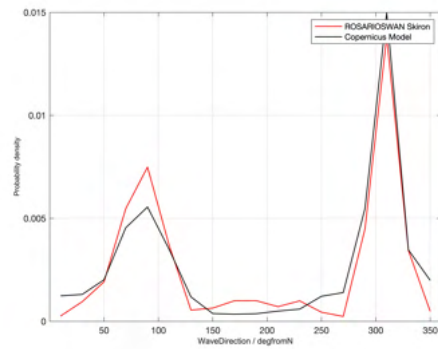
(B) *Wave Direction*
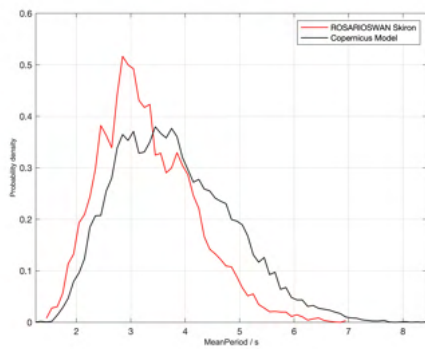
(C) *Mean Period*
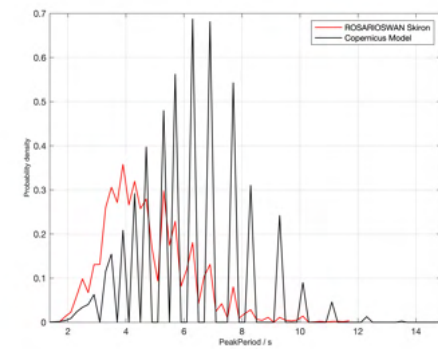
(D) *Peak Period*

FIGURE 5.36: *Probability Density of ROSARIOSWAN Skiron model (red) and Copernicus model (black) data*

TABLE 5.9: *Wave parameters' resulting correlation measures from Copernicus model and ROSARIOSWAN model data comparison for the period January 2020 - November 2021*

Wave Parameter	R	Bias	MAE	RMSE	SI
Maria					
SWH	0.82	0.22	0.34	0.47	52
Direction	0.7	10.78	45.77	89.49	52
Mean Period	0.69	0.49	0.75	0.94	26
Peak Period	0.5	1.53	1.79	2.24	33
Skiron					
SWH	0.77	0.27	0.38	0.53	58
Direction	0.67	12.56	50.02	91.25	53
Mean Period	0.64	0.49	0.77	0.97	28
Peak Period	0.5	1.45	1.75	2.2	33

TABLE 5.10: *Wave parameters' resulting linear regressions (non-zero and forced-zero intercept) from Copernicus model and ROSARIOSWAN data comparison for the period January 2020 - November 2021*

Wave Parameter	$y = mx + c$	R^2	$y = mx$	R^2
Maria				
SWH	$0.318 + 0.871x$	0.67	$1.108x$	0.59
Direction	$75.288 + 0.68x$	0.49	$0.96x$	0.38
Mean Period	$1.165 + 0.797x$	0.47	$1.124x$	0.39
Peak Period	$3.136 + 0.652x$	0.25	$1.277x$	0
Skiron				
SWH	$0.35 + 0.889x$	0.6	$1.17x$	0.49
Direction	$75.653 + 0.686x$	0.45	$0.976x$	0.34
Mean Period	$1.222 + 0.781x$	0.41	$1.125x$	0.33
Peak Period	$3.235 + 0.622x$	0.25	$1.248x$	-0.03

Looking at the probability distribution plots, Figures 5.32 and 5.36, one can note that the general distribution of densities is comparable between the datasets. In the case of the SWH and mean period, the ROSARIOSWAN model tends to output a higher density at the peak value, with this peak value being shifted lower than that associated with the Copernicus model data. In the case of the direction probability density, there is a good match in peaks at roughly Eastern and North-Western directions, as seen in previous

cases, where the ROSARIOSWAN model has a slightly higher density than the Copernicus model at the Eastern peak, with the opposite being the case for the North-Western peak. Finally, for the case of the peak period, the ROSARIOSWAN model peaks before the Copernicus case and at a lower value. It can be noted that the probability density of the ROSARIOSWAN is more 'continuous' in the sense that the area below this distribution is whole. In the case of the Copernicus model, the peaks are separated and narrow, leading to higher probability densities.

Table 5.9 shows that for the correlation parameters of the different ROSAR-IOSWAN models with the Copernicus model, these behave very similarly. From the values of R, it can be seen that the SWH in this case has the strongest correlation from the other wave parameters; the correlation is a good one, while, for the other parameters, the correlation is a moderate one. For each of the cases, based on the scale of the parameter values, the bias is not insignificant as neither is very close to zero, but they are also not excessively large either. Similar can be said for the cases of MAE and RMSE, where these are not insignificant. For the case of the scatter index, the parameter showing the lowest value is that of the mean period; this can be observed from the Figures 5.30c and 5.34c, where the data spreads the least from the other cases.

The linear regressions, Table 5.10, again clearly show the similarity of the regression between the Maria and Skiron case. For the non-zero intercept case, based on the value of R^2, the best fitting line is that calculated for the SWH, this is a further reflection of the good correlation between the datasets for this parameter. In a similar way, the other parameters' fits are weaker, with those for direction and mean period showing a moderate fit, and that for peak period a rather ill-fit. For the forced-zero intercept case, the R^2 values are worse, with the case for peak period showing clearly that

the fit is very ill-suited with a zero and negative value for the case of Maria and Skiron, respectively; the other fits are moderate for the mean period and direction, and good for the SWH.

5.4 Data Comparison: Other

In this Section, the relationships between the different sources of data, be it *in-situ*, remote sensing and model data, not yet considered are investigated. Further, the difference between forecast and hindcast analysis Copernicus model data is investigated through comparison with satellite data.

5.4.1 Satellite vs Copernicus model

Year-long satellite data of SWH, see Section 4.2.3, was obtained from 01/01/2020 midnight to 01/01/2021 midnight over the spatial area covered by the Copernicus data considered in this work; the resulting satellite tracks are given in Figure 5.37.

The orthodromic distance calculation, Section 3.1 is used in finding the closest Copernicus model point to each of the satellite readings. The satellite measurements, being instantaneous in time, are associated to the hourly Copernicus data by assigning those values with minutes ≤ 30 to the previous hour and those > 30 to the following hour; for example, a measurement at 17:26 would be assigned to hour 17 and a measurement at 17:36 would be assigned to hour 18.

Plotting these datasets against each other results in the plots with forced-zero intercept and non-forced intercept regressions in Figures 5.38 and 5.39, respectively. A scatter plot displaying the points from the different satellite
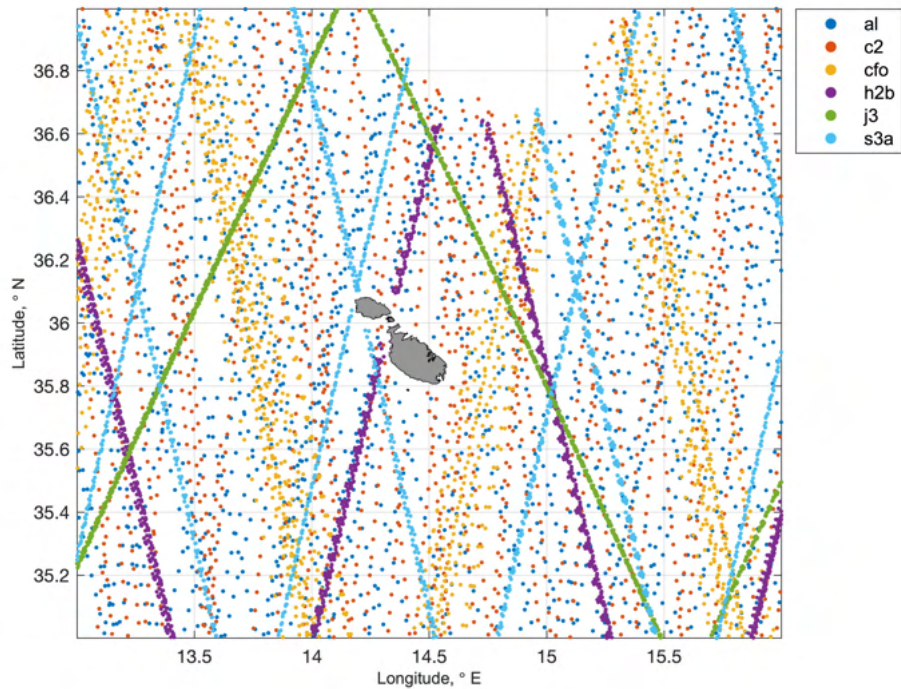
FIGURE 5.37: *Satellite tracks between 01/01/2020 and 01/01/2021 in the area bounded by 13-16E and 35-37N*

missions is also plotted in Figure 5.40.

Looking at both regressions, Figures 5.38 and 5.39, one can quickly note from only visual inspection that the data fits the regression quite well in both cases; in fact, up to two significant Figures, both R^2 values of the forced-zero intercept and non-forced intercept are 0.94. What this means is that the data comparison is good enough such that, forcing a zero-intercept doesn't change the line by a huge amount. This can be noted from the equations of both cases,

$$y = 0.966x$$

$$y = -0.017 + 0.977x,$$

133
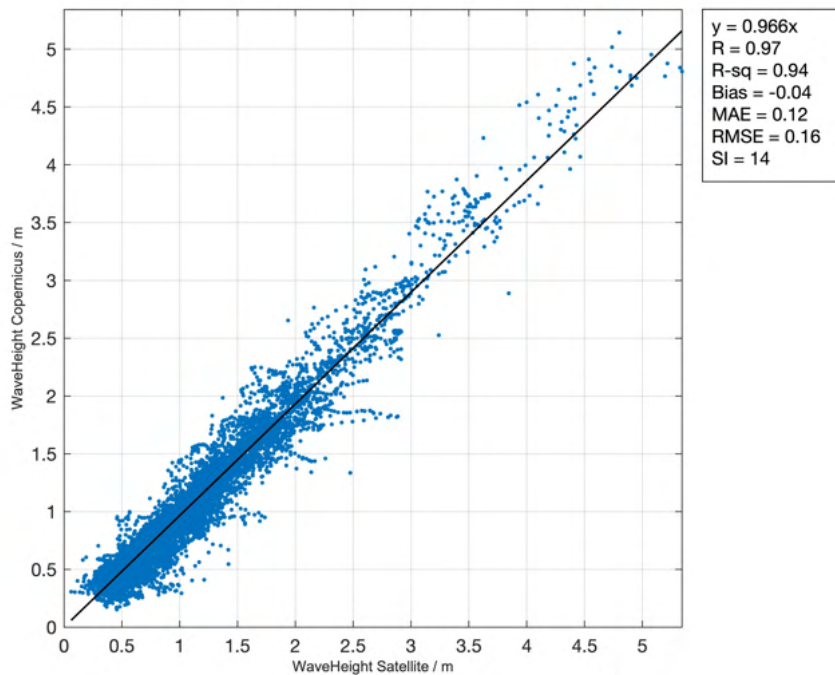
FIGURE 5.38: *Significant Wave Height correlation plot between Copernicus model and Satellite data between 01/01/2020 and 01/01/2021; forced-zero intercept regression*

where the gradients aren't very different from each other and the intercept is quite close to zero. Further indication that the datasets compare well together is the value of R, 0.97, which indicates a good fit. Additionally, the bias is quite close to zero at -0.04, while the MAE and RMSE are also low in value, 0.12 and 0.16, respectively. The SI in this case is 14%, indicating that the deviation of the point from the expected value, given the bias, is not too large. The good correlation between the two datasets can be also seen when looking at the probability density plot in Figure 5.41, where the peak curves are very similar in shape.

This good fit to a linear relationship can be expected since the hindcast analysis Copernicus model dataset is assimilated with Satellite data.
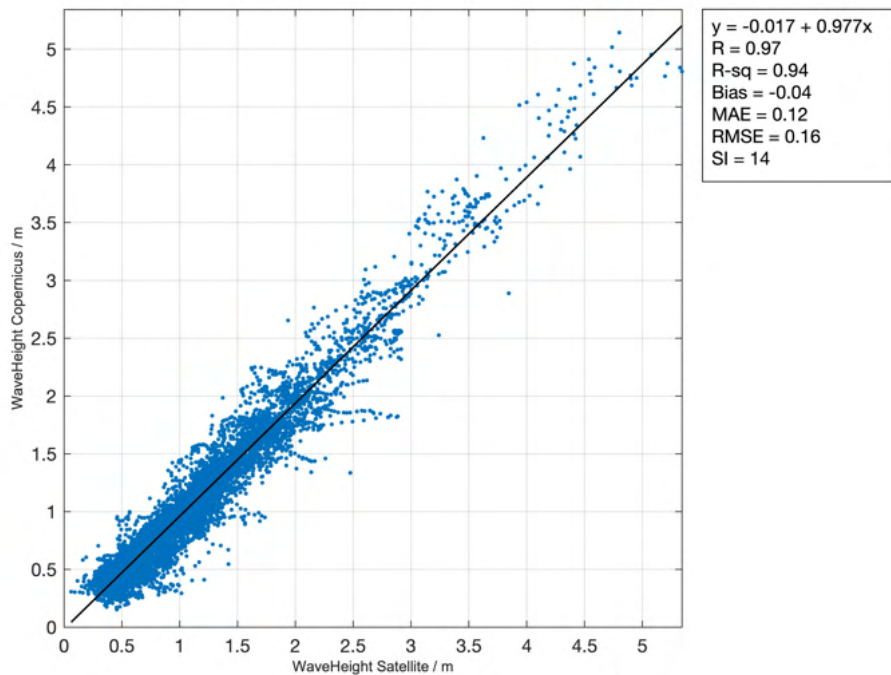
FIGURE 5.39: *Significant Wave Height correlation plot between Copernicus model and Satellite data between 01/01/2020 and 01/01/2021; non-zero intercept regression*

SWH Threshold Analysis

The probability of the Copernicus model being able to detect SWHs above a given threshold is plotted against the probability of it being a false alarm, using the method described in Section 3.2.4, where Satellite data is used as the reference dataset. The resulting plot is given in Figure 5.42, where thresholds are taken from $H_s = 0.5$ to 5 in steps of 0.5.

From this plot, it can be observed that the Copernicus model has a good PD of sea states when thresholds of H_s fall in the range 0.5-4.5; these values all lie in the 80-100% probability range. For the most part, the points seem to cluster in the top left area of the plot with a PFA under 20%. For $H_s > 3.5$ and 4.5, the values of PFA are closer to 30%. There is then a dramatic

135
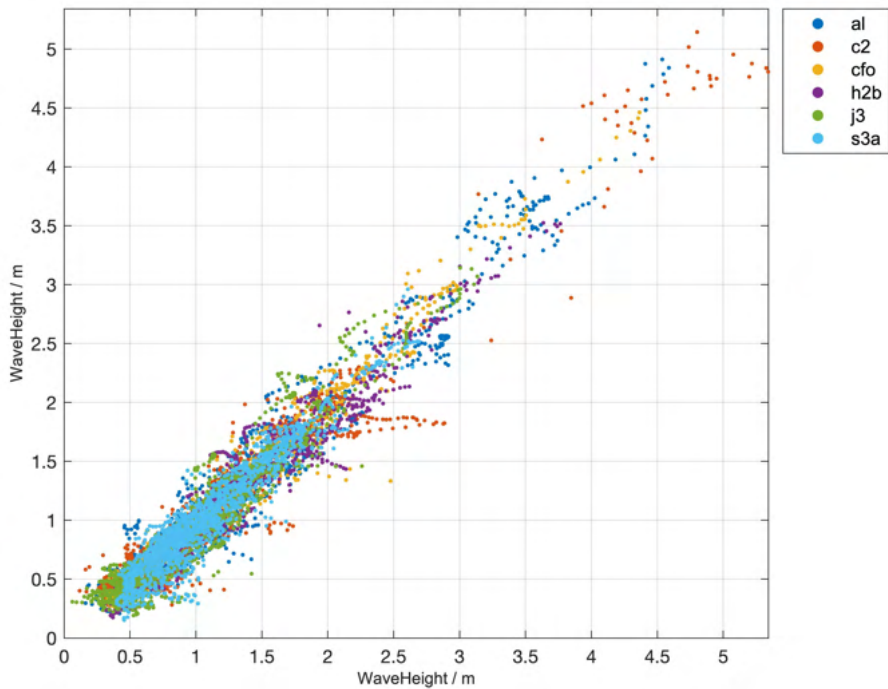
FIGURE 5.40: *Significant Wave Height correlation plot between Copernicus model and Satellite data between 01/01/2020 and 01/01/2021; classified by satellite type*

drop to zero in PD for the case of $H_s > 5$, with an associated PFA of 100%. This extreme value is likely to be the result of the small number of events that satisfy this threshold value, and so, the data might not be sufficient to represent this situation well.

Save for the aforementioned extreme case, the PD performance is quite good in this case, without a significant increase in PFA. A better performance is then observed when carrying out threshold analysis for Copernicus model data with the satellite data, rather than with the buoy data (Section 5.1.1). This is again likely the result of the Copernicus model data being assimilated with satellite data, hence, comparing well to it.
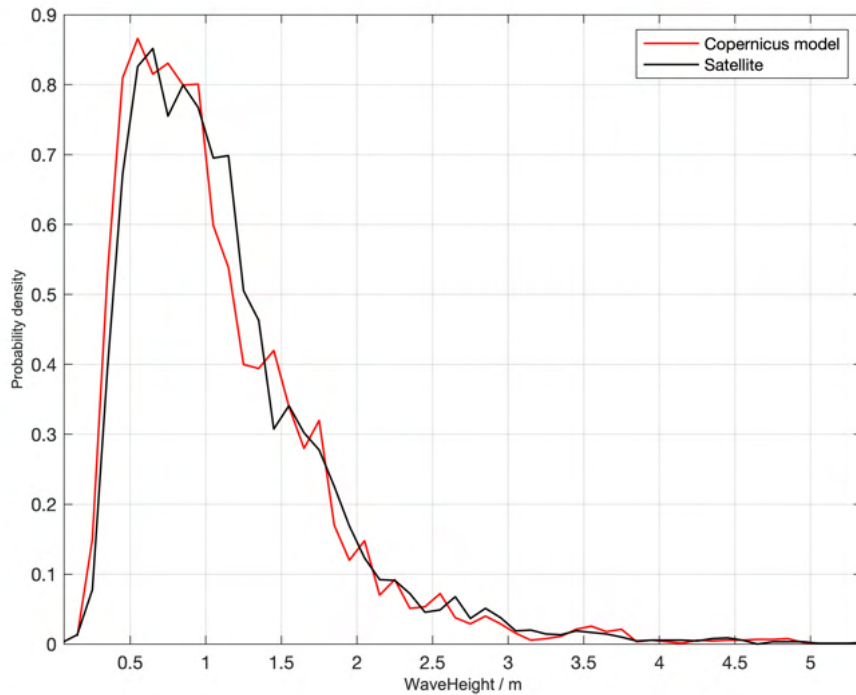
FIGURE 5.41: *Probability Density of Copernicus model (red) and Satellite (black) data*

5.4.2 Satellite vs Copernicus model: forecast vs hindcast analysis

Given the fact that the Satellite data considered is assimilated with the Copernicus model in the hindcast analysis data, it would be of interest to compare the forecast model output to the re-analysed model output. For this purpose, 10 day forecast data was obtained from the Copernicus model on 19/11/2021, spanning between 19/11/2021 12:00 and 28/11/2021 11:00. The same range of model data was then extracted on the 29/11/2021 as the model data would then be the re-analysed, thus assimilated, version. The satellite tracks that fall in this time bracket, and hence the ones used for comparison, are illustrated in Figure 5.43.

Scatter plots have been plotted for both the forecast and hindcast analysis
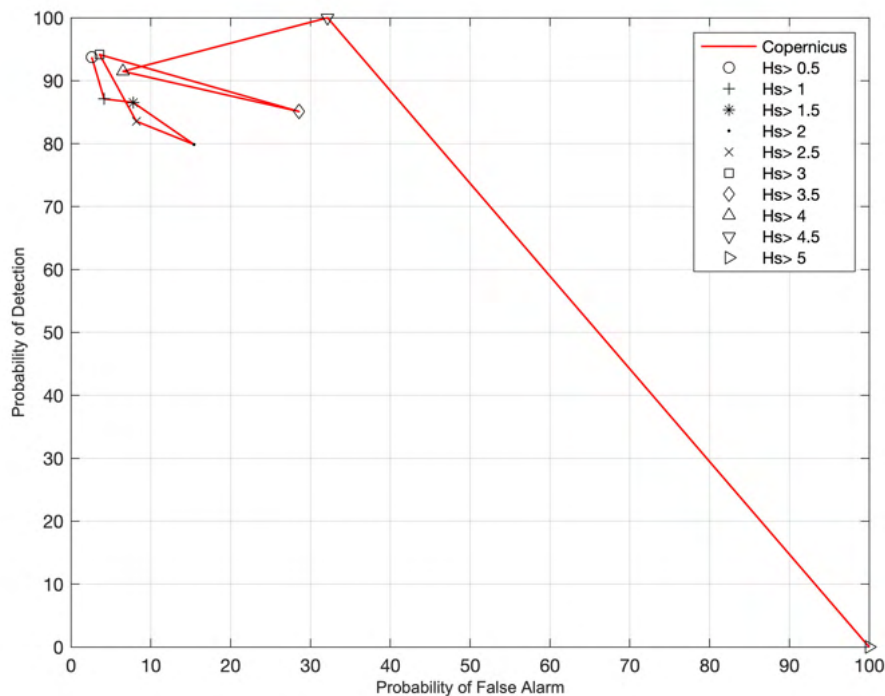
FIGURE 5.42: *Copernicus model Data SWH Threshold Analysis; tested against satellite data*

data, and are plotted side-by-side for ease of comparison; Figures 5.44, 5.45 and 5.46, show the scatter plots separated according to satellite type, with a forced-zero intercept linear regression, and with a non-zero intercept linear regression, respectively.

Additionally, the probability densities and SWH threshold analysis were also similarly plotted in Figures 5.47 and 5.48.

One can quickly note, by comparing Figures 5.44a and 5.44b that the correlation between the datasets is much more linear in the case of the hindcast analysis data, as is to be expected because of the assimilation. This improvement in correlation is further shown in the linear regression fits in Figures 5.45 and 5.46. For the case of the forced-zero intercept, Figure 5.45, the linear fit performs better in the hindcast case, with and increase in R^2
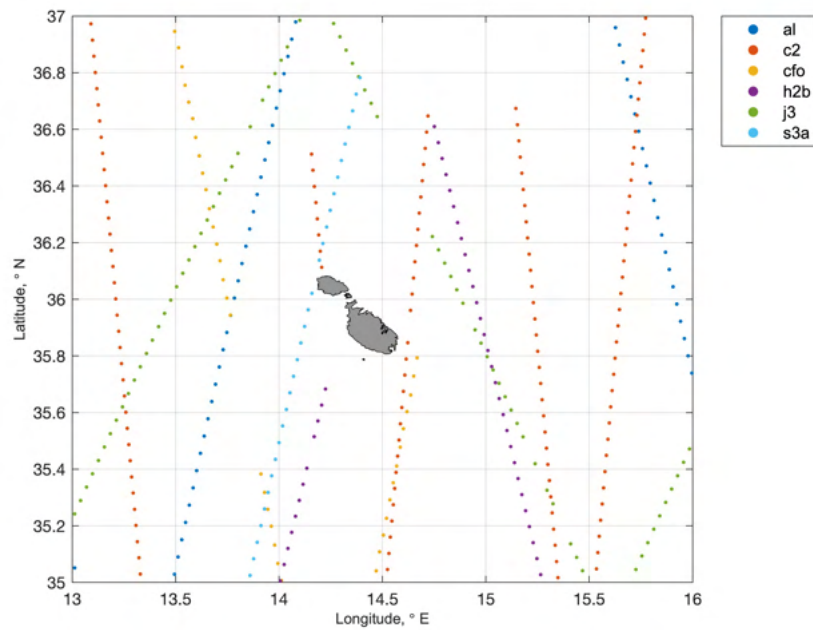
FIGURE 5.43: *Satellite tracks between 19/11/2021 12:00 and 28/11/2021 11:00 in the area bounded by 13-16E and 35-37N*

(A) *Forecast*

(B) *Re-analysis*
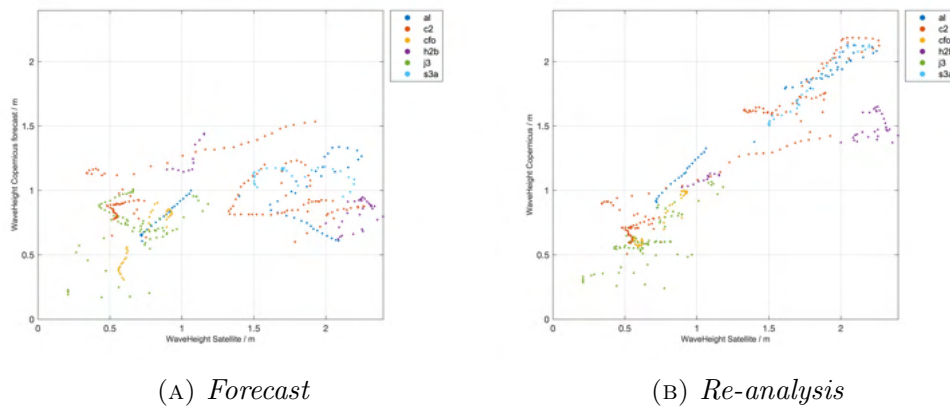
FIGURE 5.44: *Correlation plots between Copernicus model and Satellite data separated by Satellite type between 19/11/2021 12:00 and 28/11/2021 11:00*

from -1.63 to 0.79, indicating that the linear regression represents a strong relationship. In the case of the non-zero intercept, Figure 5.46, again the linear fit performs better in the hindcast case, with and increase in R^2 from 0.13 to 0.84, which are, in turn, improvements over the values in the forced-zero intercept case. The fit is then the strongest for the hindcast, non-zero

139

(A) *Forecast*

(B) *Re-analysis*
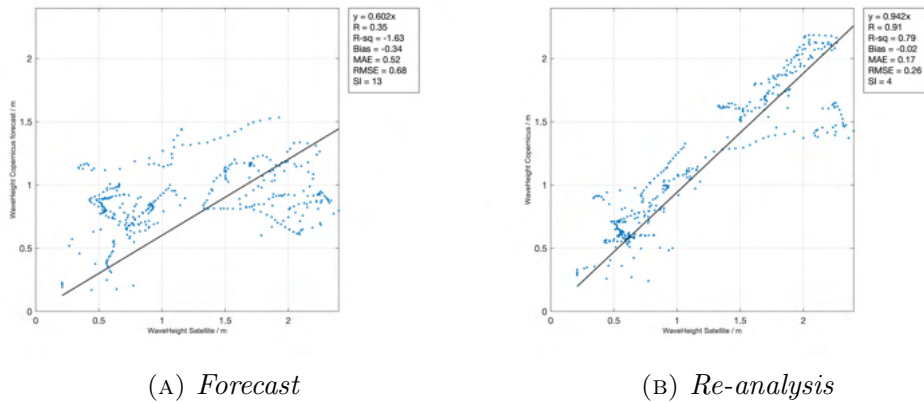
FIGURE 5.45: *Correlation plots between Copernicus model and Satellite data between 19/11/2021 12:00 and 28/11/2021 11:00; forced zero-intercept regression*

(A) *Forecast*

(B) *Re-analysis*
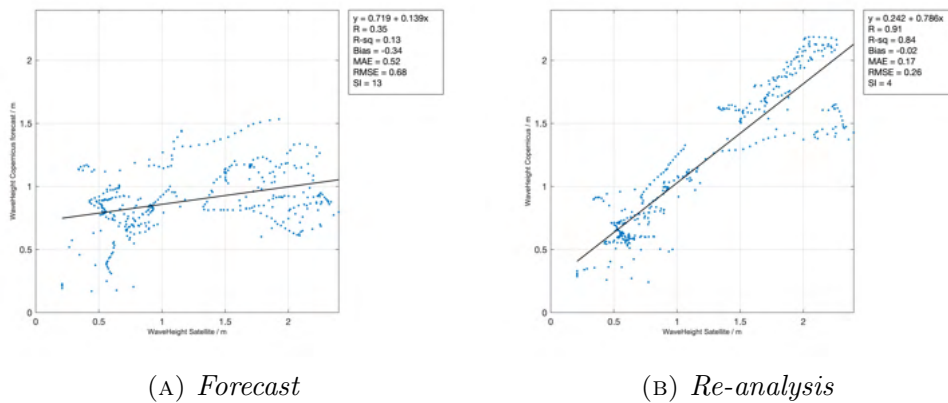
FIGURE 5.46: *Correlation plots between Copernicus model and Satellite data; non-zero-intercept regression*

intercept correlation plot.

As a further comparison of the forecast and hindcast correlations with satellite data, the correlation measure R also improved from a value of 0.35 to 0.91, again indicating a very strong relation between the values. Additionally MAE, RMSE and SI all improved with values decreased by approximately 67%, 62% and 69%, respectively. The resulting bias is also closer to zero at -0.02. The probability density fit is also improved, see Figure 5.47, in the hindcast case. In the forecast probability density, the Copernicus model

(A) *Forecast*
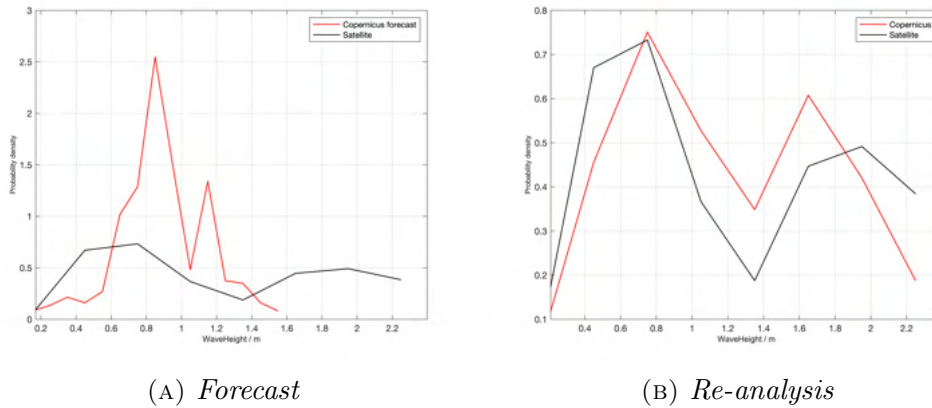
(B) *Re-analysis*

FIGURE 5.47: *Probability Density of Copernicus model (red) and Satellite (black) data between 19/11/2021 12:00 and 28/11/2021 11:00*

(A) *Forecast*
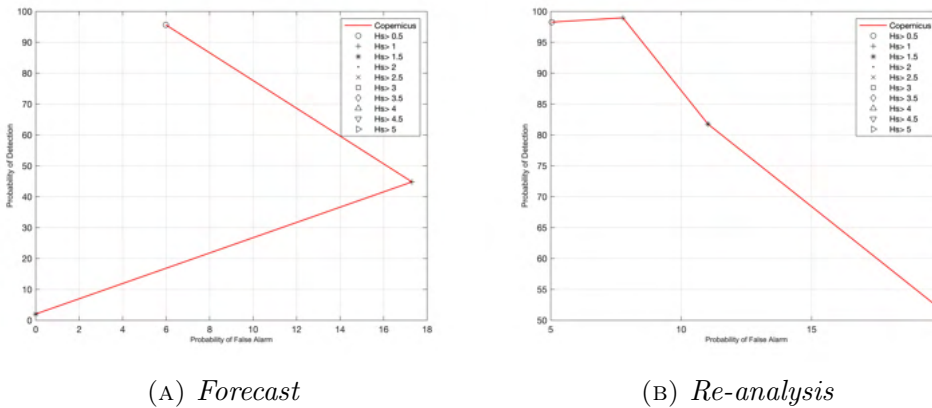
(B) *Re-analysis*

FIGURE 5.48: *Copernicus Data SWH Threshold Analysis between 19/11/2021 12:00 and 28/11/2021 11:00; tested against satellite data*

correctly predicted two peaks of SWH values, but at the incorrect values with a much less broad distribution. In the case of the hindcast, the two peaks more closely match those corresponding to the satellite data.

As a final note, a SWH threshold analysis was carried out on the data for the sake of rough comparison, since, the amount of data is limited to 10 days. Looking at Figure 5.48, it can be noted that the PD quickly disintegrates in the case of the forecast data for $H_s > 1.5$, where it is very close to zero. In contrast, in the hindcast case, the PD and associated PFA are $\sim 82\%$ and $\sim 11\%$, respectively, for the same point, which is much better. The last

141

point in the re-analyses case, $H_s > 2$, the PD and PFA have values of $\sim 52\%$ and $\sim 20\%$, respectively.

5.4.3 *In-situ* and remote-sensing measurement comparison

The comparison of different measurements, *in-situ* and remote sensing, with each other is slightly more complicated than that of comparison of measurements with model data. This is because measurements have a generally more limited spatial and/or temporal coverage of an area (as discussed in Section 2.1), and so, overlap between different sources might be difficult to obtain. In this Section, the comparisons between buoy, satellite and radar measurements are presented.

Buoy vs Satellite

In order to find Satellite data points in the vicinity of the buoy, a circular region of radius $0.05°$ was considered, see Figure 5.49. This distance was chosen such that at least one satellite point for which buoy data was available could be compared; the satellite dataset range in this case spanned from January 2020 to November 2021. Indeed, over the one year buoy data available, only one satellite point could be considered for comparison, this is presented in Table 5.11. Based on this singular data point, it can be seen that the values are relatively close to each other, with a difference of 0.121 m, with the Satellite outputting the lower of the values. Considering the proximity of the point to shore, it seems that there is no clear error resulting from reflection off land mass by the satellite.
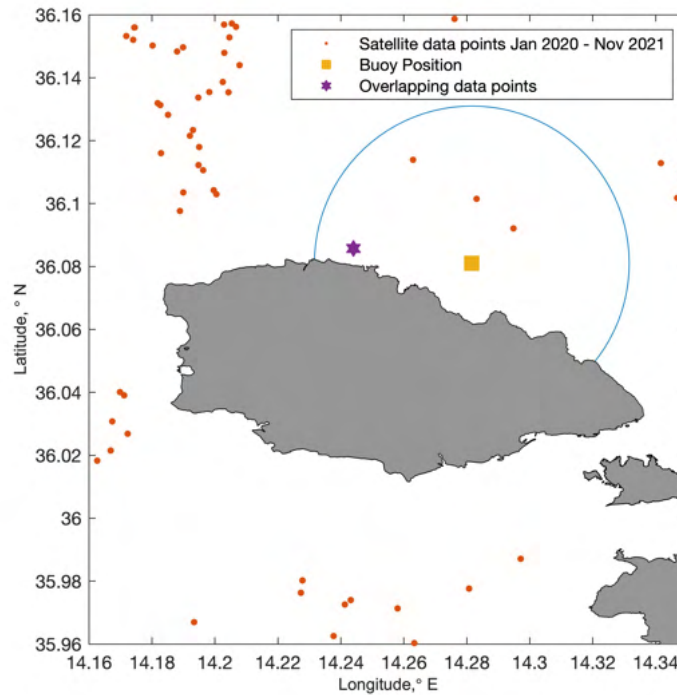
FIGURE 5.49: *Satellite and buoy overlapping data for the period 04/08/2020 - 12/07/2021*

TABLE 5.11: *Satellite and buoy overlapping SWH data for the period 04/08/2020 - 12/07/2021*

Date and Time	Latitude	Longitude	Satellite	Distance from buoy	Buoy
23/03/2021 23:00	36.0858°N	14.2440°E	2.2590 m	3.42 km	2.3800 m

Radar vs Satellite

In order to find Satellite data points that intersect with the SOPU radar's second annular ring, which is 5.85 km away from the station (a radius of about 0.0527°), a ring segment extending from shore to shore is considered. The ring is made of two concentric circles of radii 0.0580° and 0.0474° were considered, see Figure 5.50. This distance was chosen such that at least one satellite point for which radar data was available could be compared. Again, over the one year buoy data available, only one satellite point could
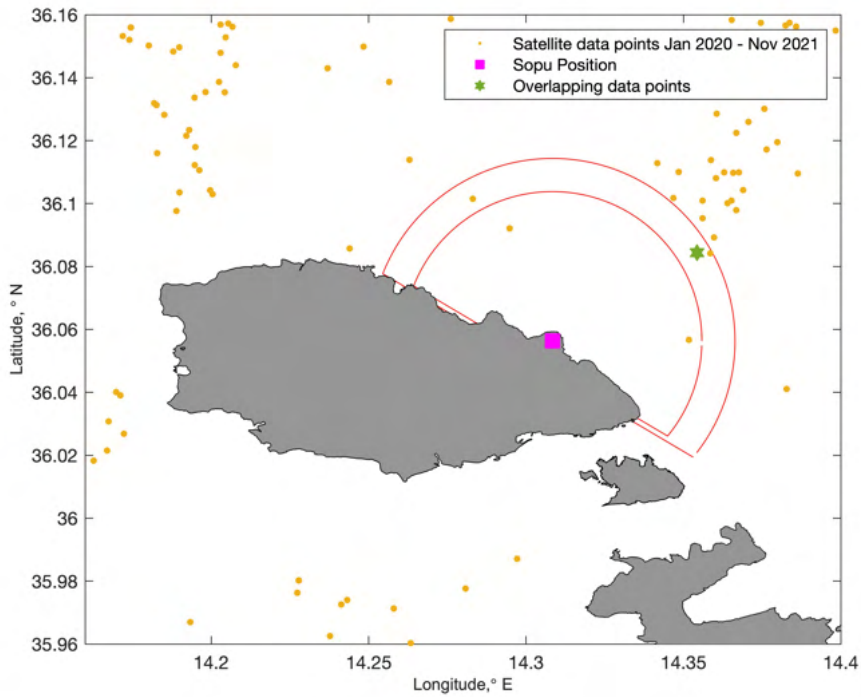
Figure 5.50: *Satellite and SOPU radar overlapping data for the period 04/08/2020 - 12/07/2021*

be considered for comparison, this is presented in Table 5.12. Based on this singular data point, it can be seen that the value pair aren't very well matching, with the Satellite data being more that double that of SOPU radar. Considering that in the previous case, when comparing the singular buoy and satellite point, there was quite a good match between the values, it might be the case that the erroneous value in this case is that from the SOPU radar. However, given the very limited points available for comparison, this cannot be concluded here.

Table 5.12: *Satellite and SOPU radar overlapping SWH data for the period 04/08/2020 - 12/07/2021*

Date and Time	Latitude	Longitude	Satellite	Distance from SOPU station	SOPU radar
25/10/2021 06:00	36.0844°N	14.3543°E	1.3910 m	5.17 km	0.6050 m

Buoy vs Radar

As discussed in Section 4.2.2, the available data for the SOPU radar at the distance closest to the buoy point has several missing values, hence, the points coinciding with the one-year buoy dataset is more-so limited. This can be visualised from the time-series plots of the two datasets in Figure 5.51.
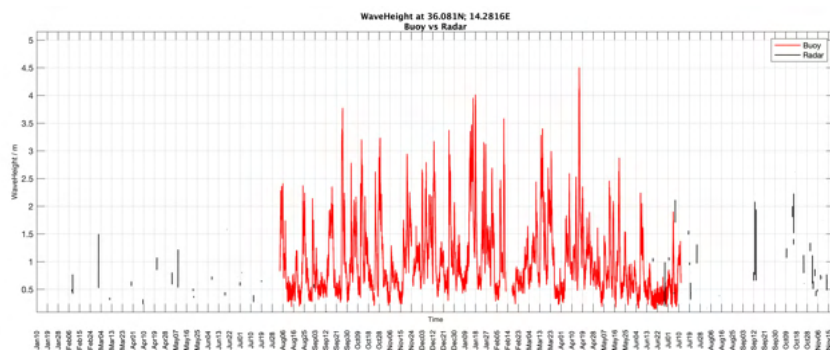
(A) *Significant Wave Height*
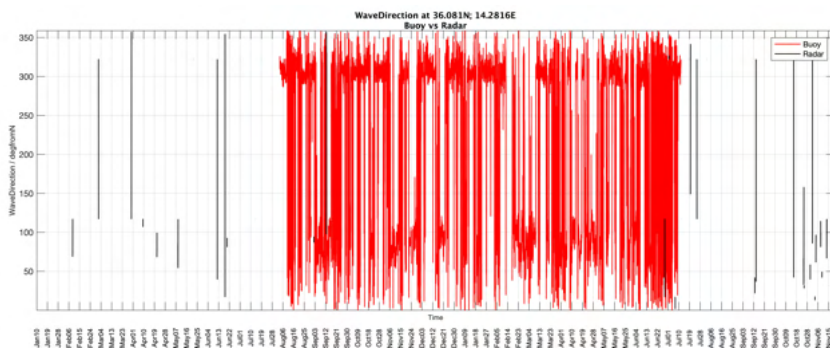
(B) *Wave Direction*
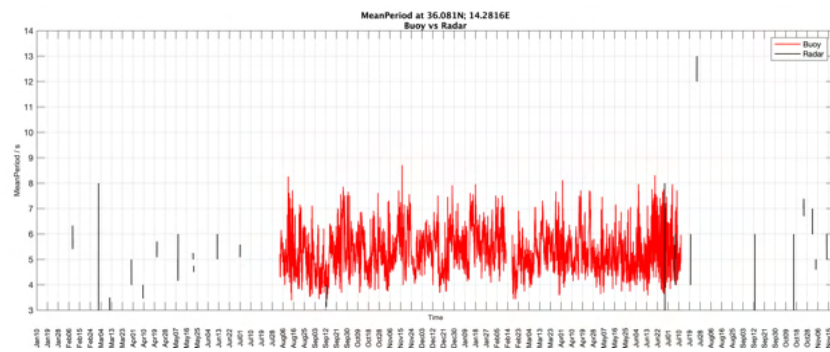
(C) *Mean Period*

FIGURE 5.51: *SOPU HF Radar (red) (Jan 2020 - Nov 2021) and Buoy (black) (Aug 2020 - Jul 2021) time series data*

The limited number overlapping points, 45 out of a possible 8030 ($\sim 0.6\%$ of the buoy dataset), mean that the correlation analysis and regression did not yield any useful results, and are thus not plotted here; the resulting correlation and regression measures are however presented in Tables 5.13 and 5.14, respectively. A moderate correlation is found for the case of the direction, which yields a weak fit in both linear regressions. The SWH's R value indicates a weak correlation, but the resulting linear regressions are very ill-fitting. The mean period shows almost no correlation and has ill-fitting regressions.

TABLE 5.13: *Wave parameters' resulting correlation measures from SOPU radar and buoy data comparison for the period 04/08/2020 - 12/07/2021*

Wave Parameter	R	Bias	MAE	RMSE	SI
SWH	0.21	0.11	0.49	0.86	25
Mean Period	0.04	1.76	1.92	2.73	10
Direction	0.57	-26.97	71.55	118.19	17

TABLE 5.14: *Wave parameters' resulting linear regressions (non-zero and forced-zero intercept) from SOPU radar and buoy data comparison for the period 04/08/2020 - 12/07/2021*

Wave Parameter	$y = mx + c$	R^2	$y = mx$	R^2
SWH	$0.66 + 0.293x$	0.05	$0.85x$	-0.21
Mean Period	$5.187 + 0.074x$	0	$1.376x$	-0.55
Direction	$53.737 + 0.613x$	0.32	$0.807x$	0.28

5.5 Power Calculations

The wave power is first calculated over a one-year period, between 04/08/2020 and 12/07/2021, near the position of the buoy for the datasets of the buoy, Copernicus Model, ROSARIOSWAN Maria and ROSARIOSWAN Skiron models in order to compare the outputs by using the method described in Section 3.3.1.

It is helpful to be able to visualise the power and energy available over the region under consideration for ease of comparison between different areas. It is also useful to use this visualisation with forecast model data, such that the power in the sea waves can be anticipated ahead of time. This can be done for a number of forecast time windows and displayed in succession in the form of an animated sequence of forecasts.

The power maps of the spatial domain under consideration are then found by using the same method describe in Section 3.3.1 but for every single point. For the case of the Copernicus model data, the variable T_E is used directly in the equation since this is an output variable, VTM10 (see Table 4.1), of the model. For the case of the ROSARIOSWAN data, the peak period T_p is used as the energy period is not an output of the model, see Table 4.2.

5.5.1 At buoy position

Here, the yearly averaged power at the buoy point is presented in Table 5.15

The power is overestimated by 1.3864 kW/m by the Copernicus Model when compared to the result from the buoy data, while the ROSARIOSWAN Models underestimate the power output by 0.5037 and 1.0642 kW/m by the Skiron and Maria versions, respectively. The underestimation by the

TABLE 5.15: *Power calculation at buoy position between 04/08/2020 and 12/07/2021*

Data	Power / kW/m
Buoy	3.4816
Copernicus Model	4.8680
ROSARIOSWAN Skiron Model	2.9779
ROSARIOSWAN Maria Model	2.4174
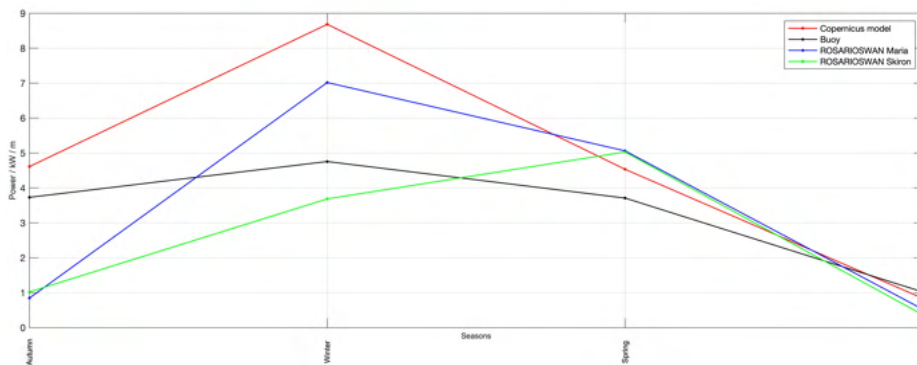
FIGURE 5.52: *Seasonal average wave power between 04/08/2020 08:00 and 12/07/2021 06:00*

ROSARIOSWAN model is likely a result of the underestimation by this model, for both Maria and Skiron, of the SWH and peak period parameters, as discussed in Sections 5.1.2 and 5.1.3.

The time series average power for each month and season, for each of the datasets, are plotted in Figures 5.52 and 5.53, respectively, for a visual representation of the variability of the power on these time scales.

For the case of the seasonal mean values, Figure 5.52, it can be noted that the datasets' outputs are closest in value during Spring and Summer, and the largest variation occurs in Winter. The outputs of the ROSARIOSWAN models Skiron and Maria, have values which are relatively close during Autumn, Spring and Summer, but deviate during Winter.

For the case of the monthly mean values, Figure 5.53, the datasets' outputs
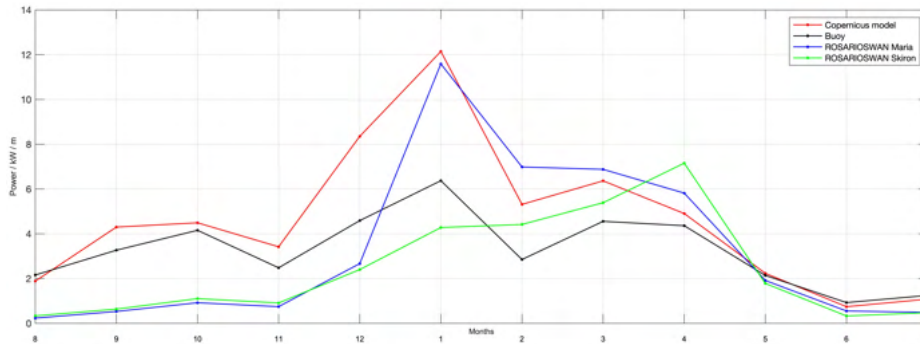
FIGURE 5.53: *Monthly average wave power between 04/08/2020 08:00 and 12/07/2021 06:00*

are closest in value during May, and the largest variation occurs during January. ROSARIOSWAN models Skiron and Maria match fairly well between August and December and between May and July. Between January and April, ROSARIOSWAN Maria has output values closer to the Copernicus model, which both show a large overestimation when compared to the buoy values. The Copernicus model and buoy outputs are close between August and November, and between April and July, with a slight overestimation by the model. ROSARIOSWAN Skiron likely has the closest annual mean due to having both underestimations and overestimations with no extreme jumps.

Power directional histogram

Additionally, directional histograms of the power output over this one year period are also plotted, Figure 5.54, for each dataset in order to be able to compare the outputs by each model as compared to the *in-situ* measurements. The binning is done with a width of 22.5° with bin centers starting at 0°. Each bar is divided into up to five segments indicating the proportion of the binned power data which is ≤ 1 kW/m, in the ranges 1-2, 2-3, 3-4 kW/m and that > 4 kW/m.

(A) *Buoy*

(B) *Copernicus Model*

(C) *ROSARIOSWAN Skiron*

(D) *ROSARIOSWAN Maria*
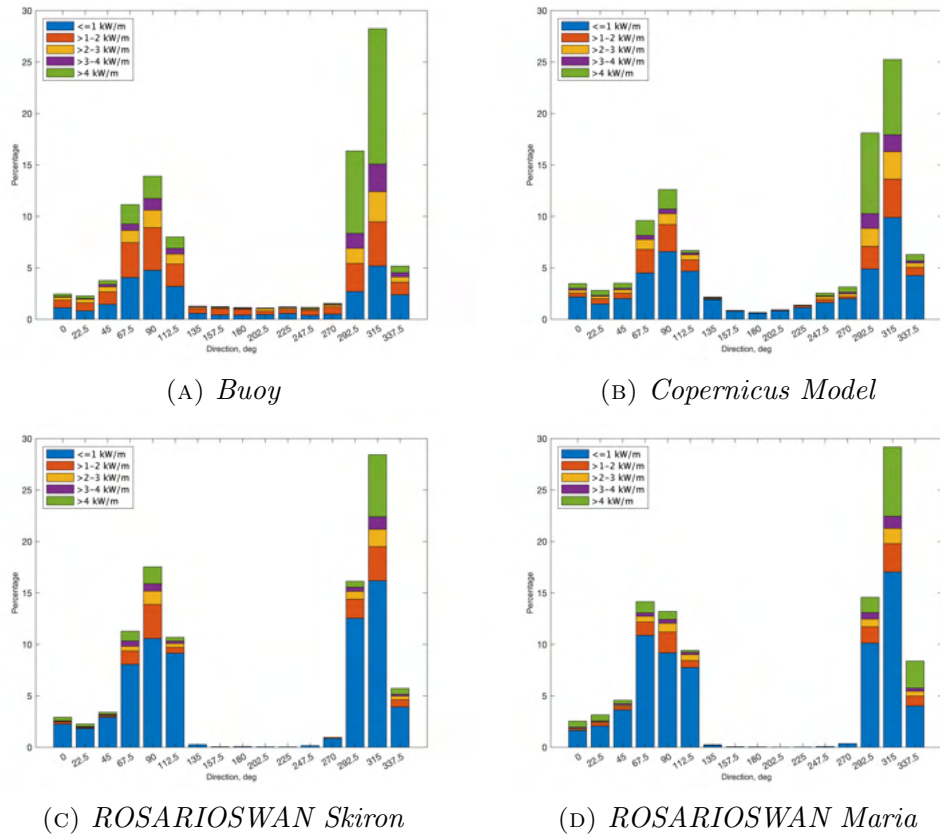
FIGURE 5.54: *Wave power (kW / m) directional histogram between 04/08/2020 and 12/07/2021*

Looking at the plots in general, it can be noted that the histograms show two main peaks at 90° and 315°, which correspond to Eastern and North-Westerly directions. This is consistent with what is discussed in Sections 5.1-5.3 when wave direction is available, as these show the high occurrence of waves from these directions. It can be noted that the high North-Westerly wave occurrence coincides with the most common wind direction experienced on the Maltese Islands which, on average, blows 20.7% of the days in a year [102].

The best agreement in these directional histograms exists between the buoy data and Copernicus model datasets, Figures 5.54a and 5.54b, respectively, where the shape and distribution of wave power in the bins is comparable.

150

The Copernicus model does however tend to overestimate the proportion of waves which have power < 1 kW/m, and in turn, underestimate those with power > 4 kW/m between 292.5° and 337.5°. In the direction ranges 0°-112.5° and 292.5°-337.5°, the Copernicus model also tends to underestimate the intermediary ranges of the wave power. In the direction range 135°-270°, the Copernicus model shows the highest occurrence of wave power is of < 1 kW/m, while the same range from the buoy data indicates that the highest occurrence is of waves with power in the range 1-2 kW/m.

Comparing first the two ROSARIOSWAN Models with each other, Figures 5.54c and 5.54d, it can be noted that there is a large underestimation of the power in the direction range 135°-270° in both cases when compared to the buoy data histogram. Another common feature of both ROSARIOSWAN Model histograms is that, as in the case of the Copernicus model, they tend to overestimate the proportion of waves which have power < 1 kW/m, and underestimate the remaining ranges. Comparing the ROSARIOSWAN Maria model to the buoy data histogram reveals that the shape of the consecutive bars matches less (with the buoy case) than in the case of the the ROSARIOSWAN Skiron model. This can be noted in the range 67.5°-112.5°, where the bars are consecutively decreasing in magnitude rather than first increasing and then decreasing to a lower percentage than the first, and in the range 0°-45°, where the bars are consecutively increasing in magnitude rather than first decreasing and then increasing to a higher percentage than the first. It would seem then that the ROSARIOSWAN Skiron model is better at representing the directional power distribution than the ROSARIOSWAN Maria model.

5.5.2 Copernicus Model Map

In this Section, power maps have been plotted for the Copernicus model dataset, that described in Section 4.1.1, using the process described in Section 3.3.1. The plots presented here are the resulting power plots for three time averaging windows: one year, 24hr and 1hr.

Forecast and hindcast analysis

Since the Copernicus model gives both forecast and re-analysed data, it would be of interest to compare the resulting power plots of the same time span, but one is data obtained from forecast and the other from the hindcast. The plots for the hindcast and the forecast are given in Figures 5.55 and 5.56, respectively.

It can be noted that, when comparing the day-averaged plots, Figures 5.55b and 5.56b, the plots are relatively similar. In particular, one can note that both plots depict lower power values to the West of Malta (and Sicily), a result of shadowing by the land. Additionally, towards the East, there is an increase in wave power, especially towards the bottom right of the plots, this is likely a result of the larger fetch from the East as opposed towards the North or South. What can be noted is that, in the case of the low-power shadows, the forecast seems to overestimate how far these extend; this can be noted from the 0.9 kW/m isoline, which is much closer to land in the case of the hindcast data. The increase in power towards the right is fairly similar in both cases, with the forecast showing a slight overestimation at the bottom right area.

Looking at the hour plots, Figures 5.55a and 5.56a, it can be noted that the plots are again relatively similar. In the case of the hindcast data, the
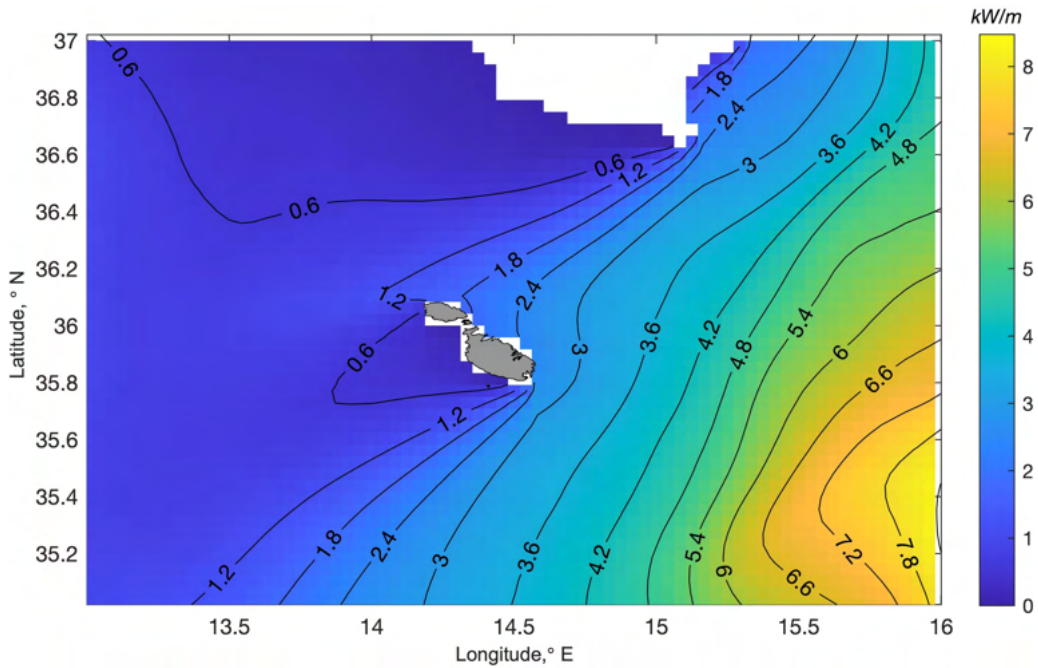
(A) *1 hour window: 20/11/2021 14:00:00*
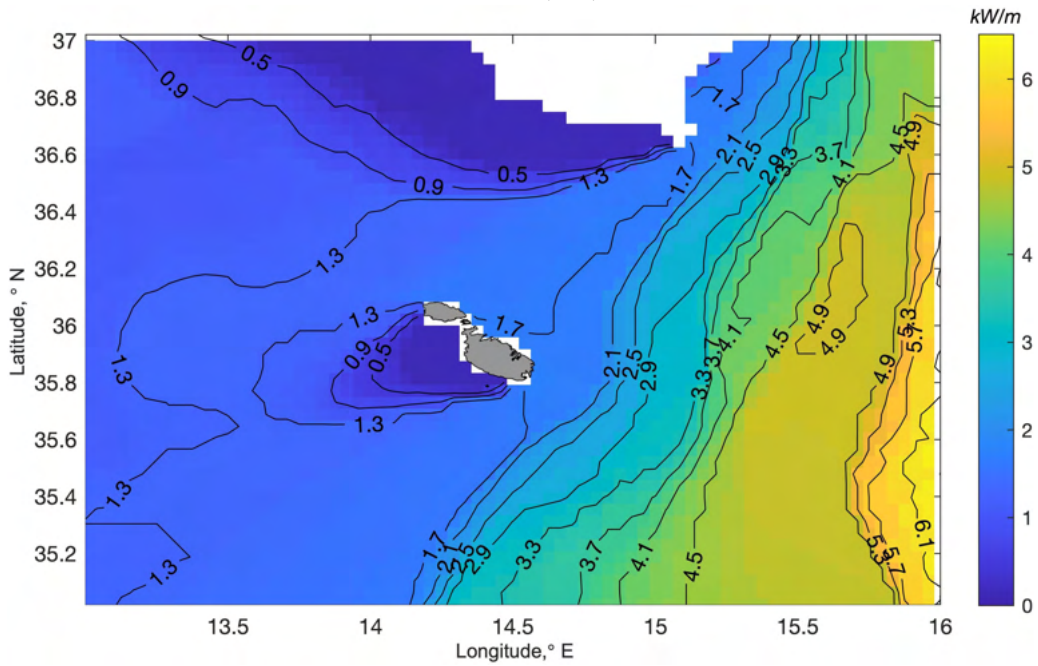
(B) *24 hour window: 20/11/2021*

FIGURE 5.55: *Power plot of the re-analysis data from the Copernicus model on 20/11/2021*

isolines are shifted slightly Eastwards, resulting in higher power values as one progresses Westwards when compared to the forecast data. The shadow
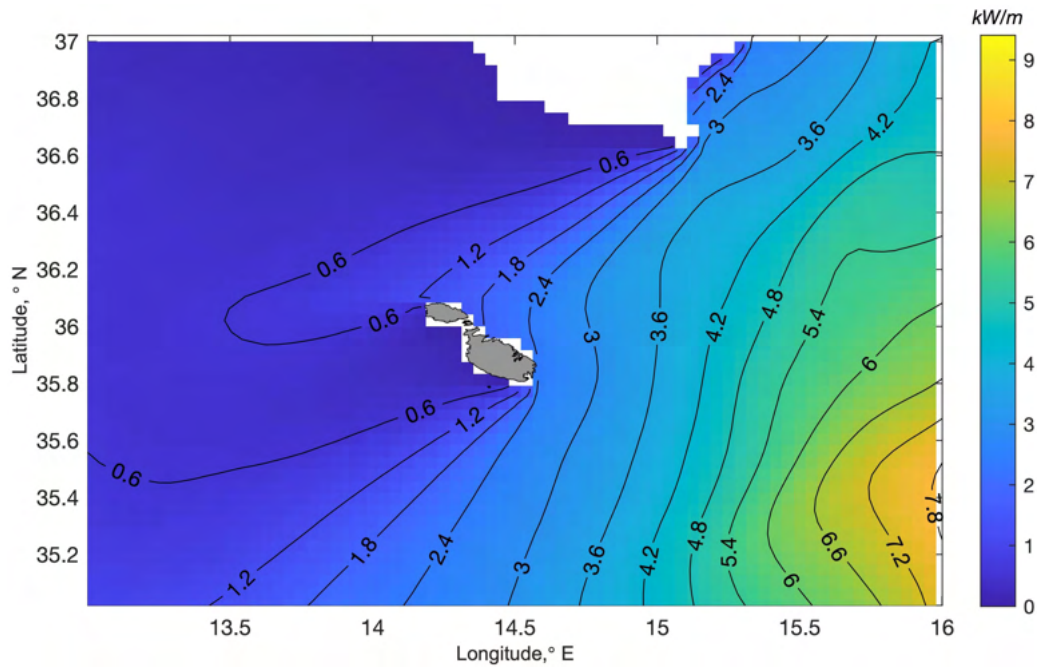
(A) *1 hour window: 20/11/2021 14:00:00*
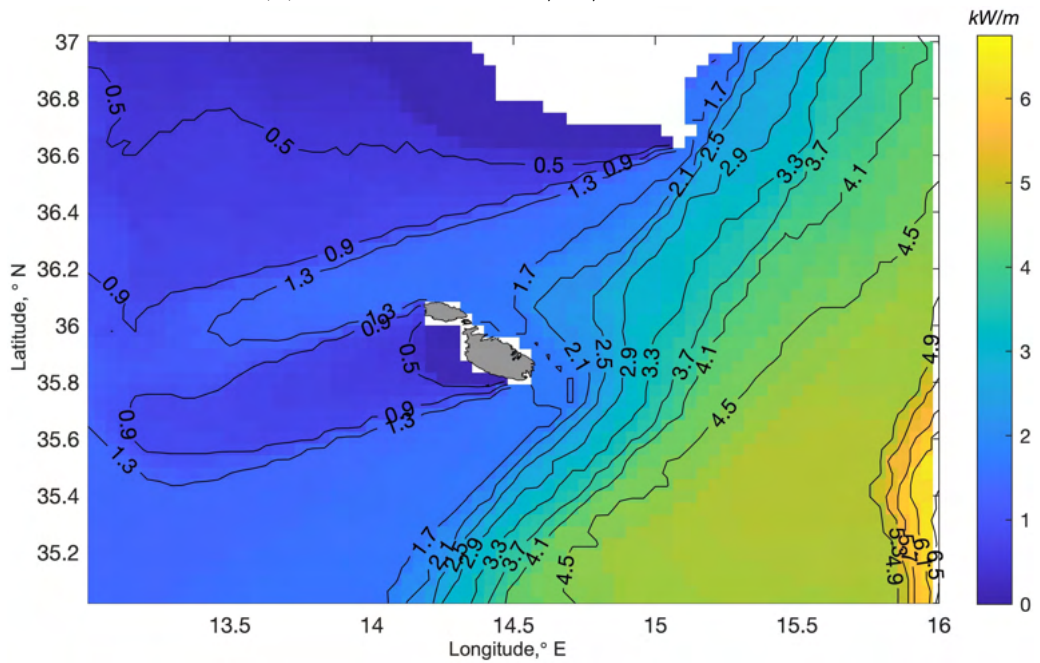
(B) *24 hour window: 20/11/2021*

FIGURE 5.56: *Power plot of the forecast data from the Copernicus model on 20/11/2021*

of lower power in the forecast case. extends further than that in the hindcast case, as can be noted from the 0.6 kW / m isoline.

154

It can then be noted than the day-averaged and hourly forecast both give quite a good approximation to the hindcast data. This indicates that the forecasts on both a low and high time resolution (1hr and 24hrs) can produce reliable wave power forecasts.

One year averaged data

Considering an averaging window over a longer period of time allows for a better estimation of the yearly wave power climate. Here, Copernicus model data between 04/08/2020 08:00 and 12/07/2021 06:00 is considered for the calculation. Naturally, having several years of data as opposed to one provides a better statistical representation of the power distribution. For the purposes of this work, however, a year is sufficient to illustrate typical power values. The average H_s and T_E variable maps are plotted, Figures 5.57 and 5.58, respectively, in order to illustrate the average sea state that results in the wave power map plot which is given in Figure 5.59.

The H_s and T_E plots are here described. Looking first at Figure 5.57, it is quickly notable that the average SWH over a year is relatively low, with offshore values reaching values around ~ 1.2 m at most. For the case of the energy period T_E, Figure 5.58, the average offshore energy period over a year reach values around ~ 5.4 s at most. The area beyond the West coast of Malta seems to have a slightly lower energy period values when compared to those beyond the East coast. These average values are consistent with the global mean H_s and T_E maps presented by Martinez and Iglesias in [103], for the region under consideration.

When the power values obtained in this Figure are compared to those obtained by Drago et al [9], for a smaller region using a SWAN model over a five-year period, these are found to be consistent. According to the work
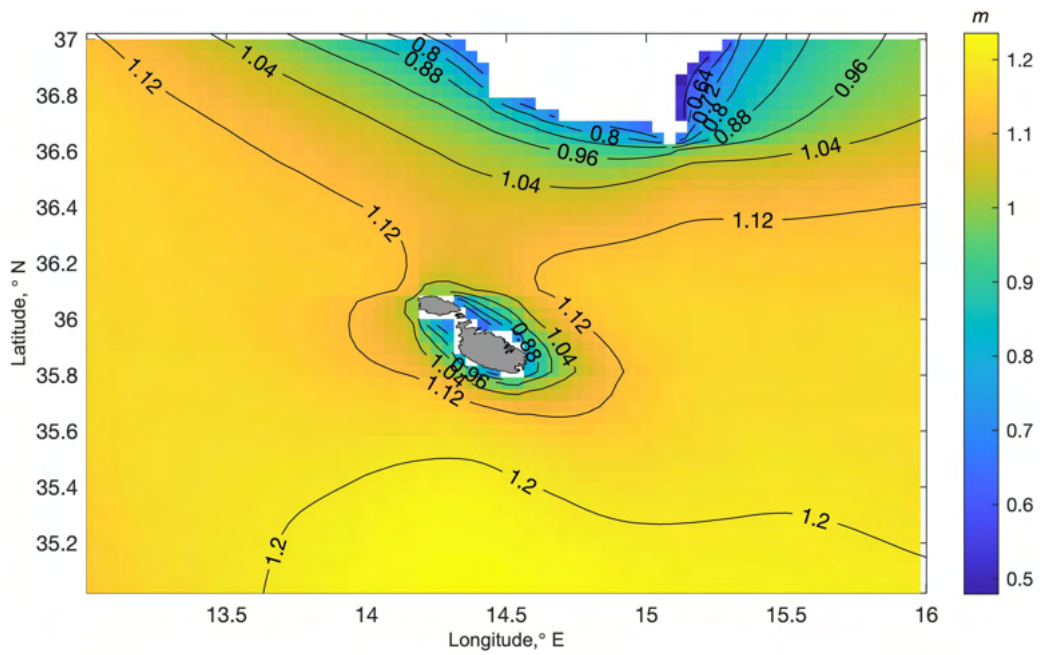
FIGURE 5.57: H_s plot of the re-analysis data from the Copernicus model between 04/08/2020 08:00 and 12/07/2021 06:00
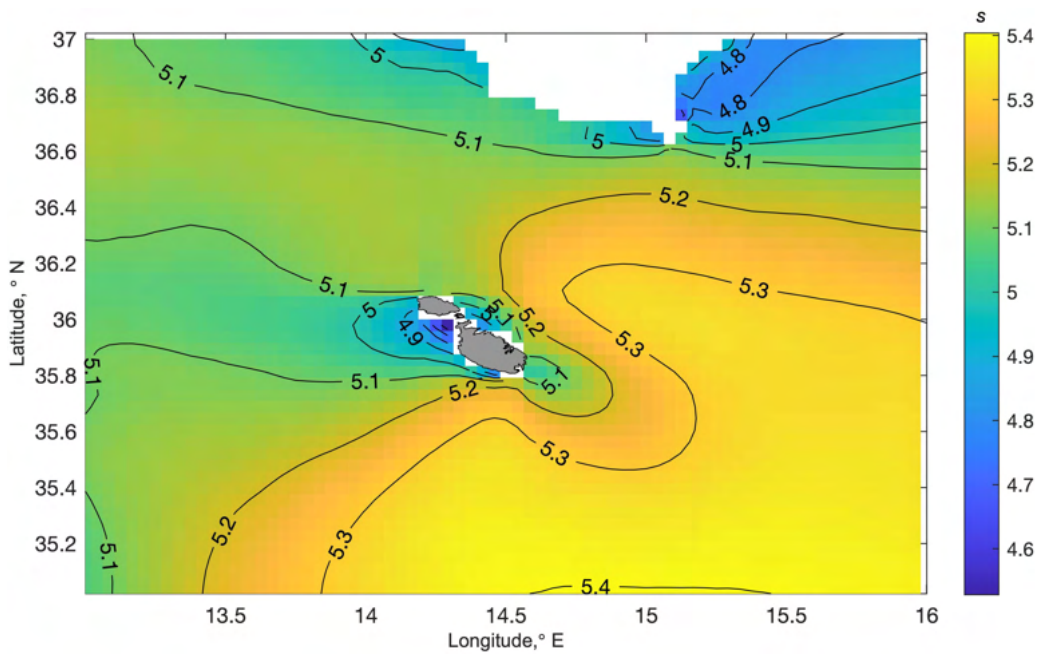
FIGURE 5.58: T_E plot of the re-analysis data from the Copernicus model between 04/08/2020 08:00 and 12/07/2021 06:00
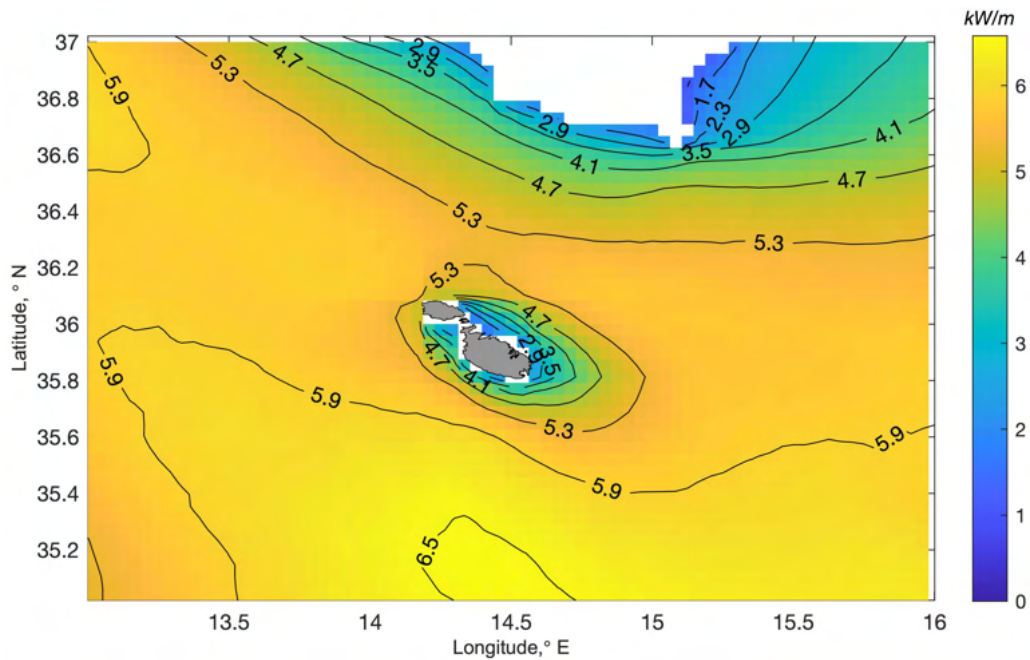
FIGURE 5.59: *Power plot of the re-analysis data from the Copernicus model between 04/08/2020 08:00 and 12/07/2021 06:00*

done by Martinez and Iglesias [103], in an investigation of global wave power exploitability, the region under consideration here is classified as Class I by the wave resource classes. This class, defined by regions of power less than 10 kW/m, is the lowest of the classes, and is indicative of poor wave energy resource. The average H_s and T_E described in the previous paragraph are also consistent with the ranges typically associated with Class I areas; $H_s < 2$m and $1.7 < T_E < 12.6$ s. In contrast to this, regions in the Northern part of Europe have classifications up to Class IV, which are regions with power in the range 40-80 kW/m [103].

5.5.3 ROSARIOSWAN Map

In this Section, power maps from the best 24hr wave forecast have been plotted for the ROSARIOSWAN dataset, that described in Section 4.1.2, using the process described in Section 3.3.1. The plots presented here are the
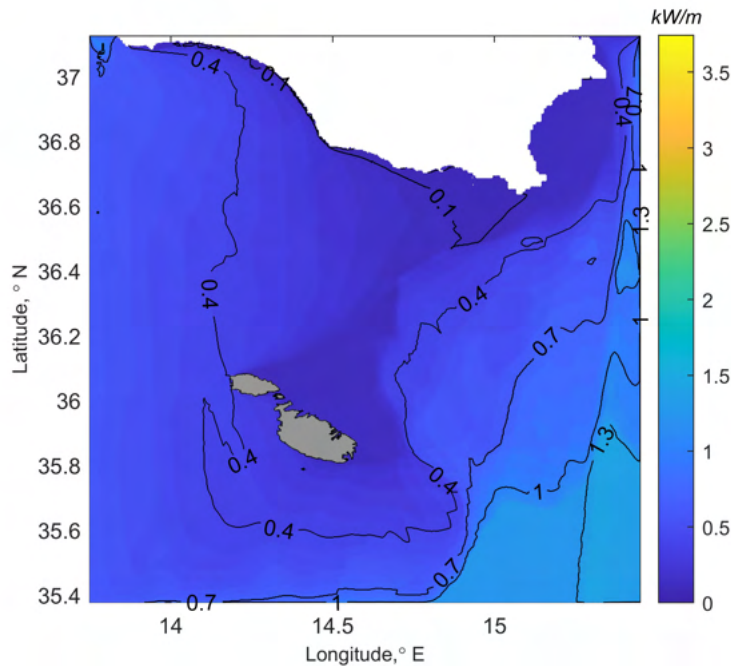
FIGURE 5.60: *Power plot of the forecast data from the ROSARIOSWAN model for 09/09/2021*

resulting power plots for two time averaging windows, 24hr and 1hr. It can be immediately noted, from these plots, that these are of higher resolution than those in the Copernicus model case; despite the fact that the area covered by the ROSARIOSWAN model is smaller than that considered in this work for the Copernicus model case, the processing of ROSARIOSWAN data takes longer because of its much higher resolution. One 24hr averaged window plot is given in Figure 5.60 and one 1hr averaged plot is given in Figure 5.61.

What can be noted from the hourly-averaged plot for 13:00 on 09/09/2021, Figure 5.61, is that a 'shadow' of lower power is formed towards South-West beyond coasts of Malta and Sicily, in this time-period. In contrast, in the day-averaged plot for the same day, Figure 5.60, the lower-power shadow is estabished more towards a North-Eastern direction for Malta, and an Eastern direction for Sicily. Both plots have higher power values in the
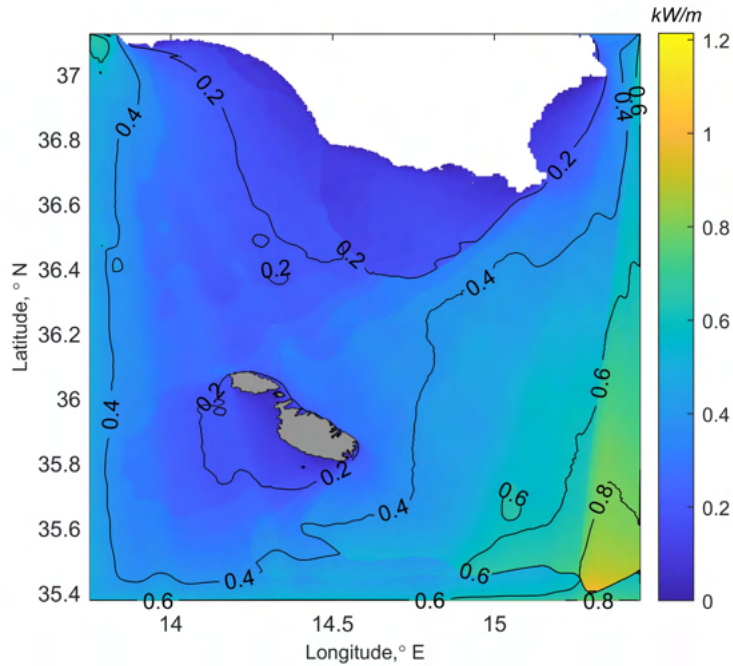
FIGURE 5.61: *Power plot of the forecast data from the ROSARIOSWAN model for 09/09/2021 13:00*

bottom-right area of the plots.

5.6 Variability

The variability of the power resource is an important factor to consider when investigating the wave resource, especially for the application of WEC technologies. In this Section, the variability measures described in Section 3.3.2 are calculated at the buoy point for the different data sources available, as well as over the whole region of Copernicus model data under consideration.

5.6.1   At buoy position

The resulting calculated values for the variability measures for the buoy, Copernicus Model, ROSARIOSWAN Skiron and ROSARIOSWAN Maria model data are summerised in Table 5.16.

Table 5.16: *Variability measures, COV, SV and MV, at buoy position*

Data	COV	SV	MV
Buoy	1.5986	1.1305	1.6722
Copernicus Model	1.9166	1.6817	2.4785
ROSARIOSWAN Skiron Model	2.3198	1.8470	2.8074
ROSARIOSWAN Maria Model	2.1148	1.9318	3.4689

For all measures, the variability is overestimated when compared to the results from the buoy data, with the ROSARIOSWAN Maria Model having the greatest difference, except for the COV case, and the Copernicus Model the least. According to the discussion in Section 3.3.2, based on the COV measure, the area can be considered to have high variability since COV> 1.2 in all cases.

Based on the work of Cornett [86], who defined the SV and MV and carried out a global assessment, the values obtained here for SV and MV can be analysed. Considering first SV, in the case of the buoy result, this value is slightly higher than what is expected in coastal areas at similar latitudes. For the higher values of SV, these are comparable to the non-coastal areas of similar latitudes.

Similarly, for the case of MV, the buoy result is higher, by an increased amount in this case, than what is expected at similar latitudes at coastal areas. The value of MV for the case of Copernicus model data is comparable to non-coastal areas. The value of MV from both the ROASRIOSWAN models is quite high and is attributed to select areas on the global scale of

high variability.

It should be noted that the variability in the Mediterranean region is not covered by the global analysis by Cornett. The area might then actually be one of higher variability than that of the open ocean due to it being closed off. This is infact confirmed in the work by Martinez and Iglesias [103], who carried out investigations into the exploitability of the global wave resource. In this aforementioned work, a plot of the COV did include the Mediterranean region, which showed a comparably higher variation than non-enclosed spaces. This variation supports then the higher values obtained in the calculation of the COV.

5.6.2   Map

As done for the single point case in Section 5.6.1, the process is repeated here for the entire Copernicus model domain under consideration, and the resulting variability measures of COV, SV and MV are plotted in maps in Figures 5.62, 5.63 and 5.64, respectively.

What can be noted over the whole region from these plots is that, for each measure, the differences from one point to another are not very dramatic. The changes are quite gradual and consistent with no specific region having particularly high or low values. From the COV and MV maps, Figures 5.62 and 5.64, respectively, it can be noted that the region West of Malta has higher variation than the region East of Malta. In the case of MV, this effect is more prominent closer to the islands' coasts. Although in the seasonal case, Figure 5.63, this effect isn't evident on a regional scale, it is closer to the coast, with the West coast experiencing more variation than the East.
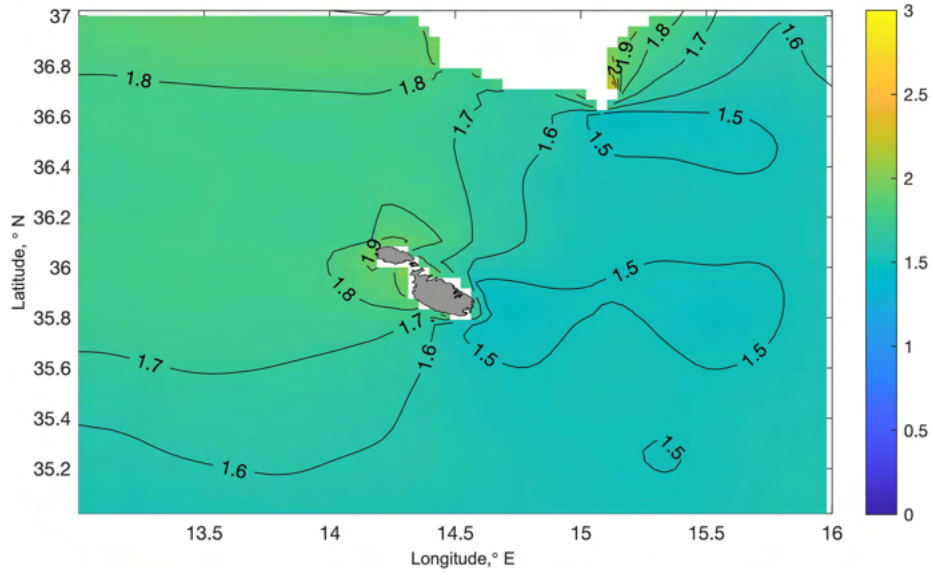
FIGURE 5.62: *Copernicus Model Coefficient of variation between 04/08/2020 08:00 and 12/07/2021 06:00*
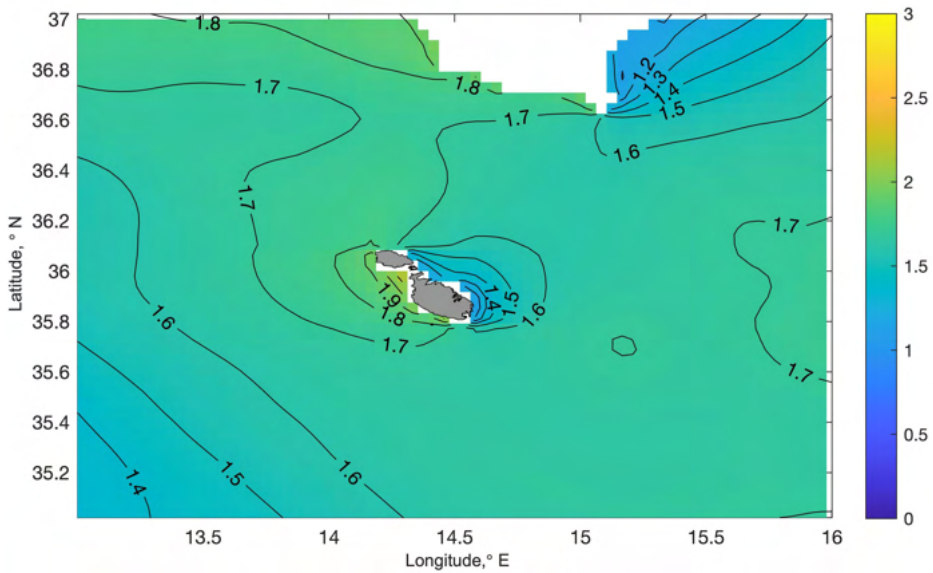
FIGURE 5.63: *Copernicus Model Seasonal Variation between 04/08/2020 08:00 and 12/07/2021 06:00*
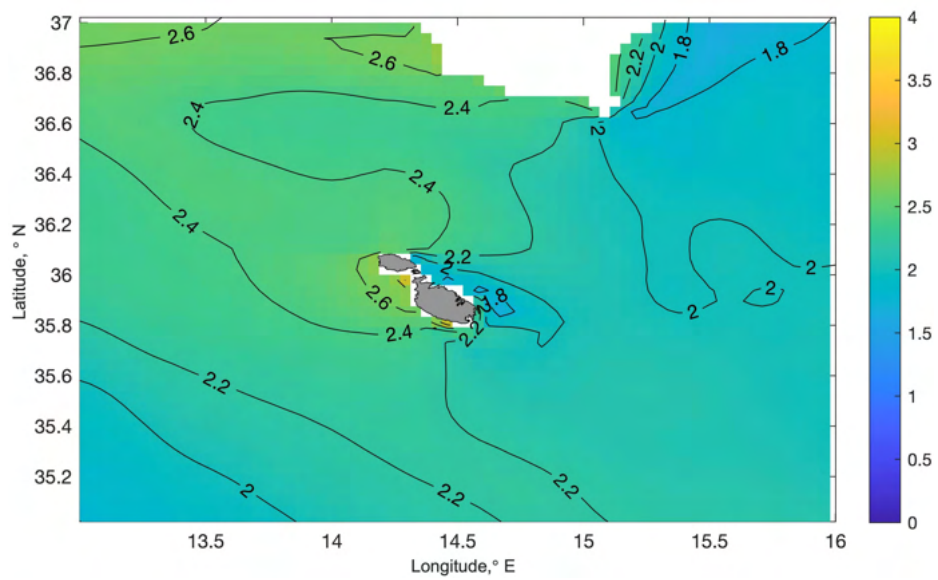
Figure 5.64: *Copernicus Model Monthly Variation between 04/08/2020 08:00 and 12/07/2021 06:00*

5.7   Wave Energy Converters Output Power

Having a means now to characterise the wave power and sea state, here we present the respective output power from different types of WECs based on these considerations. Similar to the calculations carried out for the wave power in Section 5.5, the WEC output power is first calculated over a one-year period, between 04/08/2020 and 12/07/2021, near the position of the buoy for the datasets of the buoy, Copernicus Model, ROSARIOSWAN Maria and ROSARIOSWAN Skiron in order to compare the outputs by using the method described in Section 3.3.3.

Again, it is helpful to be able to visualise the power output that each WEC has to offer over the region under consideration for ease of comparison between different areas and WEC type. It is also useful to use this visualisation with forecast model data, such that the output power in the sea waves can be anticipated ahead of time. Such forecast data can then be compared to hindcast analysis data, resulting in an indicator of how good the prediction is.

The output WEC power maps of the spatial domain under consideration are then found by using the same method describe in Section 3.3.3 for every single point. The use of either T_E or T_p as one of the binning dimensions depends on how the power matrix of the WEC under consideration is defined. In this case, the WECs under consideration are those listed in Table 2.1, where Pelamis, Wave Dragon, and Wavestar's power matrices are defined by T_E rather than T_p.

5.7.1 At buoy position

Here presented are the WEC outputs for the buoy position. These are sum-
marised in Table 5.17 and plotted in Figure 5.65. In addition, the capacity
factors, based on these annual output power values and the rated power
given in Table 2.1, are given in Table 5.18.

TABLE 5.17: *WEC annual average output power (kW) based on the period
04/08/2020 - 12/07/2021 for different data sources*

WEC	Buoy	Copernicus Model	ROSARIOSWAN Maria	ROSARIOSWAN Skiron
Aquabuoy	24.5	30.0	24.9	21.6
Archimedes	51.1	64.4	39.8	30.4
CECO	11.7	13.3	12.5	10.1
OEbuoy	68.2	83.0	49.4	44.7
Pelamis	67.3	88.4	88.0	68.7
SeaPower	88.0	103.3	59.0	52.3
Wave Dragon	812.6	910.5	657.9	588.2
Wavebob	61.0	75.8	46.5	39.2
Wavestar C6	192.7	213.9	195.2	175.5

TABLE 5.18: *WEC annual capacity factor (%) based on the period
04/08/2020 - 12/07/2021 for different data sources*

WEC	Buoy	Copernicus Model	ROSARIOSWAN Maria	ROSARIOSWAN Skiron
Aquabuoy	9.8	12.0	10.0	8.7
Archimedes	2.0	2.6	1.6	1.2
CECO	1.7	1.9	1.8	1.5
OEbuoy	2.4	2.9	1.7	1.6
Pelamis	9.0	11.8	11.7	9.2
SeaPower	2.5	2.9	1.6	1.5
Wave Dragon	13.8	15.4	11.2	10.0
Wavebob	6.1	7.6	4.7	3.9
Wavestar C6	32.1	35.6	32.5	29.3

Looking at Figure 5.65, it can be observed that all datasets generally fol-
low a similar pattern for the WEC output power, indicating that the re-
sulting values from different datasets are consistent. When compared to
the buoy results, the Copernicus model seems to overestimate the output
power, while the ROSARIOSWAN models underestimate it. In particular,
the ROASRIOSWAN Skiron model understimates the output more that the
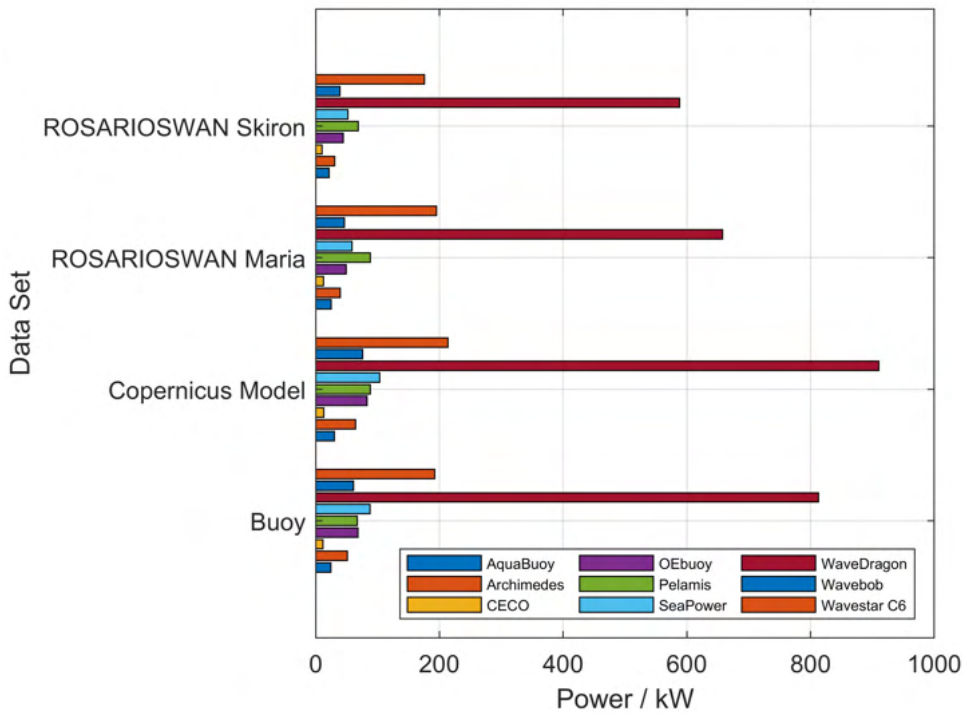
FIGURE 5.65: *WEC annual average output power (kW) based on the period 04/08/2020 - 12/07/2021 for different data sources*

ROASRIOSWAN Maria model. This underestimation of the power from the ROSARIOSWAN model data is again likely to be a result of the underestimation of the SWH and peak period parameters by the model itself as discussed in Sections 5.1.2 and 5.1.3.

The absolute difference between the buoy measurement and model WEC output power, represented as a percentage of the buoy result, can be calculated to quantify the difference in each model case. For the Copernicus model, the largest absolute difference (31.3%) is associated with the WEC Pelamis, for ROSARIOSWAN Maria (33.0%) with SeaPower and for ROSARIOSWAN Skiron (40.5%) with SeaPower.

Based on the buoy output, it can be clearly observed that the WEC that seems to have the highest output power is the WaveDragon at 812.6 kW, and

the least output power is supplied by CECO at 11.7 kW. The second highest output is produced by the Wavestar C6, which is still higher than the rest of the power outputs as it is outputs 192.7 kW. The second lowest power output is given by the AquaBuoy with an output of 24.5 kW. The other six WEC output powers fall between 50 and 90 kW and so represent more intermediary output powers. In order to better understand the variability of the outputs between the models, the difference between the maximum and minimum values for a given WEC is presented as a percentage of the buoy output power in Table 5.19. From this Table it can be inferred that the largest variation in output power exists in the Archimedes outputs (66.5%), and the smallest variation in the Wavestar C6 (19.9%). This means that the calculation of output power of a WEC is affected by which dataset is being used to calculate it. This is understandable as the different models will produce different combinations of H_s and T_E/T_p which will result in differing histograms of these two values, which will in turn affect the result when multiplying with the power matrix of a WEC.

TABLE 5.19: *WEC output power percentage difference between maximum and minimum output values from models as compared to the power output resulting from buoy measurement data*

Data	% difference
Aquabuoy	34.2
Archimedes	66.5
CECO	27.4
OEbuoy	56.1
Pelamis	29.3
SeaPower	58.0
Wave Dragon	39.7
Wavebob	59.9
Wavestar C6	19.9

Looking at the capacity factors in Table 5.18, the WECs can be broadly grouped. On one end, the worst capacity factors belong to the Archimedes,

167

CECO, OEbuoy and SeaPower WECs, with values at around 2%. On the other end, the highest capacity factor is for the Wavestar C6 WEC at 32.1%, which is followed by WaveDragon at 13.8%. Aquabuoy, Pelamis and Wavebob then lie in intermediary values between these two extremes. It would seem then that the Wavestar C6 outputs more power than most WECs, apart from WaveDragon, while also having the highest capacity factor.

5.7.2   Using Copernicus Model Map

Forecast and Hindcast analysis

For the purpose of comparison between resulting output power of a WEC for forecast and hindcast analysis Copernicus model data, only a couple of WEC types are considered here rather than all of the nine devices, as this is an analysis of the accuracy of the forecast rather than of the specific WEC output at the time range considered. The averaging period in this case is over a nine-day period over which the forecast was available; the range corresponds to 19/11/2021 12:00 - 28/11/2021 11:00. The two WECs considered were the SeaPower and the WaveDragon; the resulting plots are given in Figures 5.66 and 5.67, respectively. In these plots, apart from the WEC output power plots for the forecast and hindcast data, the difference between the two is also plotted.

For this particular time period, it seems that in both WEC cases the Copernicus model forecast underestimates the output power from the WEC. Indeed, the difference for both, Figures 5.66c and 5.67c, are positive values. Based on the discussion in Section 5.7.1 regarding the output WEC power at the buoy point, the Copernicus model in that case showed a tendency to overestimate the output power when compared to the results from the buoy measurements, where in that case the model was using hindcast analysis
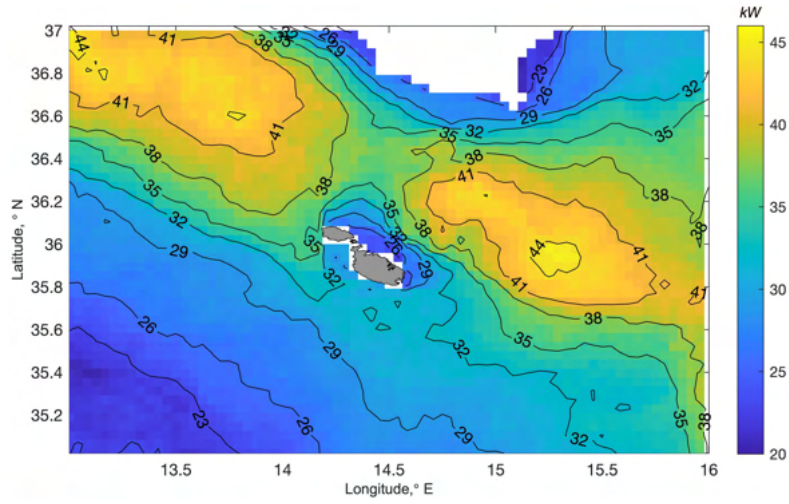
(A) *Forecast*
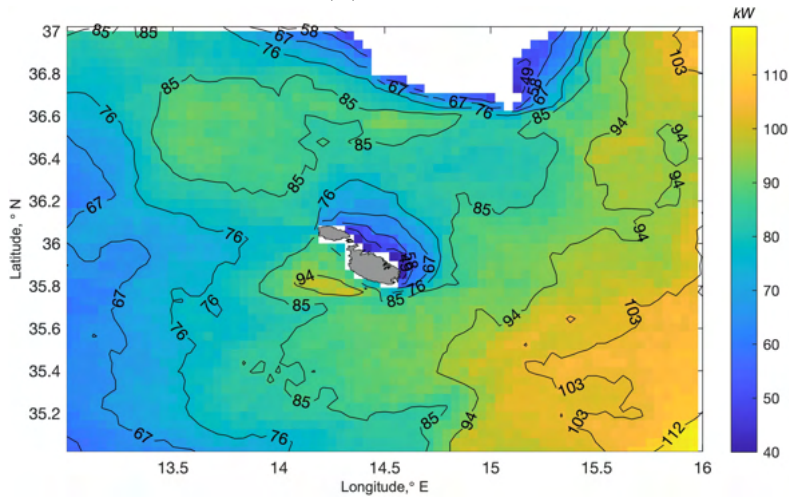
(B) *Re-analysis*
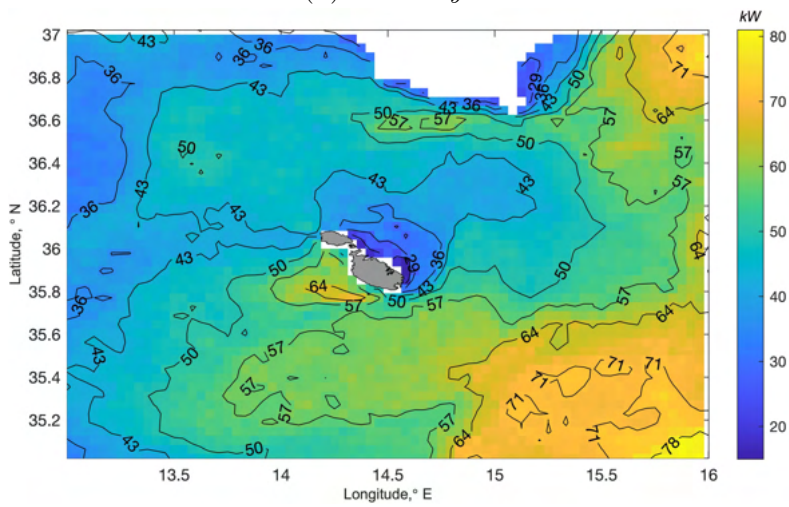
(C) *Difference*

Figure 5.66: *SeaPower output power plot using data from the Copernicus model between 19/11/2021 12:00 and 28/11/2021 11:00*
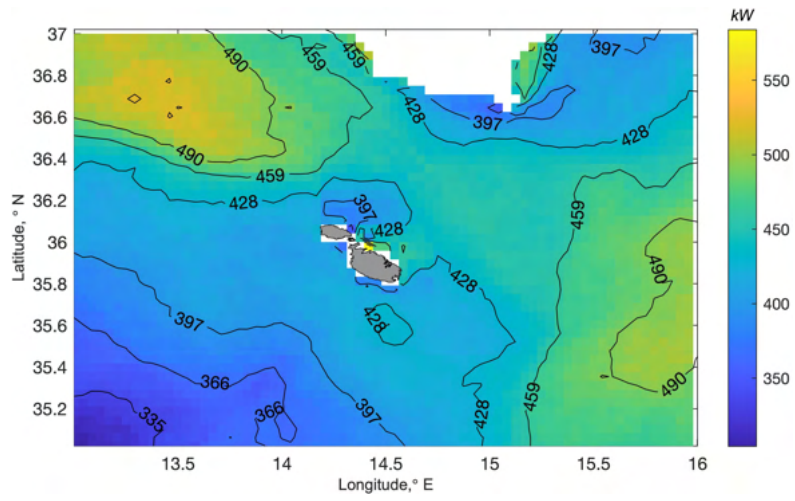
(A) *Forecast*
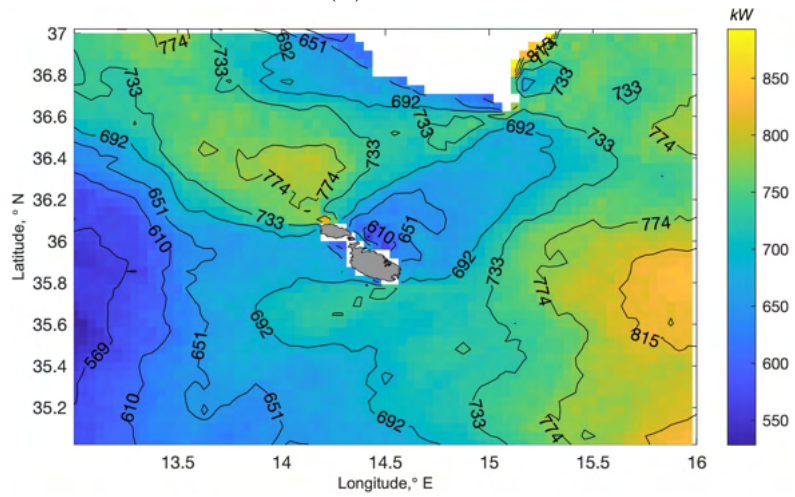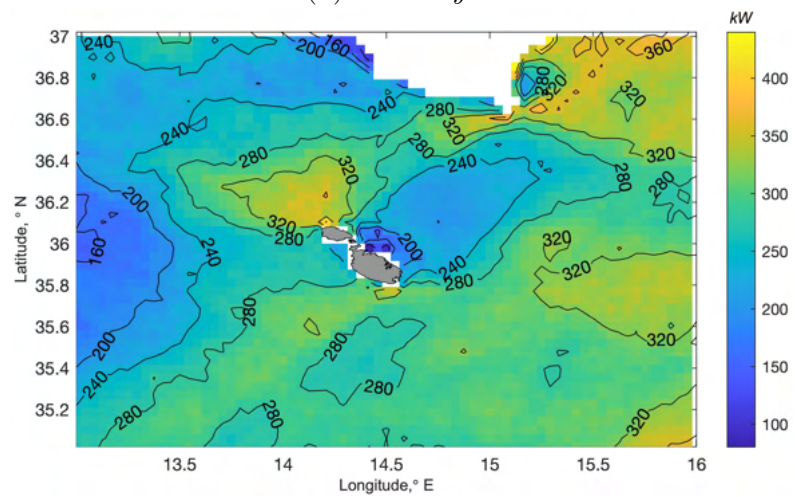
(B) *Re-analysis*

(C) *Difference*

FIGURE 5.67: *WaveDragon output power plot using data from the Copernicus model between 19/11/2021 12:00 and 28/11/2021 11:00*
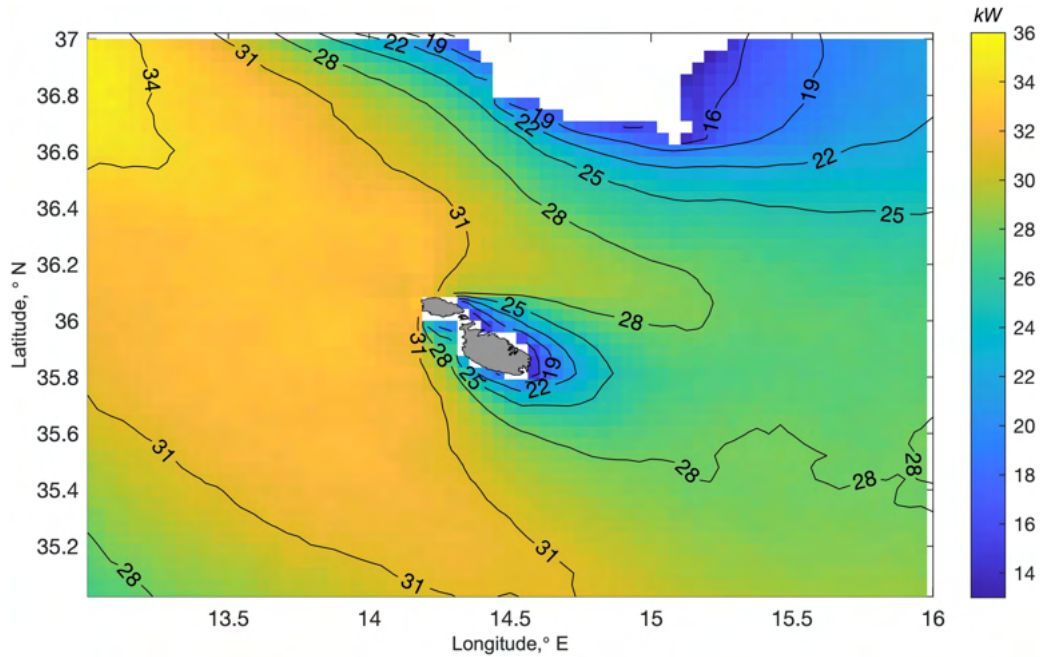
FIGURE 5.68: *AquaBuoy output power plot using re-analysis data from the Copernicus model between 04/08/2020 08:00 and 12/07/2021 06:00*

data. Considering this then, it can't be said whether the forecast would likely be underestimating or overestimating the WEC output power as this could possibly be fluctuating between the two.

One year averaged data

Considering an averaging window over the whole year period for the entire Copernicus region considered yields a better estimation of the yearly output wave power of the WEC under consideration; the Copernicus model data between 04/08/2020 08:00 and 12/07/2021 06:00 is once again used here for the calculation. The resulting plots for the nine WECs considered in this work are given in Figures 5.68-5.76.

What can be said for all of these plots is that the power output for all the WECs is higher away from the coastal areas. This coastal lower-power 'shadow' tends to, in all WECs, extend more beyond the Maltese East coast
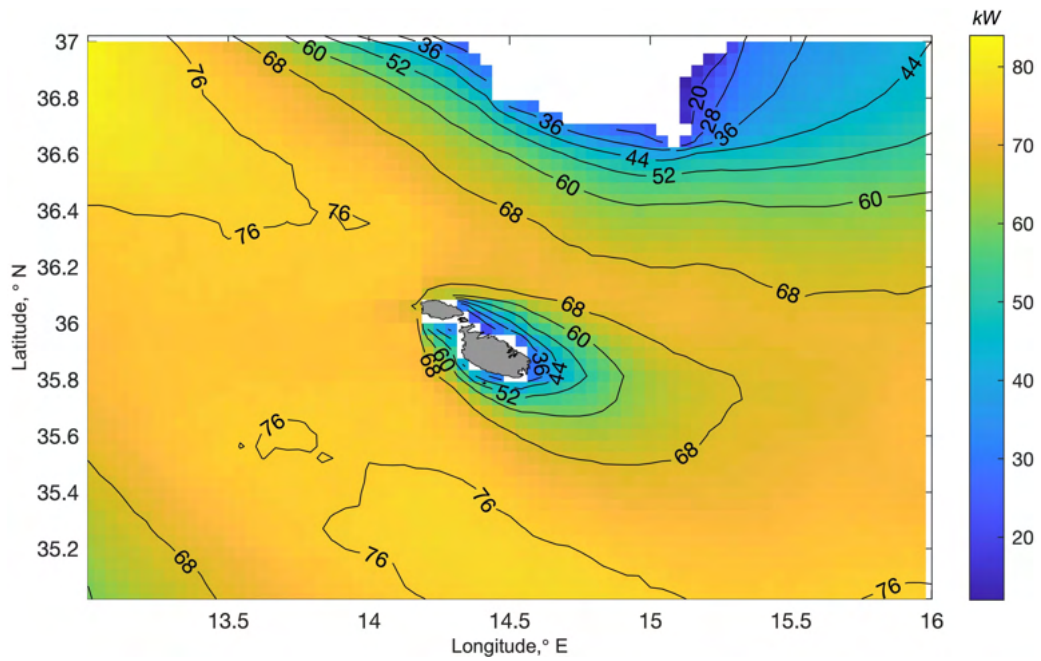
FIGURE 5.69: *Archimedes output power plot using re-analysis data from the Copernicus model between 04/08/2020 08:00 and 12/07/2021 06:00*
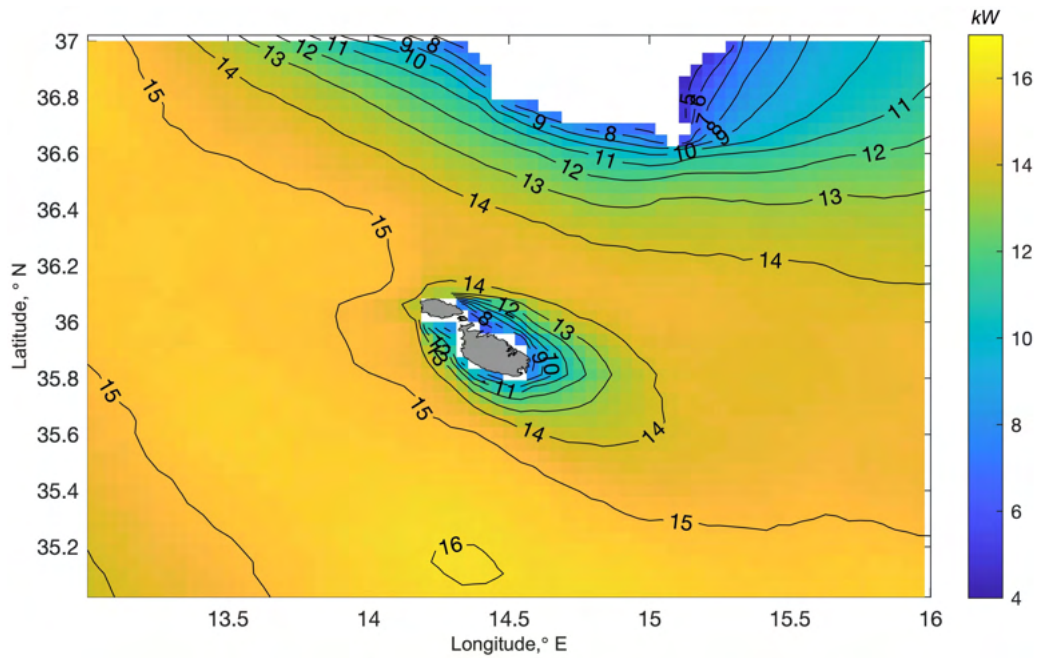
FIGURE 5.70: *CECO output power plot using re-analysis data from the Copernicus model between 04/08/2020 08:00 and 12/07/2021 06:00*

172
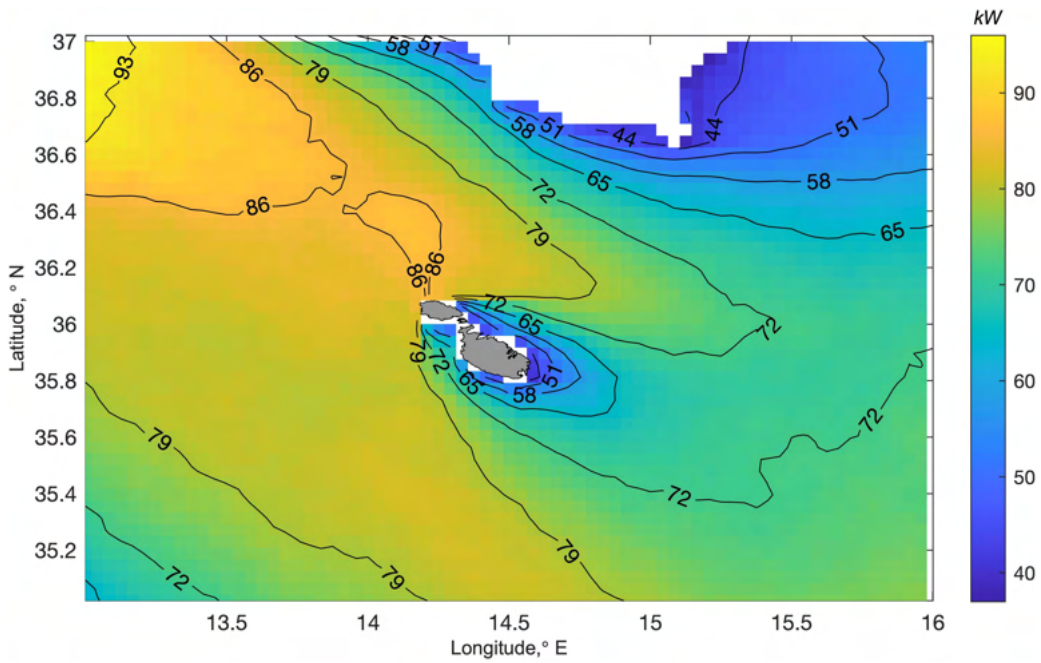
Figure 5.71: *OEbuoy output power plot using re-analysis data from the Copernicus model between 04/08/2020 08:00 and 12/07/2021 06:00*
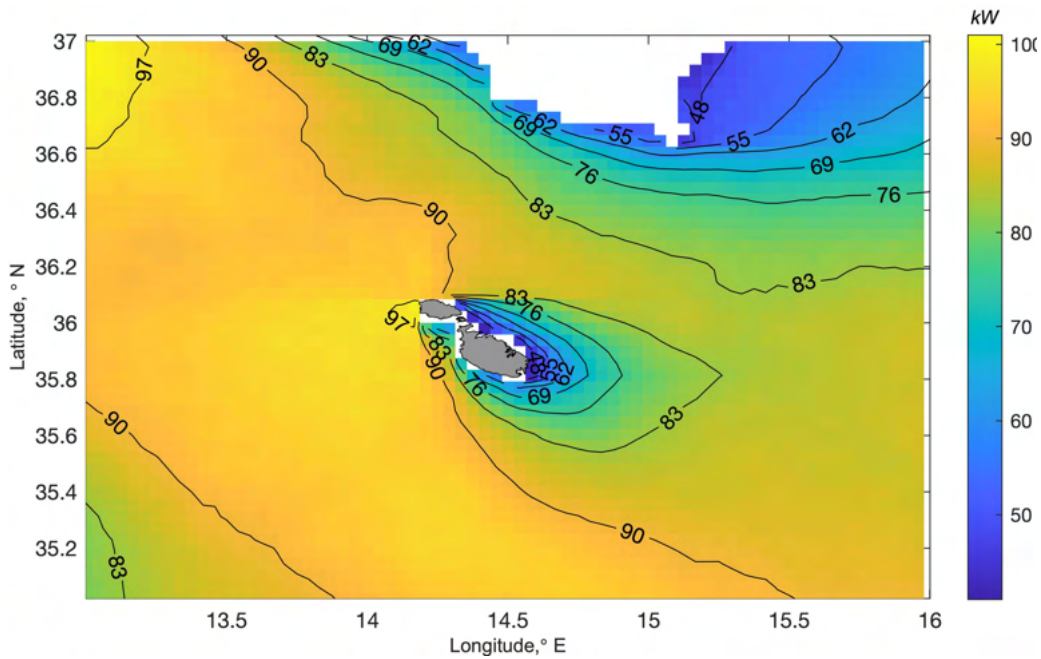
Figure 5.72: *Pelamis output power plot using re-analysis data from the Copernicus model between 04/08/2020 08:00 and 12/07/2021 06:00*

173
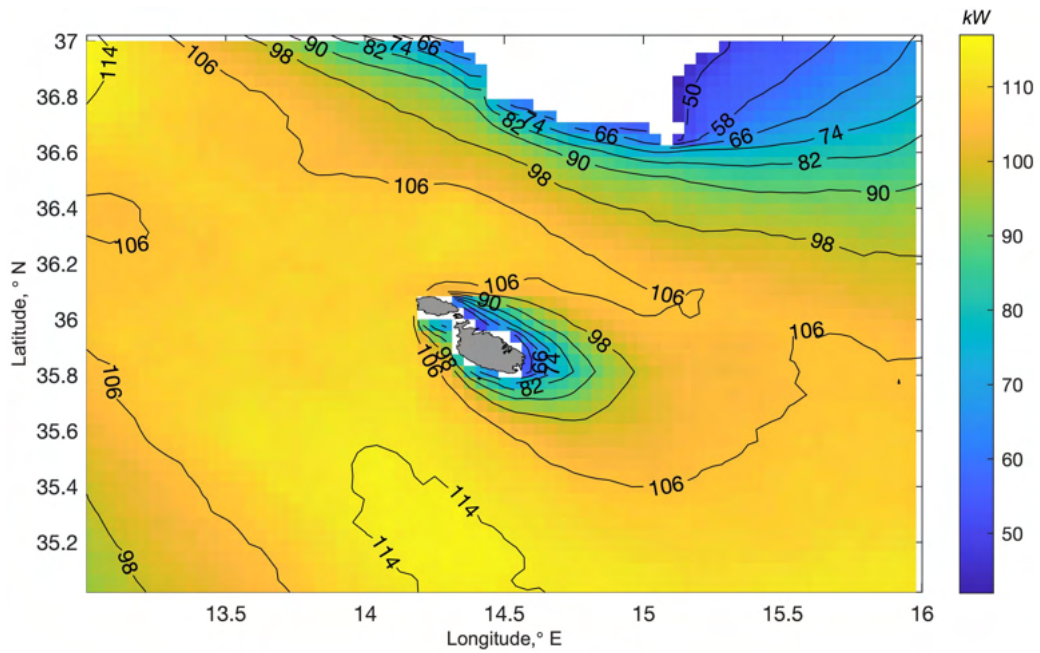
FIGURE 5.73: *SeaPower output power plot using re-analysis data from the Copernicus model between 04/08/2020 08:00 and 12/07/2021 06:00*
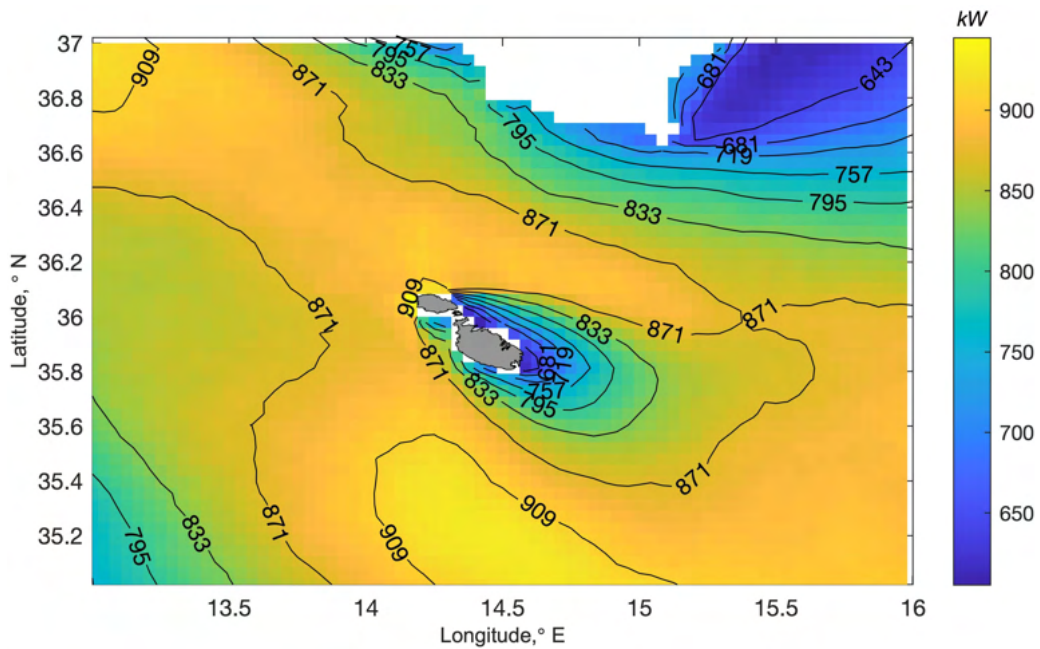
FIGURE 5.74: *WaveDragon output power plot using re-analysis data from the Copernicus model between 04/08/2020 08:00 and 12/07/2021 06:00*
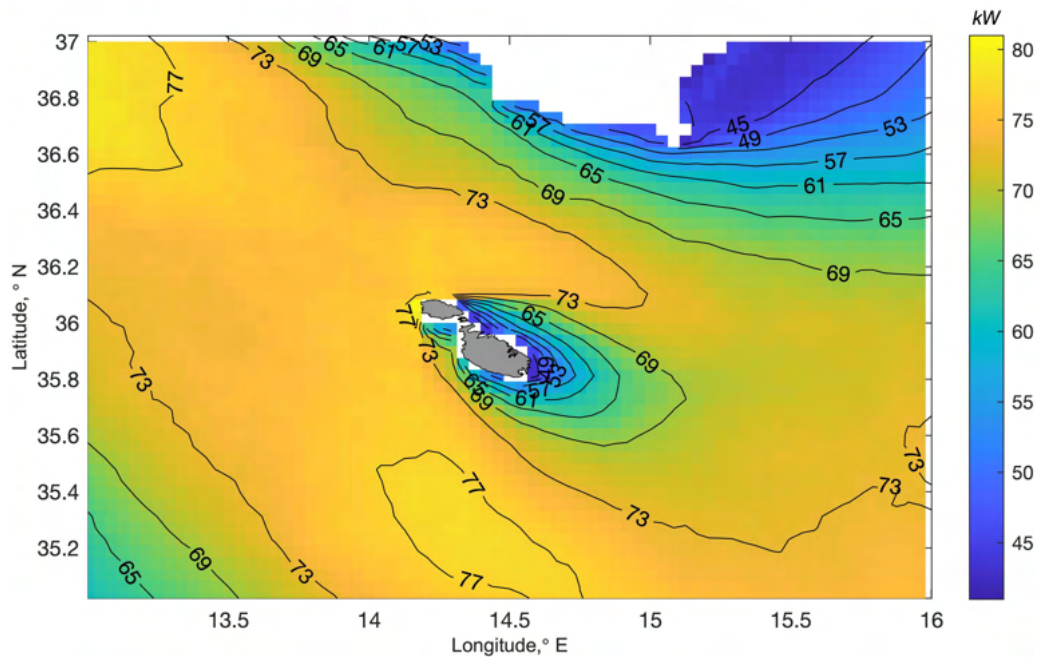
Figure 5.75: *Wavebob output power plot using re-analysis data from the Copernicus model between 04/08/2020 08:00 and 12/07/2021 06:00*
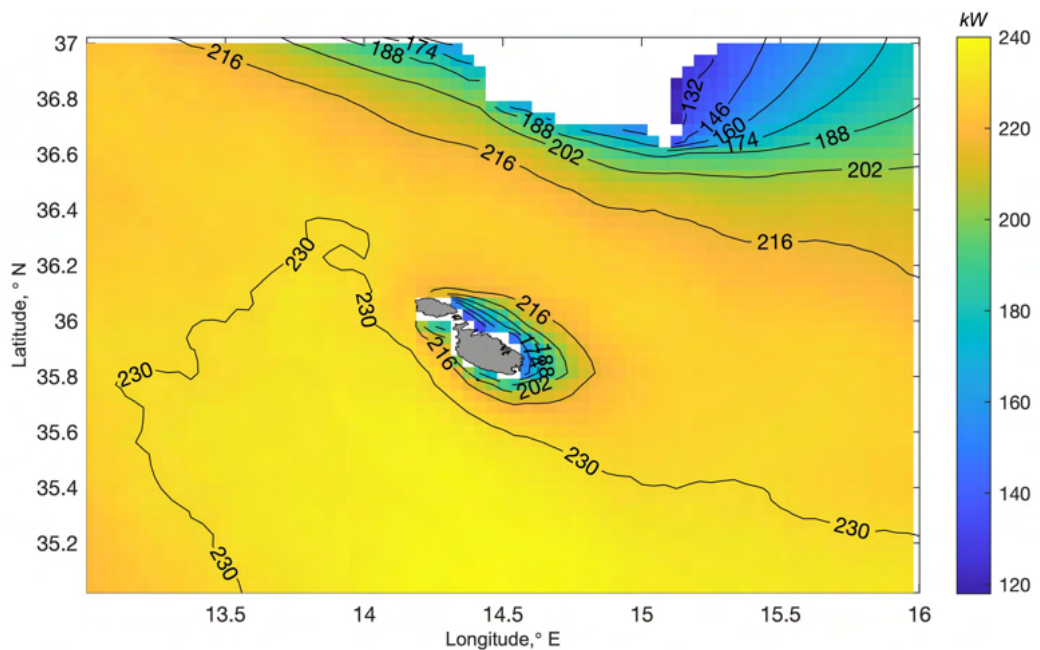
Figure 5.76: *Wavestar C6 output power plot using re-analysis data from the Copernicus model between 04/08/2020 08:00 and 12/07/2021 06:00*

175

rather beyond the West, which is illustrated by the isobars in each plot. The WECs AquaBuoy, OEbuoy, Pelamis and Wavebob (Figures 5.68, 5.71, 5.72 and 5.75, respectively) show a higher power output beyond the West coast when compared to the East coast. The remaining WECs, Archimedes, CECO, SeaPower, WaveDragon and Wavestar C6 (Figures 5.69, 5.70, 5.73, 5.74 and 5.76, respectively), do not show such a strong relative drop in power when comparing the West area to the East area. Rather, in this case, the power output tends to decrease with increasing latitude, granted that the isobars are not horizontal and so, still indicate a slight lower power in the Eastern area when compared to the same latitude in the Western area.

Looking at the power outputs of the WECs, similar to the discussion for the power at the buoy position in Section 5.7.1, the highest output power is produced by the WaveDragon with a regional maximum of about 910 kW, and the least output power is supplied by CECO with a maximum in the region of about 16 kW. The second highest output is produced by the Wavestar C6, which is still higher than the rest of the power outputs as the maximum in the region is around 240 kW. The second lowest power output is given by the AquaBuoy with a maximum in the region of about 36 kW. The other six WEC output powers generally fall between 75 and 110 kW, away from coastal areas, and so represent more intermediary output powers. These aforementioned six WECs' output power can then be considered as the most typical output values in this region.

5.7.3   Using ROSARIOSWAN Model Map

In this Section, only a couple of WEC types are considered rather than all of the nine devices, for the purpose of illustrating differing WEC output in the time range considered for different WECs. The averaging period in
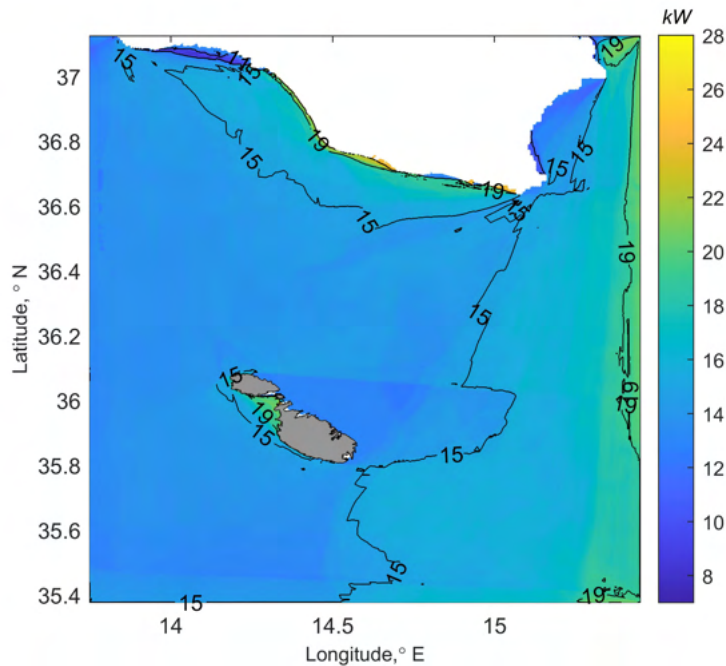
FIGURE 5.77: *SeaPower output power plot using data from the ROSAR-IOSWAN model forecast between 05/09/2021 and 09/09/2021*

this case is over a five-day period from the best 24hr wave forecast; the range corresponds to 05/09/2021 - 09/09/2021. The two WECs considered were the SeaPower and the WaveBob WECs; the resulting plots are given in Figures 5.77 and 5.78, respectively.

From this comparison, it can be clearly seen how different WECs will perform differently in the same sea states. As an example, there are areas in the Wavebob case, Figure 5.78, which have no output. These correspond to sea-states with a combination of H_s and T_p which yield 0 kW in the power matrix of the WEC in question. In the case of the Seapower WEC, Figure 5.77, there are no such areas, indicating that the sea-states favoured production with this WEC in this case. Another notable difference between the two is the variation in output power from the WECs, where the Wavebob experiences a wider variation than the SeaPower case.
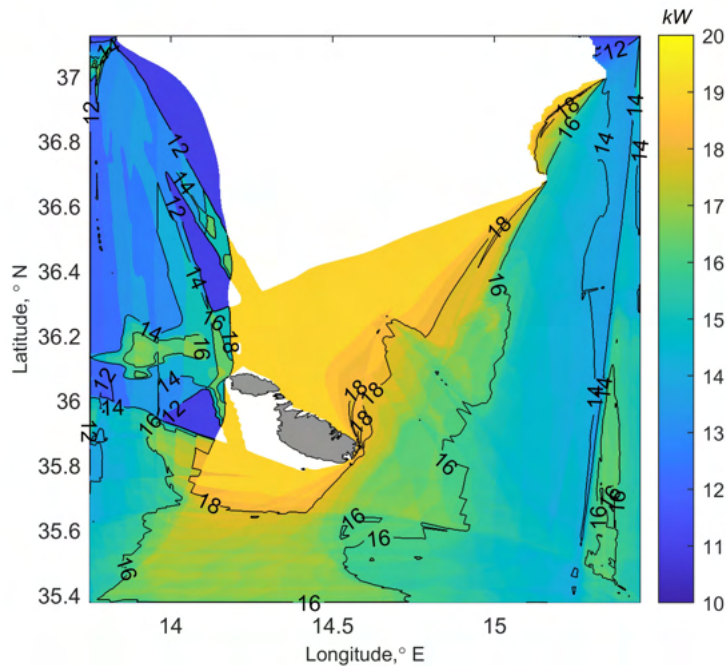
FIGURE 5.78: *Wavebob output power plot using data from the ROSAR-IOSWAN model forecast between 05/09/2021 and 09/09/2021*

5.7.4 Multi Criteria Approach

In this Section, the suitability of the WECs considered in this work is quantified through the modified MCA index, as described in Section 3.3.4, where a number of different factors are taken into consideration. The MCA is carried out for the buoy position data for the same datasets used to obtain the power results described in Section 5.7.1, that is, buoy, Copernicus model, ROSARIOSWAN Maria and ROSARIOSWAN Skiron models.

At buoy position

Here presented are the MCA outputs for the buoy position. These are summarised in Table 5.20 and plotted in Figure 5.79.

Looking at Figure 5.79, it can be observed that all datasets generally follow

TABLE 5.20: *MCA index ($\times 10^4$) based on the period 04/08/2020 - 12/07/2021 for different data sources*

WEC	Buoy	Copernicus Model	ROSARIOSWAN Maria	ROSARIOSWAN Skiron
Aquabuoy	54.96	55.27	13.87	16.60
Archimedes	104.63	112.06	23.72	21.26
CECO	38.58	31.57	10.09	10.52
OEbuoy	135.40	141.68	28.34	31.39
Pelamis	132.58	136.82	46.38	41.32
SeaPower	248.97	217.00	36.43	53.73
Wave Dragon	1830.71	1588.17	451.55	420.96
Wavebob	149.24	149.38	31.50	30.19
Wavestar C6	586.83	546.17	143.46	158.51

a similar pattern for the MCA, indicating that the resulting values from different datasets are relatively consistent. The ranked order of the resulting MCA index is given in Table 5.21 for easy of comparison between the datasets.

TABLE 5.21: *MCA index rank*

WEC	Buoy	Copernicus Model	ROSARIOSWAN Maria	ROSARIOSWAN Skiron
Aquabuoy	8	8	8	8
Archimedes	7	7	7	7
CECO	9	9	9	9
OEbuoy	5	5	6	5
Pelamis	6	6	3	4
SeaPower	3	3	4	3
Wave Dragon	1	1	1	1
Wavebob	4	4	5	6
Wavestar C6	2	2	2	2

In all cases, WaveDragon and Wavestar C6 ranked 1st and 2nd, respectively, and Archimedes, Aquabuoy and CECO ranked 7th, 8th and 9th, respectively. This indicates that, for the extreme MCA indices, the resulting ranks from the different datasets are the same. In the case of the intermediate rankings, the different data sources do not result in the same order; these will be described in the following. SeaPower and OEbuoy were ranked 3rd and 5th, respectively, in all but the ROSARIOSWAN Maria data, in which they were ranked 4th and 6th, respectively. Wavebob and Pelamis were both ranked 4th and 6th, respectively, in the buoy and Copernicus model data. In ROSAR-
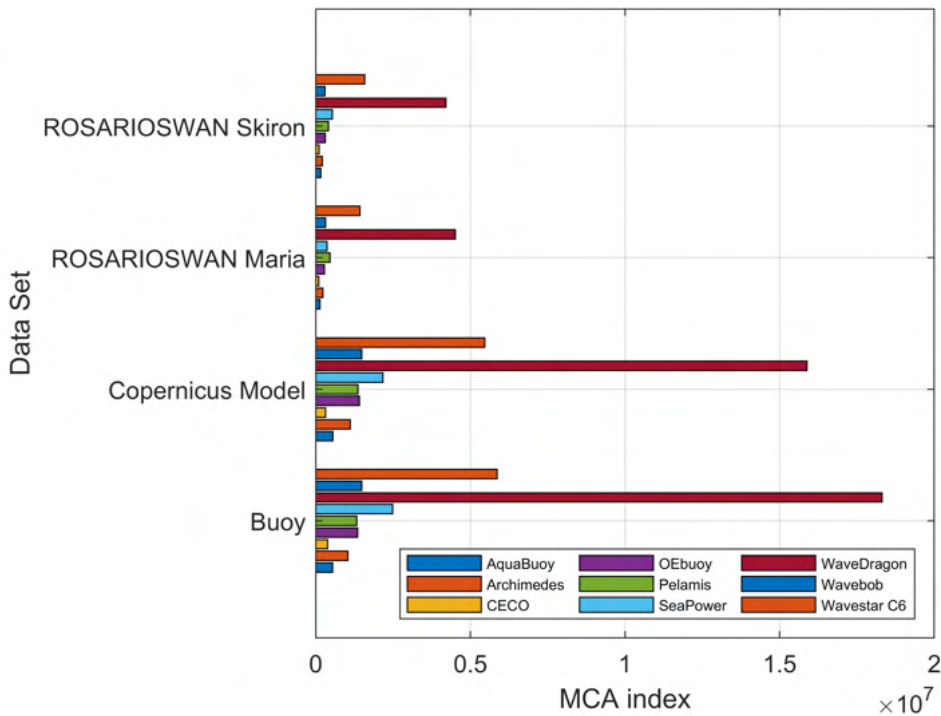
FIGURE 5.79: *MCA index based on the period 04/08/2020 - 12/07/2021 for different data sources*

IOSWAN Maria data, these were ranked 5th and 3rd, respectively, and in ROSARIOSWAN Skiron data, these were ranked 6th and 4th, respectively.

What can also be noted from this comparison is that the Copernicus model rankings are not only identical to the buoy measurement rankings, but that, when considering the actual values of the MCA, Table 5.20, these are very close to each other; this is also visually evident from Figure 5.79. This is not the case for the ROSARIOSWAN model data where, for both cases, the MCA values are all less than 35% of the buoy MCA values. The ROSAR-IOSWAN model data MCA values from both the Maria and Skiron cases are comparable to each other, but less so than the buoy and Copernicus model; indeed, the resulting MCA rankings from the ROSARIOSWAN Maria and Skiron models do not match.

It would seem then, from this analysis, that the extreme MCA values are properly ranked by all models when considering the ranking from the buoy measurements to be the 'true' ranking. Using this same measure, the Copernicus model resulting MCA values and rankings are the best of the three models, with matching rankings and similar index values, whereas the ROSAR-IOSWAN models underestimate the MCA index values and do not have consistent rankings with the respective buoy values.

CHAPTER 6

CONCLUSION

This dissertation has focused on the comparison of different wave datasets in order to establish the performance of models and measurements with respect to each other, including model forecast and hindcast considerations. In addition, calculations of the power potential, variability and WEC output were carried out for the different datasets for comparison and analysis.

The model data from Copernicus showed a better comparison to the buoy data than the ROSARIOSWAN, despite having a model grid of lower resolution. In all cases, the best and worst correlations were seen in the SWH and peak period parameters, respectively. The mean period data displayed a V-like distribution, which results from the underestimation of the parameter by the models for data corresponding to low SWH values (according to buoy data); a similar plot is obtained when comparing HF radar data to the Copernicus model. Such underestimation by the models also occurs for the peak period case. In the ROSARIOSWAN cases, the SWH, mean period, and peak period show a systematic error in the form of an underestimation.

The analyses of the comparison between HF radar data to models and other datasets were limited by the comparatively small dataset available, and so,

more data would be required to make sounder conclusions.

Where datasets were sufficiently large to produce legible scatter plots, plots of the direction parameter showed clustering around the Eastern and North-Western directions, indicating a higher frequency of waves originating from these directions. Scattered 'background' points were also noted in many plots, likely to correspond to lower SWHs, along with weaker clusters of points in the top left and bottom right of the plots.

The comparison of models with each other, Copernicus model and the two ROSARIOSWAN models, showed good correlations in general, with the weaker correlation belonging to the peak period parameter.

The Copernicus model showed very good correlation with the satellite data given that this is this same data which is assimilated with the model for hindcast calculations. Indeed, the correlation between the two datasets improved by 160% from forecast data to hindcast analysis data, with decreases of MAE, RMSE, and SI of 67%, 62%, and 69% respectively.

All the comparisons made are summarised in Table 6.1.

Buoy vs Models	Parameter correlations from strongest to weakest: SWH, direction, mean period, and peak period, for all cases. Both ROSARIOSWAN models resulted in generally similar correlations and error metrics for each parameter, showing no obvious better-performing model. The correlation and error metrics were generally better in most parameters for the Copernicus model case, with the most comparable values with ROSARIOSWAN being achieved for the direction parameter. For ROSARIOSWAN: for all cases but the wave direction, a shift downwards in the distribution of values is observed. For the Copernicus Model: a shift downwards in the distribution of values is observed for the mean period.
Radar vs Models	The most comparable model to radar data was the Copernicus model. The ROSARIOSWAN Maria model outperformed the Skiron version in this case.
Copernicus Model	Parameter correlations from strongest to weakest: Direction, SWH, and mean period. The strongest linear fit, the wave direction, had an associated R^2 of 0.32, which is relatively weak. More data required for better comparison.
ROSARIOSWAN Maria	Parameter correlations from strongest to weakest: Direction, SWH, and mean period. Very limited number of overlapping points for comparison
ROSARIOSWAN Skiron	Parameter correlations from strongest to weakest: SWH, Direction, and mean period. Very limited number of overlapping points for comparison

Models vs Models	
ROSARIOSWAN Maria vs Skiron	Parameter correlations from strongest to weakest: SWH, mean period, peak period, and wave direction. All the R values in this case are > 0.80, indicating strong correlation.
ROSARIOSWAN vs Copernicus	Both ROSARIOSWAN models output similar correlations and error metrics; the Maria version is slightly more comparable to the Copernicus model. Parameter correlations from strongest to weakest: SWH, direction, mean period, and peak period. For all cases but the wave direction, a shift downwards in the distribution of values is observed.
Other	
Satellite vs Copernicus Model	Very high correlation, $R = 0.97$, when hindcast data is used and compared with satellite data since the model is assimilated with this same data. The correlation coefficient increased by 157% from using forecast model data to hindcast model data.
Buoy vs Satellite	One data point of SWH available: Satellite = 2.2590 m and Buoy = 2.3800 m. Comparable but limited data points for comparison.
Radar vs Satellite	One data point of SWH available: Satellite = 1.3910 m and Buoy = 0.6050 m. Not very comparable but limited data points for comparison.
Buoy vs Radar	Only 0.6% of the buoy dataset could be compared. Very ill-fitting linear regression results.

TABLE 6.1: *Summary of dataset comparison results*

185

In the power potential calculations, the Copernicus model and ROSAR-IOSWAN models overestimate and underestimate the power potential, respectively, when compared to the buoy output, with ROSARIOSWAN Skiron having the closest value. The ROSARIOSWAN models are expected to underestimate the power due to its underestimation of the wave parameters. The directional histograms of the output power are generally agreeable between datasets, with a tendency to overestimate the portion of events with power ≤ 1 kW/m, with peaks at the East and North-West directions and low occurrence between the South-East and West directions.

As expected, the one year averaged Copernicus model plot indicated low power potential, near the Maltese Islands, with lower potential along the East coast when compared to the West, classifying the area as a Class I wave resource (the lowest classification). Along with this, high variability is seen in Maltese waters, with a tendency of higher variability occurring beyond the West coast as compared to the East coast. This is unfavourable since the high and low of the power availability and variability, respectively, occur at opposing sides.

The estimation of power output based on the Copernicus forecast can be said to be reliable when comparing it to the hindcast analysis data on both a short time-scale (1hr) and a longer time-scale (24hr), making it suitable basis for power potential forecast.

On the consideration of WECs, the analyses carried out suggests that the top two suitable technologies are those of the Wave Dragon and Wavestar C6, both having the highest values of power output and capacity factor. Given the Wavestar C6 is a point absorber, hence less directional, it is probably a better choice over the Wave Dragon, despite the latter's higher output power.

6.1 Future work

The analyses carried out in this work depends heavily on the datasets used. It is to be noted that the limited amount of HF radar data hindered the analysis in regards to the data source. Collection of this data in a more complete form over a longer period of time is then required for a more sound analyses to be carried out.

The MCA index calculation was in this work presented for a single point. The calculation of the index over a whole mapped region can be also done, however, this required more time than available in order to run the calculation over for all the points.

The analysis regarding the power output of the WECs, in this case, did not consider explicitly the directionality of the technologies. Investigation of how this parameter affects the power output would yield a better picture of the suitability of the respective WEC.

References

[1] Neill SP, Hashemi MR. Chapter 5 - Wave Energy. In: Neill SP, Hashemi MR, editors. Fundamentals of Ocean Renewable Energy. E-Business Solutions. Academic Press; 2018. p. 107–140.

[2] Holthuijsen LH, Booij N, van Endt M, Cakes S, Soares CG. Assimilation of buoy and satellite data in wave forecasts with integral control variables. Journal of Marine Systems. 1997;13(1):21–31.

[3] Violante-Carvalho N, Ramos AVC. Revisão das Técnicas para a Assimilação do Espectro Direcional Bi-Dimensional em Modelos de Ondas. Revista Ciências Exatas e Naturais. 2006;8(1):9–24.

[4] Drago A, Ciraolo G, Capodici F, Cosoli S, Gacic M, Poulain PM, et al. In: CALYPSO an operational network of HF radars for the Malta-Sicily Channel. Proceedings of the Seventh EuroGOOS International Conference; 2014. p. 167–176.

[5] Pecher A, Kofoed JP. Handbook of Ocean Wave Energy. Ocean Engineering & Oceanography. Springer International Publishing; 2016.

[6] Neill SP, Hashemi MR. Chapter 7 - In Situ and Remote Methods for Resource Characterization. In: Neill SP, Hashemi MR, editors. Fundamentals of Ocean Renewable Energy. E-Business Solutions. Academic Press; 2018. p. 157–191.

[7] Cefas. WaveNet Interactive Map;. Available from: `http://wavenet.cefas.co.uk/Map`.

[8] NOAA. National Data Buoy Center;. Available from: `https://www.ndbc.noaa.gov/`.

[9] Drago A, Azzopardi J, Gauci A, R T, Bruschi A. Assessing the offshore wave energy potential for the Maltese islands. ISE Annual Conference. 2013 03;p. 16–27.

[10] Joodaki G, Nahavandchi H, Cheng K. Ocean Wave Measurement Using GPS Buoys. Journal of Geodetic Science. 2013;3(3):163–172. Available from: https://doi.org/10.2478/jogs-2013-0023.

[11] Carrasco-Álvarez R, Streßer M, Horstmann J. A Simple Method for Retrieving Significant Wave Height from Dopplerized X-Band Radar. Ocean Science Discussions. 2016 05;p. 1–14.

[12] Dankert H, Rosenthal W. Ocean surface determination from X-band radar-image sequences. Journal of Geophysical Research: Oceans. 2004;109(C4). Available from: https://agupubs.onlinelibrary.wiley.com/doi/abs/10.1029/2003JC002130.

[13] Hwang PA, Sletten MA, Toporkov JV. A note on Doppler processing of coherent radar backscatter from the water surface: With application to ocean surface wave measurements. Journal of Geophysical Research: Oceans. 2010;115(C3). Available from: https://agupubs.onlinelibrary.wiley.com/doi/abs/10.1029/2009JC005870.

[14] Carrasco R, Horstmann J, Seemann J. Significant Wave Height Measured by Coherent X-Band Radar. IEEE Transactions on Geoscience and Remote Sensing. 2017;55(9):5355–5365.

[15] Crombie DD. Doppler spectrum of sea echo at 13.56 MC/s. Nature. 1955;175:681–682.

[16] Barrick DE. Remote sensing of sea state by radar. In: Derr VE, editor. Remote Sensing of the Troposphere. Washington, D. C: U.S Government Printing Office; 1972. .

[17] Lipa B. Inversion of second-order radar echoes from the Sea. Journal of Geophysical Research. 1978 01;83:959–962.

[18] Mader J, Rubio A, Asensio J, Novellino A, Alba M, Corgnati L, et al.. The European HF Radar Inventory; 2016.

[19] EuroGOOS. High Frequency Radar;. Available from: http://eurogoos.eu/high-frequency-radar-task-team/.

[20] Neill SP, Hashemi MR. Chapter 8 - Ocean Modelling for Resource Characterization. In: Neill SP, Hashemi MR, editors. Fundamentals of Ocean Renewable Energy. E-Business Solutions. Academic Press; 2018. p. 193–235.

[21] Komen GJ, Cavaleri L, Donelan M, Hasselmann K, Hasselmann S, Janssen PAEM. Dynamics and Modelling of Ocean Waves. Cambridge University Press; 1994.

[22] Booij N, Ris RC, Holthuijsen LH. A third-generation wave model for coastal regions: 1. Model description and validation. Journal of Geophysical Research: Oceans. 1999;104(C4):7649–7666. Available from: `https://agupubs.onlinelibrary.wiley.com/doi/abs/10.1029/98JC02622`.

[23] NOAA. NOAA WAVEWATCH III®;. Available from: `https://polar.ncep.noaa.gov/waves/ensemble/`.

[24] Holthuijsen LH. Waves in Oceanic and Coastal Waters. Cambridge University Press; 2007.

[25] Janssen P. The wave model May 1995. 1995 01;.

[26] Hasselmann K. On the spectral dissipation of ocean waves due to white capping. Boundary-Layer Meteorology. 1974 01;6:107–127.

[27] Ardhuin F, Bertotti L, Bidlot JR, Cavaleri L, Filipetto V, Lefevre JM, et al. Comparison of wind and wave measurements and models in the Western Mediterranean Sea. Ocean Engineering. 2007;34(3):526–541.

[28] Chang WY. A Literature Review of Wind Forecasting Methods. Journal of Power and Energy Engineering. 2014 01;02:161–168.

[29] Wu YK, Hong JS. A literature review of wind forecasting technology in the world. In: 2007 IEEE Lausanne Power Tech; 2007. p. 504–509.

[30] Saulter AN, Bunney C, King RR, Waters J. An Application of NEMOVAR for Regional Wave Model Data Assimilation. Frontiers in Marine Science. 2020;7:897. Available from: `https://www.frontiersin.org/article/10.3389/fmars.2020.579834`.

[31] Li XM, Lehner S, He MX. Ocean wave measurements based on satellite synthetic aperture radar (SAR) and numerical wave model (WAM) data - extreme sea state and cross sea analysis. International Journal of Remote Sensing. 2008;29(21):6403–6416. Available from: `https://doi.org/10.1080/01431160802175546`.

[32] Lionello P, Günther H, Janssen PAEM. Assimilation of altimeter data in a global third-generation wave model. Journal of Geophysical Research: Oceans. 1992;97(C9):14453–14474. Available from: `https://agupubs.onlinelibrary.wiley.com/doi/abs/10.1029/92JC01055`.

[33] Deshmukh AN, Deo MC, Bhaskaran PK, Nair TMB, Sandhya KG. Neural-Network-Based Data Assimilation to Improve Numerical Ocean Wave Forecast. IEEE Journal of Oceanic Engineering. 2016;41(4):944–953.

[34] Greenslade D, Young I. Background errors in a global wave model determined from altimeter data. Journal of Geophysical Research-Oceans. 2004 09;109.

[35] Mastenbroek C, Makin V, Voorrips A, Komen G. Validation of ERS-1 altimeter wave height measurements and assimilation in a North Sea wave model. The Global Atmosphere and Ocean System. 1994;2:143–161.

[36] Breivik LA, Reistad M. Assimilation of ERS-1 Altimeter Wave Heights in an Operational Numerical Wave Model. Weather and Forecasting. 1994;p. 440–451.

[37] Voorrips AC, Makin VK, Hasselmann S. Assimilation of wave spectra from pitch-and-roll buoys in a North Sea wave model. Oceanographic Literature Review. 1997;44(10):1084.

[38] Breivik LA, Reistad M, Schyberg H, Sunde J, Krogstad HE, Johnsen H. Assimilation of ERS SAR wave spectra in an operational wave model. Journal of Geophysical Research: Oceans. 1998 Apr;103(C4):7887–7900.

[39] Talagrand O. Assimilation of Observations, an Introduction (gtSpecial IssueltData Assimilation in Meteology and Oceanography: Theory and Practice). Journal of the Meteorological Society of Japan Ser II. 1997;75(1B):191–209.

[40] Panteleev G, Yaremchuk M, Rogers W. Adjoint-Free Variational Data Assimilation into a Regional Wave Model. Journal of Atmospheric and Oceanic Technology. 2015 02;32:150211132110008.

[41] Kamranzad B, Hadadpour S. A multi-criteria approach for selection of wave energy converter/location. Energy. 2020;204:117924.

[42] OES. Waves. Ocean-energy-systems.org;. Available from: https://www.ocean-energy-systems.org/ocean-energy/what-is-ocean-energy/waves/.

[43] Guillou N, Chapalain G. Annual and seasonal variabilities in the performances of wave energy converters. 2018 10;.

[44] López M, Ramos V, Rosa-Santos P, Taveira-Pinto F. Effects of the PTO inclination on the performance of the CECO wave energy converter. Marine Structures. 2018;61:452–466.

[45] AWS. ARCHIMEDES WAVESWING: SUBMERGED WAVE POWER BUOY. awsocean.com;. Available from: https://www.awsocean.com/archimedes-waveswing/.

[46] Environmental Change Institute. Variability of UK Marine resources; 2005.

[47] Babarit A, Hals J, Muliawan MJ, Kurniawan A, Moan T, Krokstad J. Numerical benchmarking study of a selection of wave energy converters. Renewable Energy. 2012;41:44–63.

[48] Angenita M. WaveBob Company Profile. calameo.com;. Available from: https://en.calameo.com/books/000674314aec3c0329ef5.

[49] Tarrant K, Meskell C. Investigation on parametrically excited motions of point absorbers in regular waves. Ocean Engineering. 2016 01;111:67–81.

[50] Downing L. Wavebob Shuts Down After Failing to Raise Funds, Find Partner; 2013. Available from: https://www.bloomberg.com/news/articles/2013-04-03/wavebob-shuts-down-after-failing-to-raise-funds-find-partner.

[51] Weinstein A, Fredrikson G, Parks MJ, Nielsen K. AquaBuOY - the offshore wave energy converter numerical modeling and optimization. In: Oceans '04 MTS/IEEE Techno-Ocean '04 (IEEE Cat. No.04CH37600). vol. 4; 2004. p. 1854–1859 Vol.4.

[52] NS ENERGY. Hydrokinetic movement. nsenergybusiness.com;. Available from: https://www.nsenergybusiness.com/features/featurehydrokinetic-movement/attachment/aquabuoy_deployed/.

[53] WAVESTAR. How it works. wavestarenergy.com;. Available from: http://wavestarenergy.com/concept.

[54] Marquis L, Kramer M, Kringelum J, Chozas J, Helstrup NE. Introduction Of Wavestar Wave Energy Converters At The Danish Offshore Wind Power Plant Horns Rev 2; 2012. Null ; Conference date: 17-10-2012 Through 19-10-2012.

[55] WAVESTAR. Projects. wavestarenergy.com;. Available from: http://wavestarenergy.com/projects.

[56] Rosa-Santos P, Taveira-Pinto F, Rodríguez CA, Ramos V, López M. The CECO wave energy converter: Recent developments. Renewable Energy. 2019;139:368–384.

[57] Wave Dragon. Principles. wavedragon.net;. Available from: http://www.wavedragon.net/principles/.

[58] Wave Dragon. Specifications. wavedragon.net;. Available from: `http://www.wavedragon.net/specifications/`.

[59] Ghasemi A. Computational Simulation of the Interaction Between Moving Rigid Bodies and Two-Fluid Flows; 2013.

[60] Sea Power Ltd . Technology. seapower.ie;. Available from: `http://www.seapower.ie/our-technology/`.

[61] POWER TECHNOLOGY. Pelamis, World's First Commercial Wave Energy Project, Agucadoura. power-technology.com;. Available from: `https://www.power-technology.com/projects/pelamis/`.

[62] EMEC. PELAMIS WAVE POWER. emec.org.uk;. Available from: `https://www.emec.org.uk/about-us/wave-clients/pelamis-wave-power/`.

[63] OceanEnergy. What is the OE Buoy?. oceanenergy.ie;. Available from: `https://oceanenergy.ie/oe-buoy/`.

[64] Mota P, Pinto JP. Wave energy potential along the western Portuguese coast. Renewable Energy. 2014;71:8–17.

[65] Vicinanza D, Contestabile P, Ferrante V. Wave energy potential in the north-west of Sardinia (Italy). Renewable Energy. 2013;50:506–521.

[66] Iglesias G, López M, Carballo R, Castro A, Fraguela JA, Frigaard P. Wave energy potential in Galicia (NW Spain). Renewable Energy. 2009;34(11):2323–2333.

[67] Iglesias G, Carballo R. Wave energy potential along the Death Coast (Spain). Energy. 2009;34(11):1963–1975.

[68] Sierra JP, Martín C, Mösso C, Mestres M, Jebbad R. Wave energy potential along the Atlantic coast of Morocco. Renewable Energy. 2016;96:20–32.

[69] Lisboa R, Teixeira P, Fortes C. Numerical evaluation of wave energy potential in the south of Brazil. Energy. 2017 01;121:176.

[70] WERMED. Malta page on WERMED;. Available from: `http://www.capemalta.net/maria/pages/about.html`.

[71] BOE. The BLUE OCEAN ENERGY Project;. Available from: `http://oceania.research.um.edu.mt/cms/blueocean/index.php?option=com_content&view=article&id=3&Itemid=103`.

[72] Datawell. Waverider SG - Second generation non-directional wave height measuring buoy;.

[73] Orasi A, Picone M, Drago A, Capodici F, Gauci A, Nardone G, et al. HF radar for wind waves measurements in the Malta-Sicily Channel. Measurement. 2018 06;128.

[74] Picone M, Orasi A, Drago A, Capodici F, Ciraolo G, Nardone G, et al. A Wave Measurements HF Radar Data Set in the Malta-Sicily Channel: Data Quality, Validation and Gap Filling;. .

[75] EUCC-D. HIPOCAS: Hindcast of dynamic processes of the ocean and coastal areas of Europe; n.d. Available from: `http://databases.eucc-d.de/plugins/projectsdb/project.php?show=301`.

[76] HIPOCAS. HIPOCAS; 2002. Available from: `http://www.mar.ist.utl.pt/hipocas/info.asp`.

[77] Veness C. Calculate distance, bearing and more between Latitude/Longitude points; n.d. Available from: `https://www.movable-type.co.uk/scripts/latlong.html`.

[78] BC Campus. The Regression Equation; n.d. Available from: `https://opentextbc.ca/introstatopenstax/chapter/the-regression-equation/`.

[79] Thakur M. Coefficient of Determination Formula; n.d. Available from: `https://www.educba.com/coefficient-of-determination-formula/`.

[80] Fairly Nerdy. What Is R Squared And Negative R Squared;. Available from: `http://www.fairlynerdy.com/what-is-r-squared/`.

[81] MathWorks. corr2; n.d. Available from: `https://www.mathworks.com/help/images/ref/corr2.html`.

[82] Rusu E, Raileanu A. A multi-parameter data-assimilation approach for wave prediction in coastal areas. Journal of Operational Oceanography. 2016;9(1):13–25. Available from: `https://doi.org/10.1080/1755876X.2016.1192013`.

[83] Factor TA. Assessing the Fit of Regression Models;. Available from: `https://www.theanalysisfactor.com/assessing-the-fit-of-regression-models/`.

[84] Pal R. Chapter 4 - Validation methodologies. In: Pal R, editor. Predictive Modeling of Drug Sensitivity. Academic Press; 2017. p. 83–107.

[85] MathWorks. histcounts; n.d. Available from: `https://www.mathworks.com/help/matlab/ref/histcounts.html`.

[86] Cornett A. A Global Wave Energy Resource Assessment. In: Proceedings of the eighteenth international offshore and polar conference. 2008 07;50.

[87] MathWorks. histogram2; n.d. Available from: `https://www.mathworks.com/help/matlab/ref/matlab.graphics.chart.primitive.histogram2.html`.

[88] Bingölbali B, Jafali H, Akpınar A, Bekiroğlu S. Wave energy potential and variability for the south west coasts of the Black Sea: The WEB-based wave energy atlas. Renewable Energy. 2020;154:136–150.

[89] Korres G, Ravdas M, Zacharioudaki A, Denaxa D, Sotiropoulou M. Mediterranean Sea Waves Analysis and Forecast (CMEMS MED-Waves, MedWA3 system) (Version 1). Copernicus Monitoring Environment Marine Service (CMEMS); 2021. Available from: `https://doi.org/10.25423/CMCC/MEDSEA_ANALYSISFORECAST_WAV_006_017_MEDWAM3`.

[90] Korres G, Ravdas M, Zacharioudaki A, Sotiropoulou M, Denaxa D, Lecci R. Product User Manual: For Mediterranean Sea Waves Analysis and Forecasting Product MEDSEA_ANALYSISFORECAST_WAV_006_017. Copernicus Marine Service; 2021.

[91] Galea De Giovanni R. Drago A, editor. CALYPSO South: Technical Report. University of Malta; 2019.

[92] University of Malta. Oceanography Malta Group; n.d. Available from: `https://www.um.edu.mt/r/research/oceanographymalta`.

[93] Lagrangian Drifter Laboratory. LDL Introduces the Directional Wave Spectra Drifter (DWSD)™. Scripps Institution of Oceanography;. Available from: `https://gdp.ucsd.edu/ldl/news-dws-drifter/`.

[94] Lagrangian Drifter Laboratory. DIRECTIONAL WAVE SPECTRA DRIFTER (DWSD)™. Scripps Institution of Oceanography;. Available from: `https://gdp.ucsd.edu/ldl/dwsd/`.

[95] CPO. New type of drifter released: the Directional Wave Spectra Drifter. Climate Program Office;. Available from: `https://cpo.noaa.gov/Serving-Society/NIHHIS/ArtMID/6409/ArticleID/1506/New-type-of-drifter-released-the-Directional-Wave-Spectra-Drifter`.

[96] Centurioni L, Braasch L, Di Lauro E, Contestabile P, De Leo F, Casotti R, et al. A NEW STRATEGIC WAVE MEASUREMENT STATION OFF NAPLES PORT MAIN BREAKWATER; 2017. .

[97] Physical Oceanography Research Group. NEWS Malta GPS Wave Buoy Interface. Interreg Italia-Malta NEWS;. Available from: `http://ioi.research.um.edu.mt/news-waves/index.php/welcome/open_map/`.

[98] CODAR Ocean Sensors. SeaSonde Wave WVLM File Format. CODAR Ocean Sensors Ltd; 2016.

[99] E U Copernicus Marine Service Information. GLOBAL OCEAN L3 SIGNIFICANT WAVE HEIGHT FROM NRT SATELLITE MEASUREMENTS. Copernicus Monitoring Environment Marine Service (CMEMS); n.d. Available from: `https://resources.marine.copernicus.eu/product-detail/WAVE_GLO_WAV_L3_SWH_NRT_OBSERVATIONS_014_001/INFORMATION`.

[100] Mertz F, Husson R, Taburet N, Charles E. Product User Manual: For WAVE Products WAVE_GLO_WAV_L3_SWH_NRT_OBSER-VATIONS_014_001, WAVE_GLO_WAV_L3_SPC_NRT_OBSERVA-TIONS_014_002, WAVE_GLO_WAV_L4_SWH_NRT_OBSERVA-TIONS_014_003. Copernicus Marine Service; 2020.

[101] EMODnet Bathymetry. Bathymetry Viewing and Download Service;. Available from: `https://www.emodnet-bathymetry.eu/data-products`.

[102] Charles G. The climate of the Maltese Islands. Institute for Sustainable Energy, University of Malta; 2012. p. 65–69.

[103] Martinez A, Iglesias G. Wave exploitability index and wave resource classification. Renewable and Sustainable Energy Reviews. 2020;134:110393.